Photochemical and Electrochemical Generation of Hydrogen Based on MoS_2 and $MoSe_2$, and their Adducts with Other Low Dimensional Materials

A Thesis Submitted for the Degree of

M. S. (Engg.)

By

Devesh Chandra Binwal

New Chemistry Unit

Jawaharlal Nehru Centre for Advanced Scientific Research

(A Deemed University)

Bangalore-560064 (India)

September 2021

Dedicated to my parents and teachers

DECLARATION

I hereby declare that the matter embodied in this M.S. (Engg.) thesis entitled **"Photochemical and Electrochemical Generation of Hydrogen Based on MoS_2 and $MoSe_2$, and their Adducts with Other Low Dimensional Materials"** is the result of investigations carried out by me at the New Chemistry Unit, and the International Centre for Materials Science, Jawaharlal Nehru Centre for Advanced Scientific Research, Bengaluru, India under the supervision of **Prof. C. N. R. Rao, FRS** and that it has not been submitted elsewhere for the award of any degree or diploma.

In keeping with the general practice in reporting scientific investigations, due acknowledgement has been made wherever the work described is based on findings of other investigators. Any omission that might have occurred by oversight or error of judgement is regretted.

(Devesh Chandra Binwal)

CERTIFICATE

I hereby declare that the matter embodied in the thesis entitled **"Photochemical and Electrochemical Generation of Hydrogen Based on MoS_2 and $MoSe_2$, and their Adducts with Other Low Dimensional Materials"** has been carried out by Mr. Devesh Chandra Binwal at the New Chemistry Unit, and the International Centre for Materials Science, Jawaharlal Nehru Centre for Advanced Scientific Research, Bengaluru, India under my guidance and that it has not been submitted elsewhere for the award of any degree or diploma.

Prof. C. N. R. Rao

(Research Supervisor)

ACKNOWLEDGEMENTS

I am extremely thankful to **Prof. C.N.R. Rao**, **FRS,** my research supervisor and take this opportunity to express my immense gratitude to him.

He not only introduced me to the field of Material Science but also has helped me with his invaluable guidance and fascinating constant encouragement. He is a person of immense enthusiasm and wisdom. It was his enthusiasm and dedication that instigated in me the desire to pursue science and has continued to inspire me ever since. His innovative ideas and ability to handle any problem in the simplest of the ways has been the strength behind the completion of this work. He has not only been instrumental in shaping up my research, and my career but my entire personality, and my outlook towards life as a whole. With his fathomless patience, unfailing support, critical suggestions, and iron will, nothing has ever been a hurdle in this journey. I cannot express words for the respect and care that I have for him.

Special thanks to all my ***scientific collaborators*** because without their help, my work would have been incomplete: Dr. K. Pramoda, Dr. Manjodh Kaur, Prof. Alla Zak, Dr. P. Chithaiah.

I thank my ***course work instructors***: Prof. A. Sundaresan, Prof. Sebastian Peter, Prof. Ranjani Viswanatha, Prof. Bivas Saha, for the illuminating courses and discussions.

My sincere thanks to Prof. Subi J. George for his constant support and help in various aspects.

I would like to thank Dr. Pratap Vishnoi for his help and constant support.

I would like to thank Dr. K. Pramoda for his support and help throughout this journey.

I would like to thank Mr. Abhishek for helping me in zeta potential studies.

Let me take this opportunity to thank my ***beloved labmates***: Dr. K. Pramoda, Dr. Manjeet Chhetri, Dr. Anand Roy, Dr. K. Manjunath, Dr. Manjodh Kaur, Mr. Monis Ayyub, Ms. Manaswee Barua, Mr. Rohit Attri, Mr. Reetendra, Mr. Swaraj, Ms. Aditi Saraswat. A special thanks and it has been an enjoyable experience working with all of them.

I thank the timely help of the ***technical staff*** members: Mr. Vasu, Mr. Anil, Mr. Mahesh, Mr. Kannan, Ms. Meenakshi, Mr. Shivakumar, Mr. Mune Gowda and Mr. Dileep. I specially thank Mrs. Sudha, Mr. Gowda, Mr. Victor, Mrs. Ramya, and Mrs. Melissa for their help in various

aspects.

I extend my sincere thanks to all the staff members associated with ***Administration, Hostel, Academic, Library, Dining hall, Dhanvantari, CPMU***, ***NCU, Security*** and other departments for all their help.

I thank ***JNCASR*** and ***ICMS*** for research fellowship.

I take this opportunity to thank ***Mrs. Indumati Rao and Mr. Sanjay Rao*** for all the affection and love I have received from them. Her notwithstanding age and enthusiasm has been the source of inspiration for me.

I thank all my ***batch mates and friends*** (particularly Swarnima, Manju, Prerana, Aneesh, Bharat, Amit, Rahul, Alice, Hari, Deeksha, Nazia, Yashwini, Prudhvi, Sowmeya, Suryadev, Suhas, Aarif, Anita, Surbhi, Aishwarya) with whom I started my life at JNCASR, and whose cheerful company made these two years of life so cherishable.

Finally, I thank my ***parents***, my ***brothers Hemant Kumar Binwal and Dheerendra Kumar Binwal***, my sister ***Meenakshi Binwal***, ***family members*** and the ***Almighty God*** for everything I have.

PREFACE

The thesis consists of four parts, of which the **first Part** gives a brief overview of photocatalytic and electrocatalytic hydrogen evolution reaction (HER).

Part 2 deals with the studies on HER activity of 2D $MoS_xSe_{(2-x)}$ and $MoSe_xTe_{(2-x)}$ nanosheet solid solutions. In this part, $MoS_xSe_{(2-x)}$ and $MoSe_xTe_{(2-x)}$ solid solutions with various S:Se and Se:Te ratios have been prepared by high-temperature solid-state reactions and thinned down to few-layers by Li-intercalation followed by exfoliation. The exfoliated $MoS_xSe_{(2-x)}$ and $MoSe_xTe_{(2-x)}$ nanosheets catalyze the photocatalytic and electrocatalytic hydrogen evolution from splitting water. The photocatalytic HER activity increases with the selenium contents - Se-rich $MoS_{0.5}Se_{1.5}$ exhibits the highest photocatalytic HER activity among the $MoS_xSe_{(2-x)}$ solid solutions. These solid solutions also exhibit satisfactory electrocatalytic HER activity with low onset potentials in the range of -0.340 to -0.190 mV.

Part 3 presents nanocomposites of MoS_2 nanotubes with polymer-functionalized nanotubes of carbon (SWCNT) and borocarbonitride (BCNNT) and their HER activity. We prepared nanocomposites of MoS_2 nanotube with polymer-functionalized SWCNT and BCNNT by electrostatic restacking. The maximum HER activity of 7475 μmol g^{-1} h^{-1} is achieved in the case of MoS_2−P.SWCNT nanocomposite (3:1), while the physical mixture MoS_2 and SWCNT exhibits only 3112 μmol g^{-1} h^{-1}. The MoS_2−P.SWCNT (3:1) nanocomposite not only shows superior photocatalytic HER activity but also high electrocatalytic H_2 evolution with an onset potential of 80 mV (vs RHE).

In **Part 4**, we show the composites of MoS_2 nanoparticles with carboxyl-functionalized single-walled carbon nanotubes (SWCNT) and MoS_2 nanoparticles with borocarbonitride (BC_6N) nanosheets, and their electrocatalytic HER activity. We report a facile protocol to prepare MoS_2/SWCNT and MoS_2/BC_6N composites in different stoichiometries by mixing MoS_2

nanoparticles with SWCNT or BCN in water. The electrocatalytic HER studies show that MoS_2/SWCNT (3:1) catalyst exhibits a superior electrocatalytic activity with the onset potential of -113 mV (vs RHE) and a small Tafel slope of 59 mV dec^{-1}, which is comparable to some of the highest reported MoS_2-CNT and MoS_2-graphene composites.

TABLE OF CONTENTS

Part-III. Nanocomposites of 1D MoS_2 with Polymer-Functionalized Nanotubes of Carbon and Borocarbonitride, and Their HER Activity

Part-IV. Nanocomposites of MoS_2 Nanoparticles with Carboxyl-Functionalized Carbon Nanotubes and Borocarbonitrides Nanosheets, and Their Electrocatalytic HER Activity

Part I

Introduction to Photochemical and Electrochemical generation of Hydrogen

Introduction

Worldwide energy consumption was 17 TW in 2013, and due to continued increase in the world population and standard of life, energy consumption is predicted to be more than double by 2050.[1,2] The limitation of carboneous fuel, as well as the environmental risks associated with it, highlight the necessity for a clean and renewable energy source. Since it is well known that hydrogen is the most environment-friendly, clean energy that produces no hazardous by-products and has a high energy density of 142 MJ/kg, it encourages researchers to find cost-effective ways to manufacture hydrogen on a large scale. Natural gas reforming requires high temperatures and pressure and produces the hazardous by-products CO and CO_2, currently produces nearly 85-90 percent of hydrogen. Current energy sources such as coal, hydrocarbons, and petroleum are non-renewable and will be unable to meet rising energy demands.[3] A H_2 production strategy is required to obtain renewable energy. The optimal and inexpensive energy resource for this process is water, which is abundant (75 percent of the earth). Hence splitting water to generate hydrogen is an ideal approach because it involves an easy and clean reaction that converts solar energy into H_2. Water splitting can be done in several ways (e.g. Electrolysis, thermochemical, biomass, thermal and, photochemical reactions).

Several semiconductor photocatalysts, such as TiO_2, $NaTiO_3$, Ga_2O_3, $La_2Ti_2O_7$, and others have been reported for splitting water into hydrogen and oxygen under UV light over the previous few decades. Photocatalyst which can make use of visible light would be more efficient because solar light contains 47% of visible light, 5-7% of UV light and the rest of the energy falls near infrared (IR) region,[4] it is necessary to develop stable and efficient visible-light harvesting semiconductor photocatalyst to convert a large proportion of solar energy into chemical energy (H_2).

Transition Metal Dichalcogenides

It is a layered materials class with the general formula MX_2, where M signifies the transition metal atom (Mo, W, etc.) and X signifies the chalcogen atom (S, Se, and Te). In 1923 MoS_2 was first reported by Linus Pauling,[5] after that there has been a wide research on it to discover the applications. Transition Metal Dichalcogenides (TMDs) are found in various polymorphic forms and with different stacking polytypes such as 1T, 2H, and 3R, where numeral denotes the number of units of X–M–X in the unit cell and the letters T, H, and R represent trigonal, hexagonal, rhombohedral, respectively. In monolayer form TMDs exhibit two phases, namely octahedral 1T and trigonal prismatic 2H. MoX_2 (X=S, Se) are semiconductors with an indirect band gap in their 2H phase, this phase is thermodynamically stable. In monolayer MoX_2, the indirect band gap transforms to the direct band gap due to the quantum confinement effect which changes the hybridization between p_z orbitals (S, Se) and d orbitals (Mo). It was shown

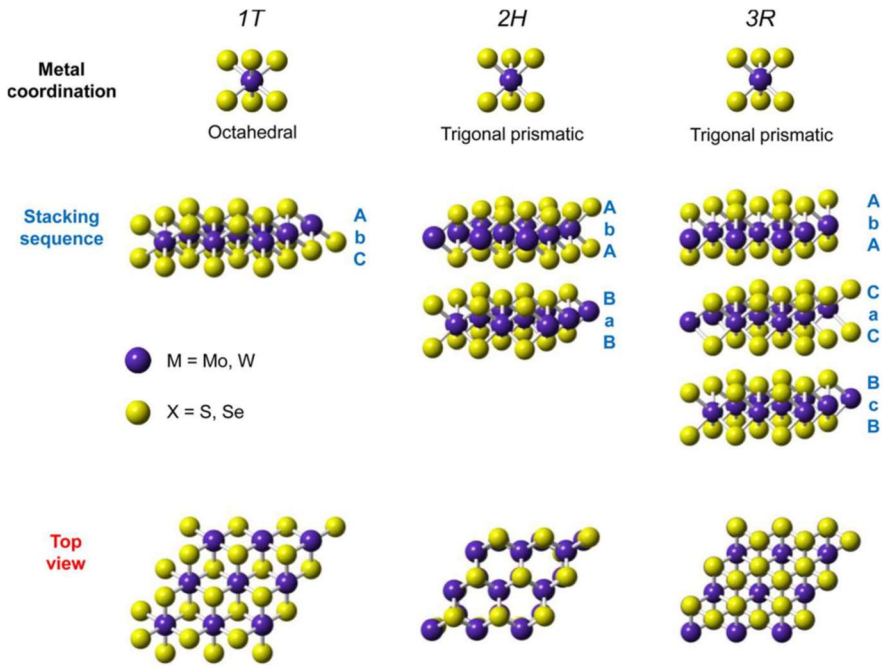

Figure 1. The Structural polytypes of TMDs: 2H, 3R, and 1T. Reproduced with permission.[6] Copyright 2010 American Chemical Society.

by the theoretical calculations that bulk TMDs band edge positions are not appropriate for the water splitting reaction. By reducing the number of layers of TMDs changes the indirect bandgap to a direct bandgap and increases the band gap also. Due to the increase of the bandgap in monolayer TMDs, it provides the appropriate band edge position for water splitting.[7]

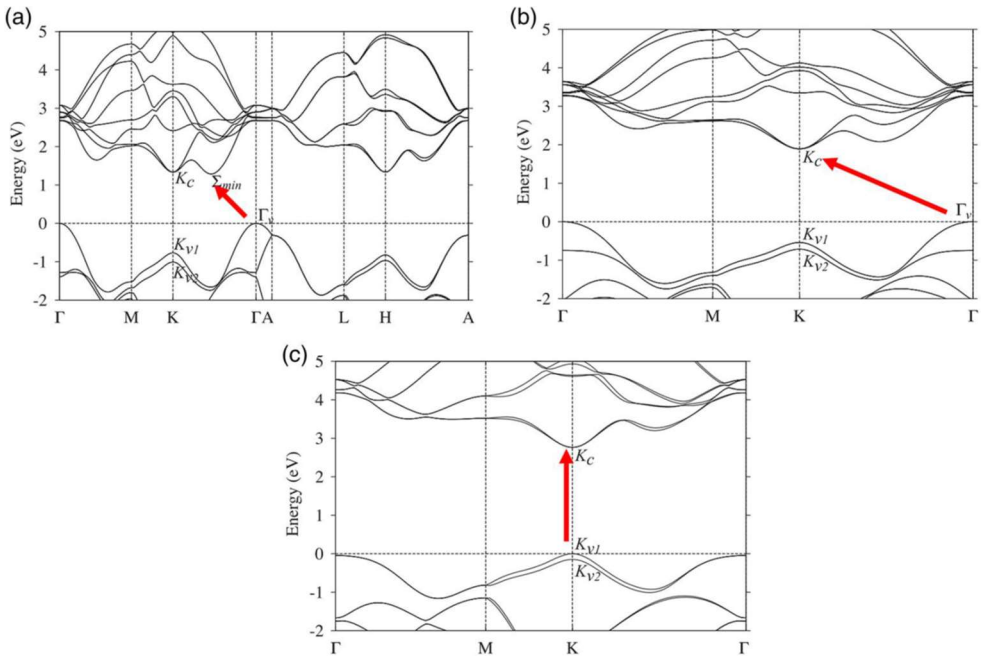

Figure 2. The Band structure of MoS_2 in a) bulk, b) bilayer, and c) monolayer. The arrow indicates the bandgap. Reproduced with permission.[7] Copyright 2012, American Physical Society.

Photocatalytic water splitting

Photocatalytic water splitting is a technique that uses photocatalyst material to split H_2O into H_2 and O_2 in the presence of artificial or natural light (sunlight).[8] Photocatalysts are semiconductor materials having a finite band gap that absorb solar radiation with an energy level that is equal to or greater than the band gap. Semiconductors possess non-overlapping valence and conduction band. Electrons are generated in the conduction band and holes are generated in the valence band when incident light exceeds the band gap. These electrons and holes are called photogenerated charge carriers and they participate in the reduction and

oxidation of H_2O to produce H_2 and O_2, respectively.[9] Reduction of water to H_2 is a two-electron process, whereas oxidation of water to O_2 is a four-electron process. Water oxidation is a rate-limiting step in water splitting because it requires four electrons, which makes it kinetically more challenging than water reduction. It should be noted that splitting of water into H_2 and O_2 can only be facilitated by photogenerated excitons with required thermodynamic potential wherein valence band maxima (VBM) and conduction band minimum (CBM) of semiconductor material employed for water splitting should be more positive and more negative than the water redox potential, respectively, at a given pH (Figure X).[10][11] At pH 0, H^+/H_2 and O_2/H_2O redox potential values are 0 and 1.23 V, respectively hence theoretical minimum band gap of semiconductor catalyst to perform water splitting should be 1.23 eV corresponding to the solar spectrum of wavelength till 1100 nm.[9] Following reactions are involved in water splitting:

$$4H^+ + 4e^- \longrightarrow 2H_2$$

$$2H_2O \longrightarrow O_2 + 4H^+ + 4e^-$$

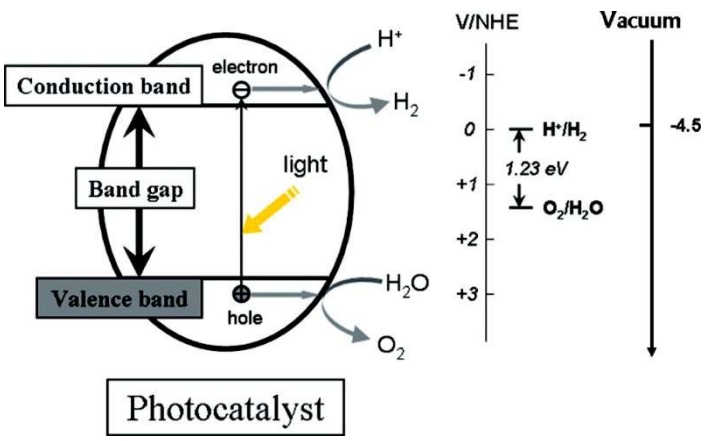

Figure 3. The fundamental principle involved in the semiconductor based water splitting. Reproduced with permission.[8] Copyright 2010 American Chemical Society.

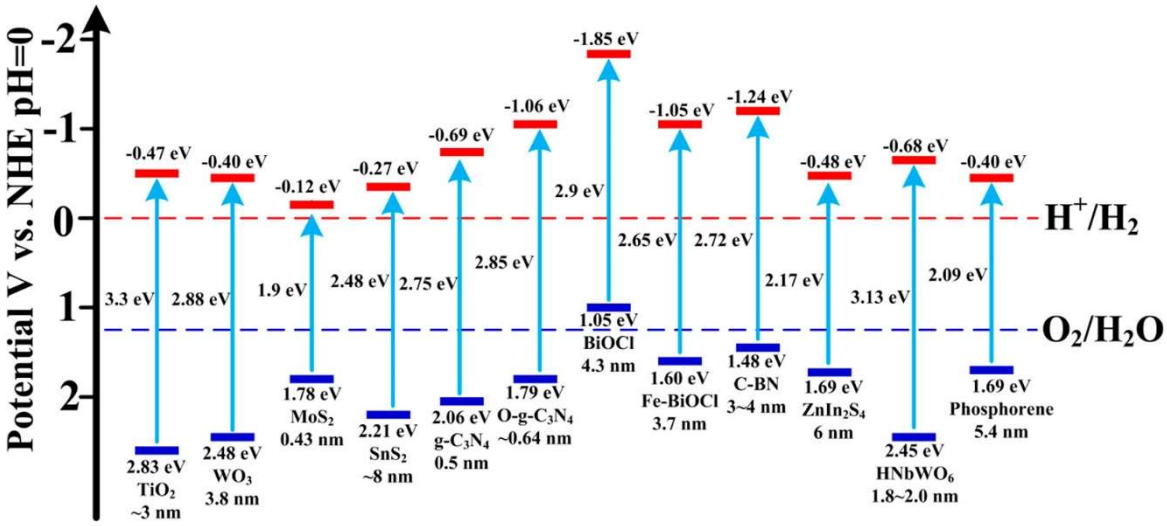

Figure 4. Band positions and band gaps of semiconductors with respect to H_2O redox potential at pH=0. Reproduced with permission.[12] Copyright 2018 American Chemical Society.

The band gaps and band edge positions of semiconductor materials with respect to the water redox potential are illustrated, demonstrating their thermodynamic suitability for photooxidation, photoreduction, and water splitting (Figure 4).[12] Semiconductors with suitable CBM and VBM positions ideally can be used for water splitting. In contrast, semiconductors with only suitable CBM or VBM positions can be used for photoreduction or photooxidation of water, respectively.

Figure 5 depicts the steps involved in photocatalytic water splitting[9,10,13] When light is absorbed by a suitable semiconductor, the valence band (HOMO) electrons are excited to the conduction band (LUMO), leaving holes in the valence band. Photogenerated electrons and holes can take the following paths: a) bulk recombination due to columbic attraction, b) separation and migration towards the surface, and c) recombination at the surface. Recombination of the charge carriers is a very simple process that results in the loss of charge

carriers in the form of heat or radiation, however charge separation require external field. As a result, charge carriers separation/recombination rate is an important factor in determining catalytic activity. Surface available charge carriers involved in the redox reaction result in the formation of H_2 and O_2. The yield of hydrogen production is dependent on all the involved steps. The number of photoexcited electrons and holes available at the photocatalyst and water interface determines the rate of HER and OER. In photocatalysis, crystallinity, particle size, and crystal structure of the material all play a role in charge separation and migration of photogenerated electrons and holes, greater the crystalline quality is, the lesser the extent of defects is. Defects operate as trapping and recombination centres among photogenerated electrons and holes, causing a decline in photocatalytic activity. The distance that electrons and holes must travel to the surface is reduced when the catalyst particle size is smaller, reducing the chance of recombination. Any process which reduces the number of photogenerated charge carriers should be avoided to obtain higher H_2 and O_2 yield. Since surface back reaction wherein produced H_2 and O_2 forms H_2O is a thermodynamically downhill reaction, it should be avoided to obtain a higher yield of H_2 and O_2.

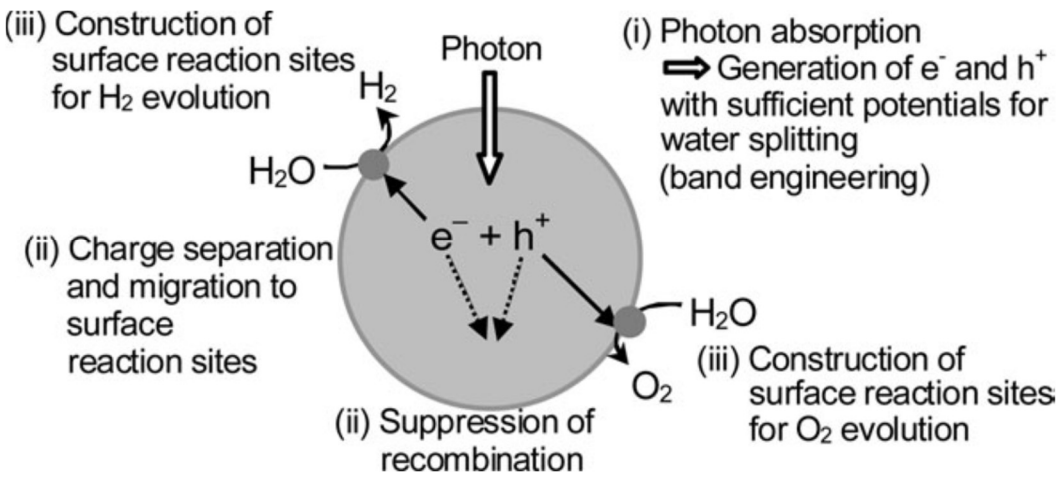

Figure 5. The process involved in photocatalytic water splitting. Reproduced with permission.[9] Copyright 2009 The Royal Society Of Chemistry.

Visible-Light Induced H_2 Generation using Dye as a Photosensitizer

In our next chapters we have used dye for photocatalysis, in this approach dye is used as a photosensitizer in the presence of catalysts such as MoS_2, $MoSe_2$, and graphene. When we irradiate light in the vessel, singlet excited state ($EY^{1}*$) generates due to the excitation of Eosin Y which converts into triplet state ($EY^{3}*$) followed by the formation of EY^{-} after accepting electrons from sacrificial electron donors (Triethanolamine).[14] This electron migrates to the surface of the catalytic material wherein it reduces the adsorbed H^{+} into H_2 (Figure).[14] N doped graphene (n-type) composite with MoS_2: (p-type) substantially improves HER because of effective charge separation. It is proven that 1T-MoS_2 is catalytically superior than the 2H form of MoS_2. In some of the recent articles 1T, and 2H form of $MoSe_2$ is used with photosensitizer Eosin-Y and it is important to point out that 1T-$MoSe_2$ revealed higher activity in comparison to MoS_2 and 2H $MoSe_2$.[15]

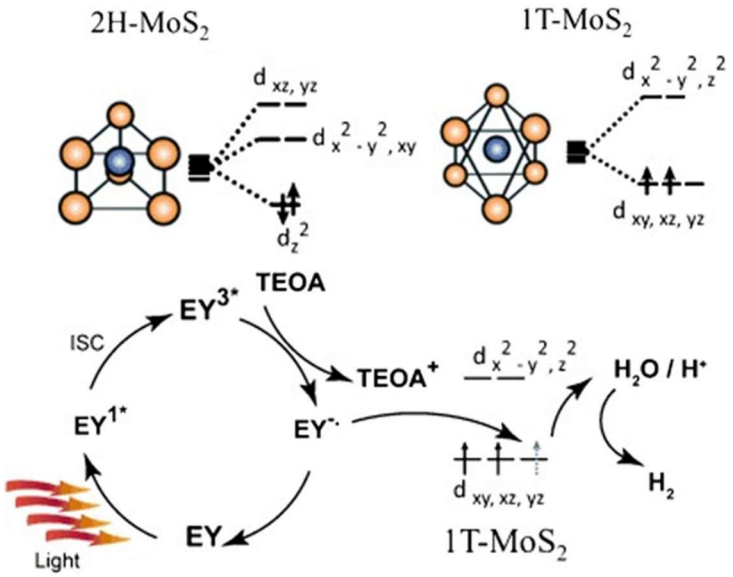

Figure 6. Proposed mechanism for catalytic activity of 1T-MoS_2 involved in photocatalytic water splitting. Reproduced with permission.[14] Copyright 2013 Wiley-VCH Verlag GmbH & Co. kGaA, Weinheim.

Role of Sacrificial Electron Donors and Acceptors

Sacrificial agents are used to either consume the photogenerated electrons (in case of OER reaction) or photogenerated holes (in the case of HER reaction). Since HER involve reduction of H^+ into H_2 by photogenerated electrons, hence, getting rid of holes by sacrificial electron donors reduces electron-hole recombination resulting in a significant enhancement in the HER activity in the case of OER reaction wherein photogenerated holes oxidizes H_2O into O_2, sacrificial electron acceptors consumes the generated electrons. Hole scavenging sacrificial reagents can be classified into inorganic and organic electron donors. Organic compounds such as methanol, ethanol, isopropanol, lactic acid, triethanolamine (TEOA) are generally used as sacrificial agents. In our upcoming chapters we have used TEOA as a sacrificaial agent for the photocatalysis.

Experimental setup

The experimental setup is shown in Figure 7. Xenon lamp (Xe-lamp) was used to simulate solar light inside the laboratory. The photocatalyst is irradiated with Visible light using a filter of 395 nm. We have used a photocatalytic reaction cell where after each hour we have taken the evolved hydrogen gas and calculated the amount of gas with the help of Gas Chromatograph.

Figure 7. Experimental setup for photocatalytic HER.

Electrochemical water splitting

Electrolysis can be used to split water by electrochemical reduction of hydronium and hydroxide ions in water.[16–20] The source of hydrogen for H_2 evolution depends on the acidic or alkaline medium used.

$$2H^+ + 2e^- \longrightarrow H_2\,(gas)\ (acidic)$$

$$2H_2O + 2e^- \longrightarrow 2OH^- + H_2\,(gas)\ (alkaline)$$

Electrochemical water splitting requires the use of input energy in the form of electricity (applied voltage or current). Water splitting reaction is conceptually simple yet obtaining its constituents, oxygen, and hydrogen is a difficult task in practice. The Gibbs free energy

associated with water splitting is $\Delta G^o = +237$ kJ/mol. This corresponds to $\Delta E^o = 1.23$ V [$\Delta G^o = -nF\Delta E^o$] redox potential. The half reactions at cathode and anode can be represented as,

In acidic medium,

$$2H^+ + 2e^- \longrightarrow H_2 \qquad E^0 = 0\ V \qquad vs\ NHE$$

$$O_2 + 4H^+ + 4e^- \longrightarrow 2H_2O \qquad E^0 = 1.229\ V \qquad vs\ NHE$$

A 2-electron transfer reaction produces hydrogen in the cathodic half-reaction, while a 4-electron transfer reaction produces oxygen in the anodic half-reaction. The complete water splitting reaction is as follows:

$$2H_2O + 4e^- \longrightarrow 2H_2 + O_2 \qquad \Delta G^0 = 237\ kJmol^{-1}$$

When electrodes are dipped in conductive water (aqueous electrolyte), H_2 and O_2 are generated at the respective electrodes when appropriate voltage is applied (equal to or greater than 1.23 V versus RHE). Theoretically, a voltage difference of 1.23 V between the anode and the cathode is required to split water, but in practise, we discover that a higher voltage is required due to the internal resistances of the cell as well as the necessity to overcome kinetic barriers at each electrode. This difference in the desired voltage more than the thermodynamically determined voltage is called the overpotential (η). Many characteristics, like as catalysts and cell architecture, can be optimised to minimise the additional voltage. Lower the overpotential better it is, the main goal is to bring the overpotential as close to zero as possible.

$$\eta_{required} = 1.23 + \eta_{cathode} + \eta_{anode} + iR_{internal\ resistance}$$

Where $\eta_{cathode}$ and η_{anode} are the kinetic activation barriers imposed at the electrode surface to the electron transfer reactions at the cathode and anode, respectively.

The pH of the electrolyte does matter when we study the activity of one of the two half cell electrodes with a potentiostat. So the required potential for that particular half cell reaction is

applied depending on the pH by the Nernst equation. In which case, the observed potential is reported with respect to reversible hydrogen electrode (RHE) allowing us to directly compare the positions of redox event with respect to standard reduction potential of hydrogen (0 V vs RHE) regardless of pH.

$$E_{RHE} = E_{NHE} + 0.059 \times pH$$

Electrode-Electrolyte Interface

The electrode and electrolyte's interface induces rearrangement of the solvent dipoles and charged species where electrode can be thought to be a giant central ion. At this interface electroneutrality is broken and electrode electrolyte surface becomes electrified interface. Charges are separated at this interface and potential difference develops which is called electrical double layer. Potential developed across this interface is not large because of the extremely small dimensions of the double layer interface region the potential gradient is as high as 10^7 V/cm. Due to this field gradient, the electrode-electrolyte interface is essence of any electrochemical reactions. Electric field in this region can either accelerate or decelerate an ionic species involved in a half cell reaction.

Double layer is formed due to the unequal distributions of ionic species at the interface as compared to the bulk. If the number of positive ions is more than negative ions at the lamina of the interface, evidently there is accumulation of positive ions at the interfacial boundary relative to bulk of an electrolyte. This would mean that the electrode surface is capable of preferentially collecting/accumulating positive ions (this is termed as an active site in following chapters). This is adsorption phenomenon and it is very important parameter in electrocatalytic reactions like water splitting.

In all the chapters, few essential concepts and a number of parameters and terms are used to access and infer the activity of the catalyst. Hence, in the following pages these terms are explained along with their significance within the context of water splitting.

Linear Sweep Voltammetry (LSV)

In the study of current vs voltage relationship, if potential is linearly swept at a constant rate from voltage V_1 to V_2, it is called linear sweep voltammetry (LSV). In the case of a water splitting reaction, this technique is used to study the efficiency and activity of a catalyst. LSV is used to determine the onset potential, overpotential and Tafel slopes. These terms are discussed below.

Overpotential and Onset potential

To compare the electrocatalysts, terms onset potential and overpotential are used. Onset potential is used to describe the potential at which redox reaction of study starts. The potential required to achieve a current density of 10 $mAcm^{-2}$ for the reaction of study is called overpotential. The onset potential term is not clear, some researchers assume the potential at $1mA/cm^2$ as the onset potential and some researchers consider the onset potential by drawing the tangent to the cathodic/anodic curve and the initial non faradic curve, the point of intersection of these two is the onset potential.[18,19,21–24]

Tafel Analysis

Butler–Volmer equation is the foundation for the study of electrochemical kinetics describing the relation between current as a function of overpotential. The most simplified expression of Butler-Volmer equation is given below,

$$I = I_0 \left[e^{\frac{(1-\alpha)ne\eta}{k_B T}} - e^{-\frac{\alpha n}{k_B T}} \right]$$

Where $I_0 = neA(k_c C_O)^{1-\alpha} (k\alpha C_R)^{\alpha}$ is the exchange current density. 'O' and 'R' stands for oxidation and reduction whereas 'a' and 'c' stands for anode and cathode, C is the concentration and η is overpotential, 'α' is the electron transfer coefficient, 'k' is the rate of reaction, 'k_B' and T are the Boltzmann constant and temperature, respectively. Butler-Volmer equation predicts an asymptotic linear dependence for large overpotentials, where the slope is related to the transfer coefficient and the y-intercept gives the exchange current. So, equation can be represented as Tafel equation given below,

$$\eta = a + b \log(j)$$

where a and b are constants. If the current density provided by electrocatalyst is plotted as logarithm of the current density vs the overpotential at various potentials, we should get a linear graph. Empirically, the smaller the Tafel slope the better the catalyst, because it means that smaller increments of overpotential are required to get higher current densities. It should be noted that Tafel analysis is not a complete analysis because of the lack of complete theories available for such systems.

References

[1] S. J. A. Moniz, S. A. Shevlin, D. J. Martin, Z. X. Guo, J. Tang, *Energy Environ. Sci.* **2015**, *8*, 731.

[2] T. Jafari, E. Moharreri, A. S. Amin, R. Miao, W. Song, S. L. Suib, *Molecules* **2016**, *21*, 900.

[3] K. Y. Kumar, H. Saini, D. Pandiarajan, M. K. Prashanth, L. Parashuram, M. S. Raghu, *Catal. Today* **2020**, *340*, 170.

[4] M. Watanabe, *Sci. Technol. Adv. Mater.* **2017**, *18*, 705.

[5] R. G. Dickinson, L. Pauling, *J. Am. Chem. Soc.* **2002**, *45*, 1466.

[6] X. Chia, A. Yong, S. Eng, A. Ambrosi, S. M. Tan, M. Pumera, *Chem. Rev.* **2015**, *115,* 11941.

[7] T. Cheiwchanchamnangij, W. R. L. Lambrecht, *Phys. Rev. B - Condens. Matter Mater. Phys.* **2012**, *85*, 1.

[8] X. Chen, S. Shen, L. Guo, S. S. Mao, *Chem. Rev.* **2010**, *110*, 6503.

[9] A. Kudo, Y. Miseki, *Chem. Soc. Rev.* **2009**, *38*, 253.

[10] X. Chen, S. Shen, L. Guo, S. S. Mao, *Chem. Rev.* **2010**, *110,* 6503.

[11] Y. Wang, H. Suzuki, J. Xie, O. Tomita, D. J. Martin, M. Higashi, D. Kong, R. Abe, J. Tang, *Chem. Rev.* **2018**, *118*, 5201.

[12] T. Su, Q. Shao, Z. Qin, Z. Guo, Z. Wu, *ACS Catal.* **2018**, *8*, 2253.

[13] A. L. Linsebigler, G. Lu, J. T. Yates, *Chem. Rev.* **1995**, *95*, 735.

[14] U. Maitra, U. Gupta, M. De, R. Datta, A. Govindaraj, C. N. R. Rao, *Angew. Chemie - Int. Ed.* **2013**, *52*, 13057.

[15] U. Gupta, B. S. Naidu, U. Maitra, A. Singh, S. N. Shirodkar, U. V. Waghmare, C. N. R. Rao, *APL Mater.* **2014**, *2*, 092802.

[16] R. Subbaraman, D. Tripkovic, D. Strmcnik, K. C. Chang, M. Uchimura, a P. Paulikas, V. Stamenkovic, N. M. Markovic, *Science* **2011**, *334*, 1256.

[17] E. J. Popczun, J. R. McKone, C. G. Read, A. J. Biacchi, A. M. Wiltrout, N. S. Lewis, R. E. Schaak, *J. Am. Chem. Soc.* **2013**, *135*, 9267.

[18] Y. Zheng, Y. Jiao, Y. Zhu, L. H. Li, Y. Han, Y. Chen, A. Du, M. Jaroniec, S. Z. Qiao, *Nat. Commun.* **2014**, *5*, 2.

[19] E. J. Popczun, C. G. Read, C. W. Roske, N. S. Lewis, R. E. Schaak, *Angew. Chemie -*

Int. Ed. **2014**, *53*, 5427.

[20] R. Subbaraman, D. Tripkovic, K. C. Chang, D. Strmcnik, A. P. Paulikas, P. Hirunsit, M. Chan, J. Greeley, V. Stamenkovic, N. M. Markovic, *Nat. Mater.* **2012**, *11*, 550.

[21] R. D. L. Smith, *Science* **2013**, *340*, 60.

[22] R. Guidelli, R. G. Compton, J. M. Feliu, E. Gileadi, J. Lipkowski, W. Schmickler, S. Trasatti, *Pure Appl. Chem.* **2014**, *86*, 245.

[23] J. T. S. Irvine, D. C. Sinclair, A. R. West, *Adv. Mater.* **1990**, *2*, 132.

[24] K. Gelderman, L. Lee, S. W. Donne, *J. Chem. Educ.* **2007**, *84*, 685.

Part II

HER activity of nanosheets of 2D solid solutions of $MoSe_2$ with MoS_2 and $MoTe_2$

Chapter II

HER activity of nanosheets of 2D solid solutions of $MoSe_2$ with MoS_2 and $MoTe_2$

Summary*

$MoS_xSe_{(2-x)}$ and $MoSe_xTe_{(2-x)}$ solid solutions with various S:Se and Se:Te ratios have been prepared by high temperature solid-state reactions and thinned down to few-layers by Li-intercalation followed by exfoliation. Photocatalytic as well as electrocatalytic hydrogen evolution reaction (HER) activity of exfoliated $MoS_xSe_{(2-x)}$ /$MoSe_xTe_{(2-x)}$ 2D nanosheets have been studied. It is found that Se-rich compositions exhibit good HER activity. The $MoS_{0.5}Se_{1.5}$ nanosheets show high photocatalytic HER activity yielding 29.6 mmol h^{-1} g^{-1} of H_2, while $MoS_{1.0}Se_{1.0}$ displays good electrocatalytic activity with an onset potential of -0.220 V. Amongst $MoSe_xTe_{(2-x)}$ solid solutions, $MoSe_{1.8}Te_{0.2}$ shows relatively high photocatalytic HER activity (5.0 mmol h^{-1} g^{-1}), while $MoSe_{1.0}Te_{1.0}$ exhibits a low onset potential (-0.190 V vs. RHE).

*A paper based on this work has been published as D.C. Binwal *et al. Bull. Mater. Sci.*, 2020, 43, 313.

1. Introduction

Since the discovery of graphene, there have been extensive investigations of the various 2D inorganic analogues.[1–3] Some of them are elemental two-dimensional (2D) materials such as phosphorene[4,5] and arsenene.[6] Others are binary compounds of which the most interesting one is MoS_2. Of the various inorganic 2D materials, MoS_2 possesses desirable structural features as well as electronic, optical, and other properties.[7–9] While MoS_2 exists as a semiconductor in the stable 2H-form, it is metallic in the 1T-form generated by Li-intercalation and exfoliation. 2H-polytype of MoS_2 is a direct band gap semiconductor which transforms to the metallic 1T-phase on Li intercalation and exfoliation.[10–12] 1T-MoS_2 shows superior HER activity compared to the 2H-phase. Similar properties are exhibited by $MoSe_2$ as well.[13,14] Nanostructures of MoS_2 and $MoSe_2$ in the 1T-forms are probably the best materials for generating hydrogen from water splitting.[15] $MoSe_2$ also forms the 1T phase on Li-intercalation and exfoliation of 2H-$MoSe_2$.[16–18] The 1T-phases are not stable and transform to the 2H-phase on keeping. Solid solutions of 1T $MoS_xSe_{(2-x)}$ phases also transform to the 2H-phases with time.[19] There are few reports on the electrocatalytic HER activity of a few solid solutions of $MoS_xSe_{(2-x)}$, but their photocatalytic HER activity has not been explored.[20–22] Photo/electrocatalytic H_2 evolution reactions of $MoSe_xTe_{(2-x)}$ have not been reported. We have investigated a wide range of $MoS_xSe_{(2-x)}$ and $MoSe_xTe_{(2-x)}$ solid solutions for both photocatalytic and electrocatalytic HER activity. In these studies, we have utilized the 2D nanosheets of $MoS_xSe_{(2-x)}$ and $MoSe_xTe_{(2-x)}$, obtained by Li-intercalation in the 2H-phases followed by exfoliation. We have found interesting variations in the catalytic activity as a function of the composition or the Se content, the highest photocatalytic HER activity being 29.6 mmol h^{-1} g^{-1} obtained with $MoS_{0.5}Se_{1.5}$. $MoS_{1.0}Se_{1.0}$ shows the lowest onset potential of -

0.220 V (vs. RHE) compared to the other compositions, illustrating its superior performance as an electrocatalyst. The nanosheets of $MoSe_xTe_{(2-x)}$ also show an increase in photo/electrocatalytic activity with the Se mole fraction.

2. Experimental Section

Reagents and chemicals: Molybdenum powder, sulphur powder, selenium powder, tellurium powder, n-BuLi (1.6 M in hexane) were procured from commercial sources and used as received.

Instrumentation: Powder X-ray diffraction (PXRD) patterns of $MoS_xSe_{(2-x)}$ and $MoSe_xTe_{(2-x)}$ solid solutions were recorded using a PANalytical X-ray diffractometer operating with CuKa radiation (k = 1.5404 A °). SEM images were acquired with a ZEISS Gemini 500 microscope. TEM images were obtained using a FEI Tecnai microscope, operating at a voltage of 200 kV. Raman spectra at different locations of $MoS_xSe_{(2-x)}$ and $MoSe_xTe_{(2-x)}$ solid solutions were collected with a LabRAM HR Raman spectrometer using a 514.5 nm laser as the excitation source.

Synthesis of MoS_2, $MoSe_2$, $MoTe_2$ and $MoS_xSe_{(2-x)}$ /$MoSe_xTe_{(2-x)}$ solid solutions: Pure MoS_2 and $MoSe_2$ were synthesized by mixing Mo metal (2 mmol) with S/Se powder (4 mmol) and heated at 650 ^{0}C for 12 h in a vacuum-sealed quartz tube at a heating rate of 5 ^{0}C min^{-1}.[14] The quartz tube was cooled to room temperature (5 ^{0}C min^{-1}) to obtain black MoS_2/$MoSe_2$ compound. $MoS_xSe_{(2-x)}$ solid solutions were prepared by mixing Mo metal (2 mmol) with

different ratios of S (x = 0.4, 1.0, 1.4,2, 2.6, 3.0, 3.6 mmol) and Se powder ((2-x) = 3.6, 3.0, 2.6,2.0, 1.4, 1.0, 0.4 mmol), following the procedure mentioned earlier.[22]

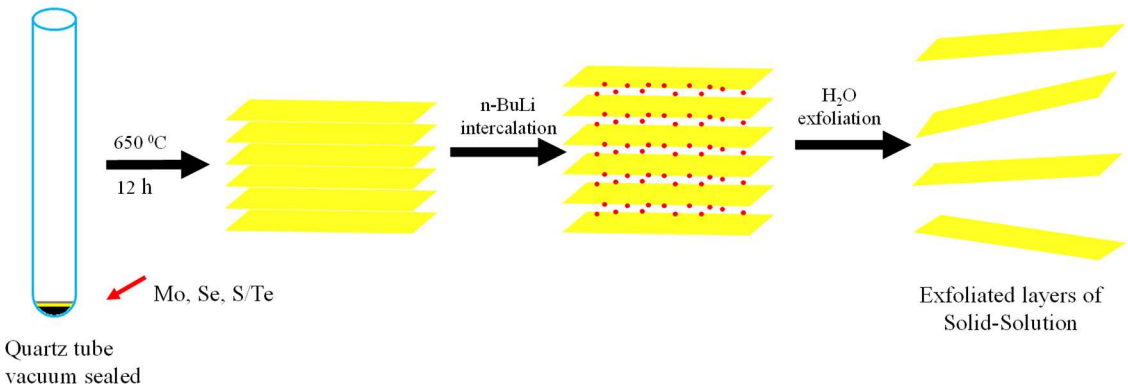

Scheme 1. Schematic of synthesis of $MoS_xSe_{(2-x)}$ /$MoSe_xTe_{(2-x)}$solid solutions and exfoliation in water.

The various compositions of $MoS_xSe_{(2-x)}$ obtained are labelled as $MoS_{0.2}Se_{1.8}$, $MoS_{0.5}Se_{1.5}$, $MoS_{0.7}Se_{1.3}$, $MoS_{1.0}Se_{1.0}$, $MoS_{1.3}Se_{0.7}$, $MoS_{1.5}Se_{0.5}$ and $MoS_{1.8}Se_{0.2}$, respectively, based on the initial precursor ratios. $MoSe_xTe_{(2-x)}$ solid solutions were obtained by mixing Mo metal (2 mmol) with different mole fractions of Se (x = 0.4,1.0, 1.4, 2, 2.6, 3.0, 3.6 mmol) and Te ((2-x) = 3.6, 3.0,2.6, 2.0, 1.4, 1.0, 0.4 mmol) using the above procedure.

The various compositions of $MoSe_xTe_{(2-x)}$ obtained are labelled as $MoSe_{0.2}Te_{1.8}$, $MoSe_{0.5}Te_{1.5}$, $MoSe_{0.7}Te_{1.3}$, $MoSe_{1.0}Te_{1.0}$, $MoSe_{1.3}Te_{0.7}$, $MoSe_{1.5}Te_{0.5}$ and $MoSe_{1.8}Te_{0.2}$, respectively (Various steps in synthesis of solid solutions and exfoliation is depicted in Scheme 1). Photocatalytic HER studies were performed by dispersing 2 mg of $MoS_xSe_{(2-x)}$ /$MoSe_xTe_{(2-x)}$ catalyst in a solution of triethanolamine (TEOA, 15% v/v) in water by sonication in a glass vessel to make total volume to 50 mL. To this Eosin Y (EY) was added, and the mixture was thoroughly purged with N_2. EY here is used as a photosensitizer, while TEOA acts as a

sacrificial agent. The vessel was irradiated with a xenon lamp (400 W) with a steady stirring of the mixture. Three mL of the evolved gas was manually collected from the headspace of the glass vessel and analysed using a gas chromatograph (PerkinElmer ARNL580C) equipped with a thermal conductivity detector. Electrocatalytic HER performance of $MoS_xSe_{(2-x)}$ /$MoSe_xTe_{(2-x)}$ was examined in 0.5 M H_2SO_4 using a conventional three-electrode system with Ag/AgCl and graphite electrodes as the reference and the counter electrode, respectively. The working electrode was fabricated by drop-casting 5 µL of the catalyst-ink (ink was prepared by dispersing 2 mg of $MoS_xSe_{(2-x)}$ /$MoSe_xTe_{(2-x)}$ in 4:1:0.05 ratio of water/IPA/5 wt% Nafion solution) on to a glassy carbon electrode to obtain ~0.140 mg cm^{-2} loading.

3. Results and discussion

We have characterized the $MoS_xSe_{(2-x)}$ and $MoSe_xTe_{(2-x)}$ solid solutions by a variety of methods. PXRD patterns of bulk $MoS_xSe_{(2-x)}$ and those of the pure MoS_2 and $MoSe_2$ are presented in Figure 1a.

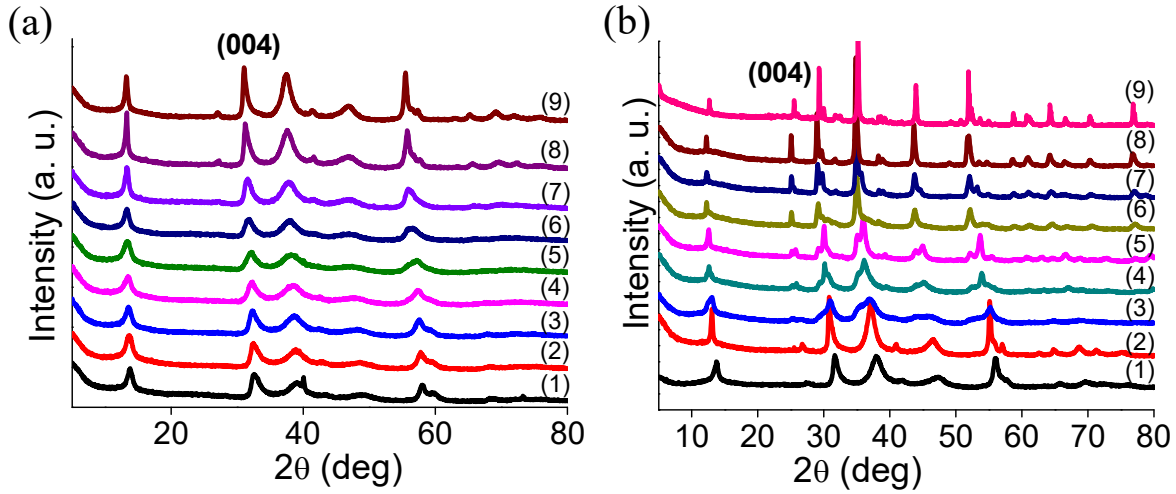

Figure 1. Powder X-ray diffraction pattern of a) bulk $MoS_xSe_{(2-x)}$ solid solutions with different ratios of S and Se; b) bulk $MoSe_xTe_{(2-x)}$ solid solutions with different ratios of Se and Te. In (a) S mole fraction, x = 2 (1), 1.8 (2), 1.5 (3), 1.3 (4), 1.0 (5), 0.7 (6), 0.5 (7), 0.2 (8), 0.0 (9) and in (b) Se mole fraction , x = 2 (1), 1.8 (2), 1.5 (3), 1.3 (4), 1.0 (5), 0.7 (6), 0.5 (7), 0.2(8), 0(9).

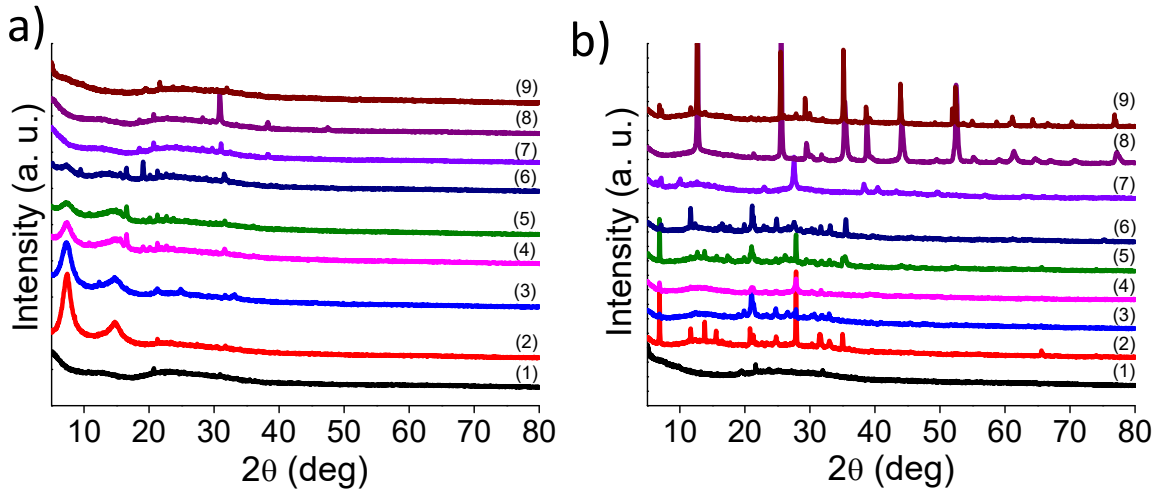

Figure 2. Powder X-ray diffraction pattern of a) Exfoliated $MoS_xSe_{(2-x)}$ solid solutions with different ratios of S and Se; b) Exfoliated $MoSe_xTe_{(2-x)}$ solid solutions with different ratios of Se and Te. In (a) S, x = 2 (1), 1.8 (2), 1.5 (3), 1.3 (4), 1.0 (5), 0.7 (6), 0.5 (7), 0.2 (8), 0 (9) and in (b) Se, x = 2 (1), 1.8 (2), 1.5 (3), 1.3 (4), 1.0 (5), 0.7 (6), 0.5 (7), 0.2(8), 0(9).

The PXRD patterns of pure MoS_2 and $MoSe_2$ match with those reported in the literature (JCPDS card no: 17-744 and 20-757).[23–25] In the Se-dominant $MoS_xSe_{(2-x)}$ solid solutions, the reflections are shifted to lower 2θ values compared to pure MoS_2 due to the larger atomic radius of Se.[26] Figure 1b shows the PXRD patterns of bulk $MoSe_xTe_{(2-x)}$ along with those of pure $MoSe_2$ and $MoTe_2$. With an increase in the Te content, the (002) peak of $MoSe_2$ is shifted to lower 2θ values in addition to the appearance of new peaks due to incorporated Te.[27] The PXRD patterns of the exfoliated $MoS_xSe_{(2-x)}$ and $MoSe_xTe_{(2-x)}$ solid solutions are shown in Figure 2a, b, respectively. We observe a new low angle reflection at 2θ of ~7.35 and 7.0^0 in the case of the exfoliated samples due to increased interlayer spacing because of Li intercalation and exfoliation.[28] Scanning electron microscope (SEM) images of bulk $MoS_{1.0}Se_{1.0}$ and $MoSe_{1.0}Te_{1.0}$, show stacks of platelets of varying thickness (Figure 3a, c). Energy dispersive

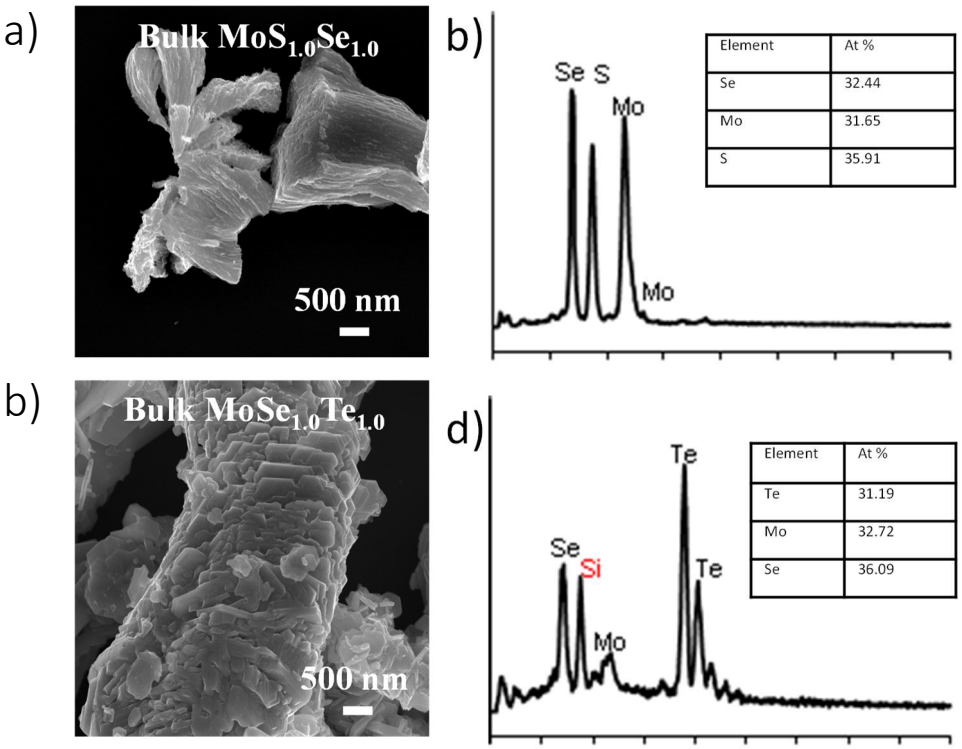

Figure 3. FESEM images of bulk (a) $MoS_{1.0}Se_{1.0}$, (c) $MoSe_{1.0}Te_{1.0}$ solid solutions; and (b) and (d) show corresponding EDS data.

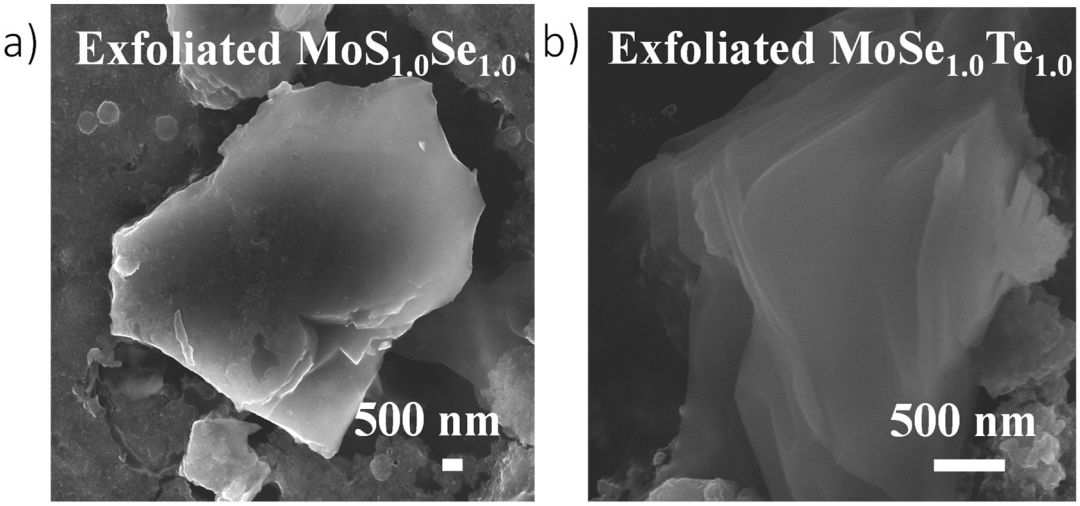

Figure 4. FESEM image of exfoliated a) $MoS_{1.0}Se_{1.0}$ solid solution; b) $MoSe_{1.0}Te_{1.0}$ solid solution.

X-ray analysis (EDS) data of $MoS_{1.0}Se_{1.0}$ and $MoSe_{1.0}Te_{1.0}$ reveal the presence of ~1:1 ratio of the atomic percentage of S:Se and Se:Te (Figure 3b, d). The solid solutions are exfoliated into few-layer nanosheets by the lithium intercalation of bulk, using n-butyllithium, followed by exfoliation in water as described earlier for various TMDs, such as MoS_2 and $MoSe_2$.[16] SEM images of exfoliated $MoS_{1.0}Se_{1.0}$/$MoSe_{1.0}Te_{1.0}$ solid solutions reveal the few-layer nature (Figure 4). As evident from Figure 4a, b, no visible difference in terms of morphology has been noted in the case of exfoliated $MoS_{1.0}Se_{1.0}$ and $MoSe_{1.0}Te_{1.0}$. Raman spectra of bulk and exfoliated samples of MoS_2, $MoSe_2$, $MoTe_2$, $MoS_{1.0}Se_{1.0}$ and $MoSe_{1.0}Te_{1.0}$ are shown in Figure 5a and b. Bulk MoS_2 and $MoSe_2$ display signals only from 2H-form, whereas $MoTe_2$ show peaks due to 1T' (at 123, 160 cm^{-1}) as well as 2H-phase (at 171, 234 cm^{-1}). Bulk $MoS_{1.0}Se_{1.0}$ exhibits peaks due to 2H-MoS_2 (at 382 and 408 cm^{-1}) and 2H-$MoSe_2$ (at 268 cm^{-1}, slightly red shifted compared to pure $MoSe_2$), in accordance with the literature.[29–31]

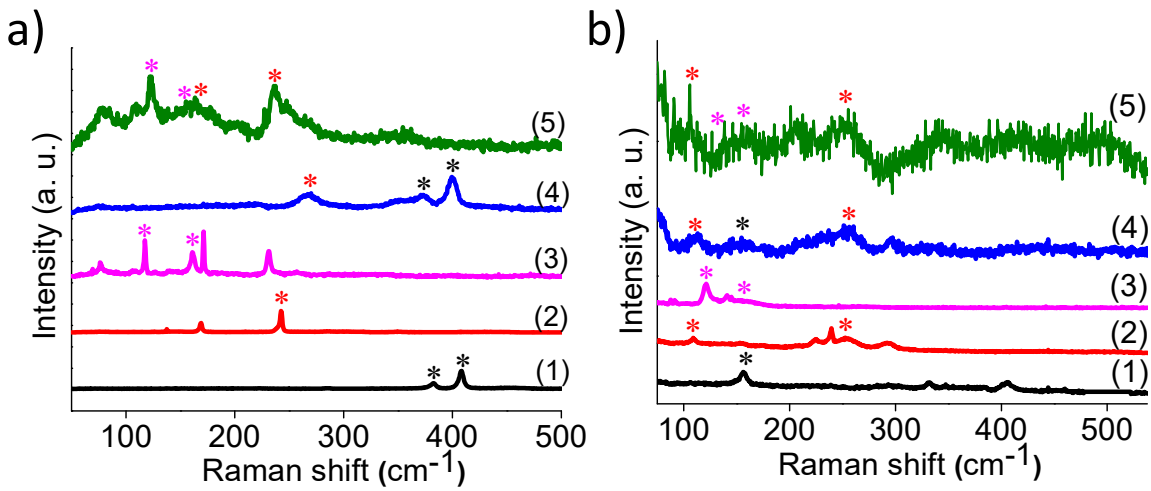

Figure 5. Raman spectra of a) Bulk- MoS_2 (1), $MoSe_2$ (2), $MoTe_2$ (3), $MoS_{1.0}Se_{1.0}$ (4) and $MoSe_{1.0}Te_{1.0}$ (5) solid solutions, b) Exfoliated- MoS_2 (1), $MoSe_2$ (2), $MoTe_2$ (3), $MoS_{1.0}Se_{1.0}$ (4) and $MoSe_{1.0}Te_{1.0}$ (5) solid solutions (Black, red and pink asterisk indicates peaks from MoS_2, $MoSe_2$ and $MoTe_2$ respectively).

Table 1. Photocatalytic HER activity of exfoliated $MoS_xSe_{(2-x)}$ and $MoSe_xTe_{(2-x)}$ solid solutions.

Solid solution	H_2 evolved (mmol h^{-1} g^{-1})	Solid solution	H_2 evolved (mmol h^{-1} g^{-1})
$MoSe_2$	14.83	$MoSe_2$	14.83
$MoS_{0.2}Se_{1.8}$	24.93	$MoSe_{1.8}Te_{0.2}$	5.00
$MoS_{0.5}Se_{1.5}$	29.59	$MoSe_{1.5}Te_{0.5}$	3.20
$MoS_{0.7}Se_{1.3}$	15.77	$MoSe_{1.3}Te_{0.7}$	2.60
$MoS_{1.0}Se_{1.0}$	21.62	$MoSe_{1.0}Te_{1.0}$	1.80
$MoS_{1.3}Se_{0.7}$	27.80	$MoSe_{0.7}Te_{1.3}$	0.73
$MoS_{1.5}Se_{0.5}$	25.82	$MoSe_{0.5}Te_{1.5}$	0.43
$MoS_{1.8}Se_{0.2}$	22.78	$MoSe_{0.2}Te_{1.8}$	0.33
MoS_2	11.1	$MoTe_2$	1.07

Bulk $MoSe_{1.0}Te_{1.0}$ show signals of 2H $MoSe_2$ (at 241 cm^{-1}) and 1T'/2H-$MoTe_2$ (at 160/234 cm^{-1}) (Figure 5a). In the case of exfoliated $MoS_{1.0}Se_{1.0}$, we have observed peaks due to 1T-MoS_2 (156 cm^{-1}) as well as 1T-$MoSe_2$ (106 cm^{-1}) along with weak 2H-MoS_2/$MoSe_2$ (at 382/241 cm^{-1}) signals (Figure 5b), due to the partial 2H→ 1T transition.[32,33] $MoSe_{1.0}Te_{1.0}$ show peaks due to the 1T-form of $MoSe_2$ (at 106 cm^{-1}) as well as the 1T'-$MoTe_2$ (at 123, 160 cm^{-1}) along with those of 2H-$MoSe_2$/$MoTe_2$ (at 241/234 cm^{-1}) signals (Figure 5b).[34,35] For the purpose of brevity, only 1T and 2H Raman peaks of highest intensity are considered for obtaining 1T/2H ratio of solid solutions.

Photocatalytic HER activity of exfoliated $MoS_xSe_{(2-x)}$ and $MoSe_xTe_{(2-x)}$ solid solutions was examined using eosin Y (EY) as the photosensitizer and triethanolamine (TEOA) as a sacrificial agent under visible-light illumination. Figure 6a shows the yields of H_2 evolved with $MoS_xSe_{(2-x)}$ solid solutions. The highest HER activity of 29.6 mmol h^{-1} g^{-1} is obtained with

$MoS_{0.5}Se_{1.5}$. Under similar conditions, pure MoS_2 and $MoSe_2$ show HER activities of only 11.1 and 14.8 mmol h^{-1} g^{-1}, respectively. Variation of HER activity of $MoS_xSe_{(2-x)}$ solid solutions with selenium content is shown in Figure 6b. The HER activity increases progressively with Se mole fraction till $MoS_{0.5}Se_{1.5}$ composition. Beyond this composition, the activity decreases slightly with Se content (Figure 6b, Table 1). Figure 6c shows yields of H_2 evolved with $MoSe_xTe_{(2-x)}$ solid solutions.

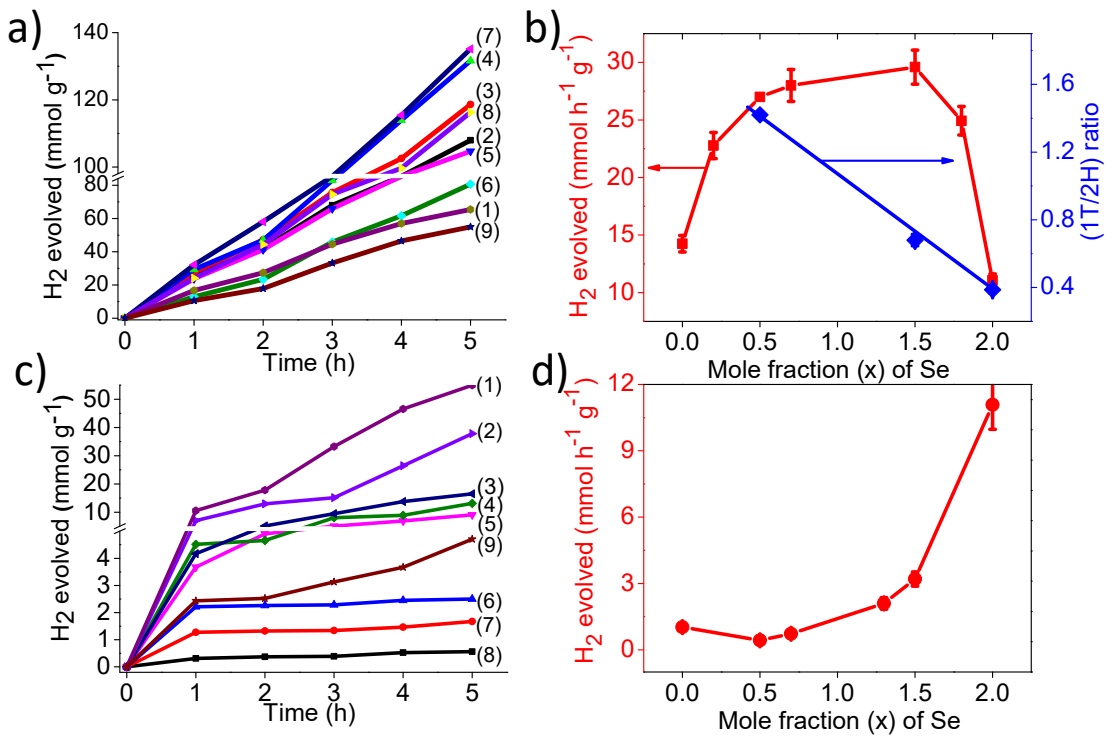

Figure 6. a) Photocatalytic HER activity of $MoS_xSe_{(2-x)}$ solid solutions (MoS_2 (1), $MoS_{1.8}Se_{0.2}$ (2), $MoS_{1.5}Se_{0.5}$ (3), $MoS_{1.3}Se_{0.7}$ (4), $MoS_{1.0}Se_{1.0}$ (5), $MoS_{0.7}Se_{1.3}$ (6), $MoS_{0.5}Se_{1.5}$ (7), $MoS_{0.2}Se_{1.8}$ (8), $MoSe_2$ (9) ; b) Comparison of HER activity with respect to the Se content and 1T/2H ratios for MoSe2 in $MoS_xSe_{(2-x)}$ solid solutions (1T/2H ratios are calculated from Raman spectra); c) Photocatalytic HER activity of $MoSe_xTe_{(2-x)}$ solid solutions ($MoSe_2$ (1), $MoSe_{1.8}Te_{0.2}$ (2), $MoSe_{1.5}Te_{0.5}$ (3), $MoSe_{1.3}Te_{0.7}$ (4), $MoSe_{1.0}Te_{1.0}$ (5), $MoSe_{0.7}Te_{1.3}$ (6), $MoSe_{0.5}Te_{1.5}$ (7), $MoSe_{0.2}Te_{1.8}$ (8), $MoTe_2$ (9) ; b) Comparison of HER activity with respect to the Se content.

The highest HER activity of 5.0 mmol h^{-1} g^{-1} is obtained with Se-rich $MoSe_{1.8}Te_{0.2}$, while pure $MoSe_2$ and $MoTe_2$ show HER activities of 14.8 and 1.1 mmol h^{-1} g^{-1}, respectively. Similar to the $MoS_xSe_{(2-x)}$ nanoflakes, the activity of $MoSe_xTe_{(2-x)}$ nanosheets increases with selenium mole fraction (Figure 6d and table 1). From the photochemical measurements, the performance of parent TMDs is in the order $MoSe_2$ >MoS_2 > $MoTe_2$, in agreement with the literature reports[8,16]. The above result suggests that the incorporation of Se in the MoS_2/$MoTe_2$ lattice plays a positive role in enhancing the photocatalytic HER activity.

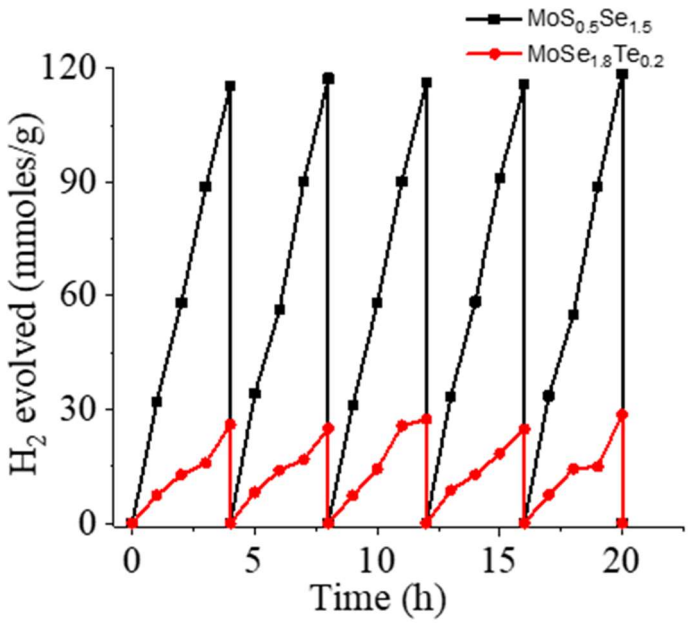

Figure 7. Cyclic stability curves of $MoS_{0.5}Se_{1.5}$ and $MoSe_{1.8}Te_{0.2}$ Solid solutions.

The enhancement in the activity in the case of $MoSe_xTe_{(2-x)}$ with selenium mole fraction is however, lower compared to $MoS_xSe_{(2-x)}$. Cycling studies on $MoS_{0.5}Se_{1.5}$ and $MoSe_{1.8}Te_{0.2}$ showed stable H_2 evolution over long periods (Figure 7), indicating that the solid solutions are robust.

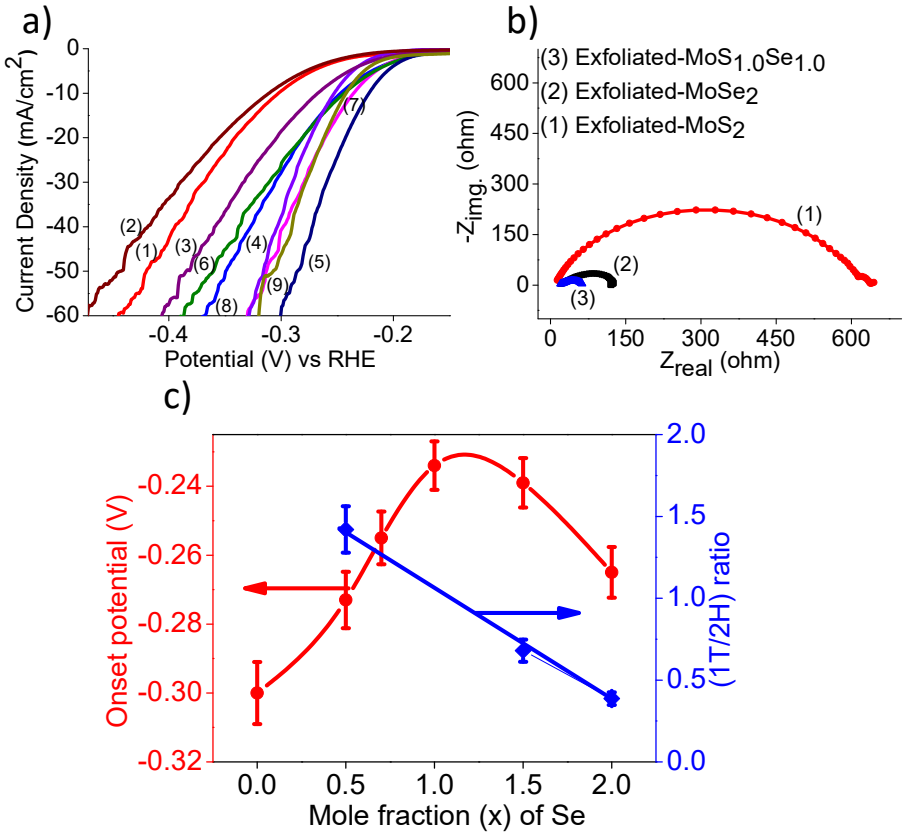

Figure 8. Electrocatalytic HER activity of $MoS_xSe_{(2-x)}$ solid solutions a) Linear sweep voltammetry curves (LSV) (MoS_2 (1), $MoS_{1.8}Se_{0.2}$ (2), $MoS_{1.5}Se_{0.5}$ (3), $MoS_{1.3}Se_{0.7}$ (4), $MoS_{1.0}Se_{1.0}$ (5), $MoS_{0.7}Se_{1.3}$ (6), $MoS_{0.5}Se_{1.5}$ (7), $MoS_{0.2}Se_{1.8}$ (8), $MoSe_2$ (9) ; b) Nyquist plot; c) Comparison of onset potential with respect to the Se content and 1T/2H ratios for $MoSe_2$ in $MoS_xSe_{(2-x)}$ solid solutions (1T/2H ratios are calculated from Raman spectra).

Encouraged by the superior photocatalytic HER activity of the $MoS_xSe_{(2-x)}$ and $MoSe_xTe_{(2-x)}$, we have examined them for electrocatalytic HER using a conventional three electrode cell with 0.5 M H_2SO_4 as an electrolyte. The electrocatalytic performance was examined using linear sweep voltammetry (LSV), electrochemical impedance spectroscopy (EIS) measurements. Polarization curves of $MoS_xSe_{(2-x)}$ along with those of MoS_2 and $MoSe_2$ are shown in Figure 8a. The onset potential obtained for $MoS_{1.0}Se_{1.0}$ (-0.220 V) is lower than that of other

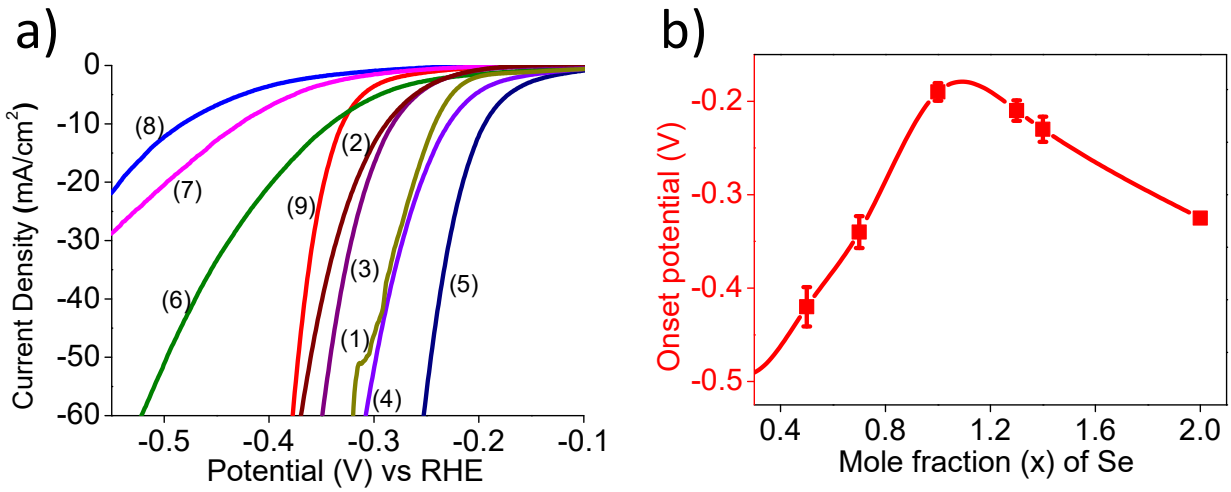

Figure 9. Electrocatalytic HER activity of exfoliated $MoSe_xTe_{(2-x)}$ solid solutions ($MoSe_2$ (1), $MoSe_{1.8}Te_{0.2}$ (2), $MoSe_{1.5}Te_{0.5}$ (3), $MoSe_{1.3}Te_{0.7}$ (4), $MoSe_{1.0}Te_{1.0}$ (5), $MoSe_{0.7}Te_{1.3}$ (6), $MoSe_{0.5}Te_{1.5}$ (7), $MoSe_{0.2}Te_{1.8}$ (8), $MoTe_2$ (9) ; a) Linear sweep voltammetry curves (LSV); b) HER activity in relation to Se content.

Table 2. Electrocatalytic HER activity of exfoliated $MoS_xSe_{(2-x)}$ and $MoSe_xTe_{(2-x)}$ solid solutions.

Solid solution	Onset potential @10 mA/cm^2	Solid solution	Onset potential @10 mA/cm^2
$MoSe_2$	-0.24	$MoSe_2$	-0.24
$MoS_{0.2}Se_{1.8}$	-0.31	$MoSe_{1.8}Te_{0.2}$	-0.28
$MoS_{0.5}Se_{1.5}$	-0.273	$MoSe_{1.5}Te_{0.5}$	-0.27
$MoS_{0.7}Se_{1.3}$	-0.255	$MoSe_{1.3}Te_{0.7}$	-0.22
$MoS_{1.0}Se_{1.0}$	-0.220	$MoSe_{1.0}Te_{1.0}$	-0.19
$MoS_{1.3}Se_{0.7}$	-0.249	$MoSe_{0.7}Te_{1.3}$	-0.34
$MoS_{1.5}Se_{0.5}$	-0.239	$MoSe_{0.5}Te_{1.5}$	-0.42
$MoS_{1.8}Se_{0.2}$	-0.25	$MoSe_{0.2}Te_{1.8}$	-0.48
MoS_2	-0.30	$MoTe_2$	-0.32

compositions as well as pure MoS_2 (-0.30 V) and $MoSe_2$ (-0.240 V). Furthermore, the charge-transfer resistance of $MoS_{1.0}Se_{1.0}$ is minimal suggesting fast electron transport to the catalytically active sites in comparison to parent MoS_2 or $MoSe_2$ (Figure 8b). Figure 8c shows the variation of onset potential of $MoS_xSe_{(2-x)}$ with selenium content. The onset potential value decreases with the Se mole fraction up to $MoS_{1.0}Se_{1.0}$ composition (Figure 8c and table2). In the case of $MoSe_xTe_{(2-x)}$, we obtained the lowest onset potential of -0.190 V with the $MoSe_{1.0}Te_{1.0}$ (Figure 9a, table 2). The charge-transfer resistance is least with this composition, due to its better electrocatalytic HER activity. It is interesting that same selenium mole fraction shows the lowest onset potential amongst $MoS_xSe_{(2-x)}$ as well (Figures 8c and 9b). Figure 8c shows how the 1T/2H-$MoSe_2$ ratio of $MoS_xSe_{(2-x)}$ and $MoSe_xTe_{(2-x)}$ varies with the Se mole fraction. The results suggest that several factors, such as change in the band gap as well as presence of certain defects could play a role in determining the HER activity of solid solutions.[21] It is also possible that the alloys possess more active edge sites than the parent materials. Besides other factors influencing HER, the best performance of Se-rich compositions may be ascribed to their efficient electronic conductivity.[36] The $MoS_{1.0}Se_{1.0}$ solid solution is stable under the electrochemical HER conditions as accessed by LSV curves before and after running cyclic voltammetry (CV) up to 1000 cycles (Figure 10). Table 3 shows the comparison of the onset potential values (@10 mA cm^{-2}) of exfoliated $MoS_{1.0}Se_{1.0}$ and $MoSe_{1.0}Te_{1.0}$ with some of the similar alloys reported in the literature. Evidently, negligible performance decay is observed after the 1000 cycles, indicating the outstanding stability of $MoS_{1.0}Se_{1.0}$ solid solution.

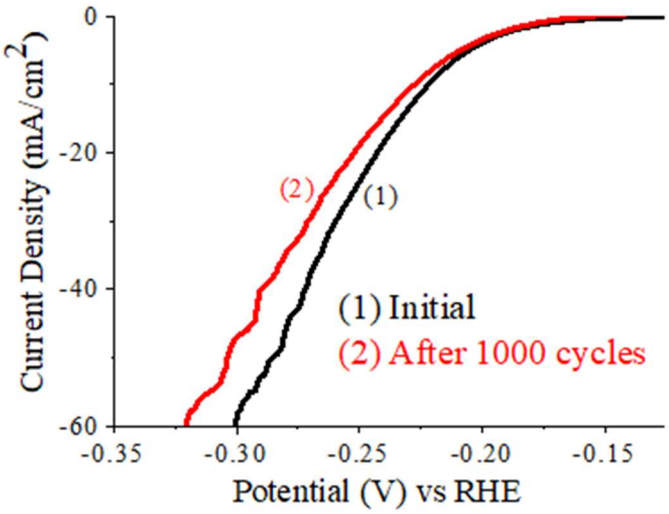

Figure 10. LSV plot (between −0.35 V and -0.15 V) before and after 1000 cycles of CV for $MoS_{1.0}Se_{1.0}$ solid solutions.

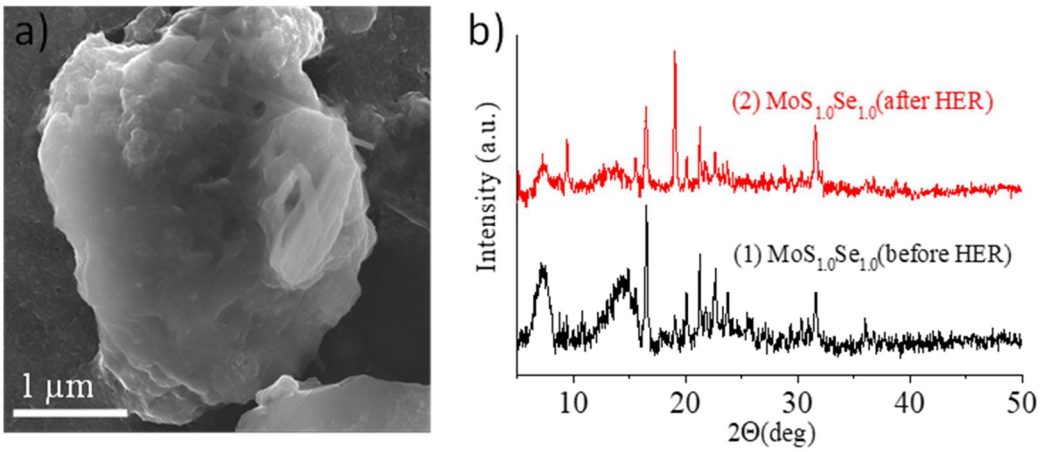

Figure 11. a) FESEM image of exfoliated $MoS_{1.0}Se_{1.0}$ solid solution after 1000 cycles of CV. b) PXRD pattern of exfoliated $MoS_{1.0}Se_{1.0}$ electrocatalyst initially (1, black) and after 1000 cycles (2, red) of CV.

Table 3. Comparison of onset potential values (@10 mA cm^{-2}) of exfoliated $MoS_{1.0}Se_{1.0}$ and $MoSe_{1.0}Te_{1.0}$ with some of the similar alloys reported in the literature.

Solid solutions	Onset potential (V vs. RHE) @10 mA cm^{-2}
$MoSe_2@MoS_2$[37]	-0.89
$MoS_{1.0}Se_{1.0}$[21]	-0.3
MoSSe[20]	-0.03
$MoS_{1.0}Se_{1.0}$[22]	-0.19
$MoS_{0.94}P_{0.53}$[38]	-0.19
$MoSe_{0.35}Te_{1.65}$[39]	-0.24
$MoSe_{0.17}Te_{1.83}$[39]	-0.19
$MoS_{1.0}Se_{1.0}$[a]	-0.22
$MoSe_{1.0}Te_{1.0}$[a]	-0.20

[a]Solid solutions reported in the present work.

Furthermore, structural changes of $MoS_{1.0}Se_{1.0}$ after the durability tests were also evaluated by SEM and PXRD measurements (Figure 11a, b). It can be seen that there were no noticeable changes in terms of morphology (Figure 11a) as well as in the PXRD reflections (Figure 11b) even after 1000 cycles. These observations clearly demonstrate that the catalyst is chemically stable.

4. Conclusions

In conclusion, exfoliated $MoS_xSe_{(2-x)}$ and $MoSe_xTe_{(2-x)}$ solid solutions exhibit photo/electrocatalytic HER activity by splitting water, wherein the photocatalytic HER activity increases with the selenium mole fraction. Se-rich $MoS_{0.5}Se_{1.5}$ exhibits the highest photocatalytic HER activity among the $MoS_xSe_{(2-x)}$ solid solutions. These solid solutions also exhibit satisfactory electrocatalytic HER activity with low onset potentials in the range of -0.340 to -0.190 mV.

5. References

[1] C. N. R. Rao, A. K. Sood, K. S. Subrahmanyam, A. Govindaraj, *Angew. Chemie - Int. Ed.* **2009**, *48*, 7752.

[2] A. K. Geim, K. S. Novoselov, *Nat. Mater.* **2007**, *6*, 183.

[3] C. N. R. Rao, A. K. Sood, R. Voggu, K. S. Subrahmanyam, *J. Phys. Chem. Lett.* **2010**, *1*, 572.

[4] P. Vishnoi, U. Gupta, R. Pandey, C. N. R. Rao, *J. Mater. Chem. A* **2019**, *7*, 6631.

[5] C. R. Ryder, J. D. Wood, S. A. Wells, Y. Yang, D. Jariwala, T. J. Marks, G. C. Schatz, M. C. Hersam, *Nat. Chem.* **2016**, *8*, 597.

[6] P. Vishnoi, M. Mazumder, S. K. Pati, C. N. R. Rao, *New J. Chem.* **2018**, *42*, 14091.

[7] H. S. S. Ramakrishna Matte, A. Gomathi, A. K. Manna, D. J. Late, R. Datta, S. K. Pati, C. N. R. Rao, *Angew. Chemie - Int. Ed.* **2010**, *49*, 4059.

[8] U. Gupta, C. N. R. Rao, *Nano Energy* **2017**, *41*, 49.

[9] K. C. Knirsch, N. C. Berner, H. C. Nerl, C. S. Cucinotta, Z. Gholamvand, N. McEvoy, Z. Wang, I. Abramovic, P. Vecera, M. Halik, S. Sanvito, G. S. Duesberg, V. Nicolosi, F. Hauke, A. Hirsch, J. N. Coleman, C. Backes, *ACS Nano* **2015**, *9*, 6018.

[10] B. Chakraborty, H. S. S. R. Matte, A. K. Sood, C. N. R. Rao, *J. Raman Spectrosc.* **2013**, *44*, 92.

[11] A. Splendiani, L. Sun, Y. Zhang, T. Li, J. Kim, C. Chim, G. Galli, F. Wang, *Nano Lett.* **2010**, *10*, 1271.

[12] G. Eda, H. Yamaguchi, D. Voiry, T. Fujita, M. Chen, M. Chhowalla, *Nano Lett.* **2011**, *11*, 5111.

[13] Y. K. Ryu, R. Frisenda, A. Castellanos-gomez, *Chem. Commun.* **2019**, *55*, 11498.

[14] M. K. Jana, A. Singh, A. Sampath, C. N. R. Rao, U. V Waghmare, Z. Anorg. Allg. Chem. **2016**, *23*, 1386.

[15] U. Maitra, U. Gupta, M. De, R. Datta, A. Govindaraj, C. N. R. Rao, *Angew. Chemie -*

Int. Ed. **2013**, *52*, 13057.

[16] U. Gupta, B. S. Naidu, U. Maitra, A. Singh, S. N. Shirodkar, U. V Waghmare, C. N. R. Rao, *APL Mater.* **2014**, *2*, 092802.

[17] U. Gupta, D. S. Narang, *Bull. Mater. Sci.* **2017**, *40*, 329.

[18] R. Singh, U. Gupta, V. S. Kumar, M. Ayyub, U.V. Waghmare, CNR Rao, *ChemPhysChem* **2019**, *20*, 1728.

[19] N.K. Singh, A. Soni, R. Singh, U. Gupta, K. Pramoda, CNR Rao, J.Chem. Sci. **2018**, 130, 131.

[20] Q. Gong, L. Cheng, C. Liu, M. Zhang, Q. Feng, H. Ye, M. Zeng, L. Xie, Z. Liu, Y. Li, *ACS Catal.* **2015**, *5,* 2213.

[21] B. Konkena, J. Masa, W. Xia, M. Muhler, W. Schuhmann, *Nano Energy* **2016**, *29*, 46.

[22] V. Kiran, D. Mukherjee, R. N. Jenjeti, S. Sampath, *Nanoscale* **2014**, *6*, 12856.

[23] L. Li, Z. Qin, L. Ries, S. Hong, T. Michel, J. Yang, C. Salameh, M. Bechelany, P. Miele, D. Kaplan, M. Chhowalla, D. Voiry, *ACS Nano* **2019**, 13, 6824.

[24] A. Eftekhari, *Appl. Mater. Today* **2017**, *8*, 1.

[25] D. Qi, C. Han, X. Rong, X. Zhang, M. Chhowalla, A. T. S. Wee, W. Zhang, *ACS Nano* **2019**, *13*, 9464.

[26] S. Zhang, Z. Huang, Z. Wen, L. Zhang, J. Jin, R. Shahbazian-yassar, J. Yang, *Nano Lett.* **2017**, *17*, 3518.

[27] M. K. Agarwal, P. D. Patel, R. M. Joshi, V. V Rao, *Cryst. Res. Technol.* **1990**, *25*, 467

[28] K. D. Rasamani, F. Alimohammadi, Y. Sun, Mater. Today **2017**, *20,* 83.

[29] H. I. Lee, H. Yu, C. K. Rhee, Y. Sohn, *Appl. Surf. Sci.* **2019**, *489*, 976.

[30] J. Mann, Q. Ma, P. M. Odenthal, M. Isarraraz, D. Le, E. Preciado, D. Barroso, K. Yamaguchi, G. V. S. Palacio, A. Nguyen, T. Tran, M. Wurch, A. Nguyen, V. Klee, S. Bobek, D. Sun, T. F. Heinz, T. S. Rahman, R. Kawakami, L. Bartels, **2014**, *2*, 1399.

[31] H. He, D. Huang, Q. Gan, J. Hao, S. Liu, Z. Wu, W. K. Pang, B. Johannessen, Y. Tang, J. Luo, H. Wang, Z. Guo, *ACS Nano* **2019**, *13*, 11843.

[32] S. Chen, C. Zheng, M. S. Fuhrer, J. Yan, Nano Lett. **2015**, *15*, 252.

[33] M. Yang, X. Cheng, Y. Li, Y. Ren, M. Liu, Z. Qi, *Appl. Phys. Lett.* **2017**, *110*, 093108.

[34] V. Mode, F. Mote, M. Yamamoto, S. T. Wang, M. Ni, Y. Lin, S. Li, S. Aikawa, **2014**, 3895.

[35] D. O. Dumcenco, K. Y. Chen, Y. P. Wang, Y. S. Huang, K. K. Tiong, *J. Alloys Compd.* **2010**, *506*, 940.

[36] K. S. Bhat, H. S. Nagaraja, *Int. J. Hydrogen Energy* **2019**, *44*, 17878.

[37] X. Ren, Q. Wei, P. Ren, Y. Wang, R. Chen, *Mater. Lett.* **2018**, *231*, 213.

[38] R. Ye, P. Angel-vicente, Y. Liu, M. J. Arellano-jimenez, Z. Peng, T. Wang, Y. Li, B. I. Yakobson, S. Wei, M. J. Yacaman, J. M. Tour, *Adv. Mater.* **2016**, *28*, 1427.

[39] T. Kosmala, H. C. Diaz, H. Komsa, Y. Ma, A. V Krasheninnikov, M. Batzill, S. Agnoli, *Adv. Energy Mater.* **2018**, *8*, 1800031.

Part III

Nanocomposites of 1D MoS_2 with Polymer-Functionalized Nanotubes of Carbon and Borocarbonitride, and Their HER Activity

Chapter III

Nanocomposites of 1D MoS_2 with Polymer-Functionalized Nanotubes of Carbon and Borocarbonitride, and Their HER Activity

Summary*

Nanocomposites formed by carboxyl-functionalized MoS_2 nanotubes with poly(diallyldimethylammonium chloride) (PDDA, described as P)-modified single-walled carbon nanotubes (SWCNT) and borocarbonitride nanotubes (BCNNT) have been prepared by a solution-phase flocculation of 1D nanotubes. The nanocomposites show higher photocatalytic and electrocatalytic HER activities compare to the individual constituents, where the H_2 yield improves with the MoS_2 nanotube proportion. The maximum H_2 evolution rate achieved is 7475 μmol g^{-1} h^{-1} in the nanocomposite of MoS_2–P.SWCNT with a MoS_2–P.SWCNT proportion of 3:1, whereas the corresponding physical mixture exhibits only 3112 μmol g^{-1} h^{-1}. The MoS_2–P.SWCNT (3:1) nanocomposite also shows superior electrocatalytic H_2 evolution with an onset potential of 80 mV (vs RHE). The MoS_2–P.BCNNTcomposite exhibits a somewhat lower H_2 evolution rate. Electrostatic stacking of 1D MoS_2 nanotubes with SWCNT/BCNNT appears to be a valuable strategy for HER and related catalytic reaction.

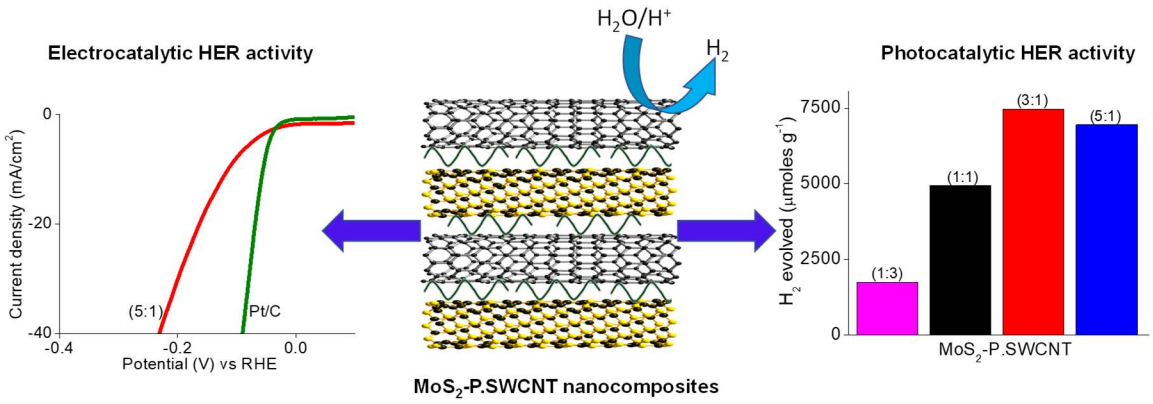

* A paper based on this work has been published as D.C. Binwal *et al.* ACS Appl. Energy Mater., 2021, 4, 2339.

1. Introduction

The MoS_2-based nanomaterials have been extensively investigated because of their potential applications in sensors,[1–3] batteries,[4–7] and water reduction reactions.[8–12] Although these properties are noteworthy, they are impeded by the low electrical conductivity and limited surface area of MoS_2.[13,14] Hence, the coupling of MoS_2 nanostructures with conductive additives such as carbon nanotubes (CNTs) and graphene has become an effective strategy to resolve the above issues.[15] For instance, MoS_2 nanoparticles grown on graphene displays superior electrocatalytic activity in hydrogen evolution reaction (HER) through more exposed edge sites and reduced charge transfer resistance because of the underlying conductive carbon networks.[16] In addition, layered assemblies of 2D MoS_2 with graphene,[17] C_3N_4,[18] and BCN[19,20] have shown to exhibit electrocatalytic H_2 evolution at par with Pt and reasonably good photocatalytic activity. Recently, inorganic nanotubes of MoS_2 have been prepared that possess entirely different properties compared to the 2D analogues.[21] MoS_2 nanotubes are semiconducting[21] whereas single-walled carbon nanotubes (SWCNT) can possess metallic or semiconducting properties as a function of helicity and diameter,[22–24] and coupling the two would be expected to result new features. In this context, we considered it is most worthwhile to prepare a MoS_2 nanotube composite with other 1D carbon nanotubes.

We have prepared the nanocomposites of negatively charged MoS_2 nanotubes with PDDA-functionalized SWCNT and borocarbonitride nanotubes (BCNNT) following the procedure of Xiong *et al.,*[25,26] and studied their photo/electrocatalytic H_2 evolution. The conjugation of MoS_2 nanotubes with 4-mercaptobenzoic acid (MBA) yields negative charge and the noncovalent functionalization of SWCNT and BCNNT with the polymer PDDA makes the nanotube surface positive. In the presentation that follows, nanocomposites prepared by

reacting carboxyl-functionalized MoS_2 nanotubes (MoS_2–C_6H_4COOH) with PDDA-functionalized SWCNT and BCNNT, designated as MoS_2–P.SWCNT and MoS_2–P.BCNNT respectively. In Table 1, we have listed the range of MoS_2–P.SWCNT and MoS_2–P.BCNNT nanocomposites synthesized by electrostatic restacking approach. These nanocomposites of MoS_2–P.SWCNT (3:1, 5:1) with a high MoS_2 nanotube proportion display higher H_2 evolution in relation to (1:3, 1:1) compositions. Photocatalytic H_2 evolution of MoS_2–P.SWCNT (3:1) nanocomposite is noteworthy with an activity of 7475 μmol g^{-1} h^{-1}. MoS_2–P.SWCNT (3:1) also exhibits good electrocatalytic H_2 evolution showing an onset potential of 80 mV (vs RHE).

Table 1. Nanocomposites of MoS_2–P.SWCNT and MoS_2– P.BCNNT Prepared.

Negatively charged precursor (wt %)	Positively charged precursor (wt %)	Product
MoS_2-$C_6H_4COOH^a$ (1)	P.SWCNT^b (3)	MoS_2-P.SWCNT (1:3)
MoS_2-$C_6H_4COOH^a$ (1)	P.SWCNT^b (1)	MoS_2-P.SWCNT (1:1)
MoS_2-$C_6H_4COOH^a$ (3)	P.SWCNT^b (1)	MoS_2-P.SWCNT (3:1)
MoS_2-$C_6H_4COOH^a$ (5)	P.SWCNT^b (1)	MoS_2-P.SWCNT (5:1)
MoS_2-$C_6H_4COOH^a$ (1)	P.BCNNT^c (3)	MoS_2-P.BCNNT (1:3)
MoS_2-$C_6H_4COOH^a$ (1)	P.BCNNT^c (1)	MoS_2-P.BCNNT (1:1)
MoS_2-$C_6H_4COOH^a$ (3)	P.BCNNT^c (1)	MoS_2-P.BCNNT (3:1)
MoS_2-$C_6H_4COOH^a$ (5)	P.BCNNT^c (1)	MoS_2-P.BCNNT (5:1)

[a]4-Mercaptobenzoic acid functionalized MoS_2 (MoS_2-C_6H_4COOH).
[b]Poly(diallyldimethylammonium chloride)-functionalized single-walled carbon nanotube (P.SWCNT).
[c]Poly(diallyldimethylammonium chloride)-functionalized borocarbonitride nanotube (P.BCNNT).

2. Experimental Section

Carboxyl-functionalized MoS_2 nanotubes were prepared by dispersing pristine MoS_2 nanotubes[21] (20 mg, procured from the Holon Institute of Technology) in anhydrous dimethylformamide (DMF, 10 mL), and then 4-mercaptobenzoic acid (MBA, 20 mg) was

added under steady stirring.[27] The resultant carboxyl-functionalized nanotubes were separated by centrifugation, repeatedly washed with DMF, and dried in a vacuum. PDDA-functionalized SWCNT were obtained by following the earlier reports.[20,25] To the acid-functionalized SWCNT, PDDA (0.2 mL) and hydrazine hydrate (15 µL) were added and the resultant solution was heated at 90 °C. Prior to PDDA modification, carboxyl-functionalized SWCNT were obtained by refluxing pristine SWCNT (50 mg, Sigma-Aldrich) with HNO_3 (2 mL) and H_2SO_4 (2mL) mixture, following the earlier reports.[28] For the preparation of MoS_2−P.SWCNT composites, P.SWCNT was added dropwise to the carboxyl-functionalized MoS_2 under constant stirring, which results in the instant flocculation. The obtained flocculation is repeatedly washed with water and dried in a vacuum oven. To prepare MoS_2−P.BCNNT composites, we have used PDDA-functionalized BCNNT instead of P.SWCNT and repeated the above-mentioned repeated.[20,26,29]

Photocatalytic HER experiments were carried out in an aqueous solution of triethanolamine (TEOA, 15% v/v) and eosin Y (EY). The MoS_2−P.SWCNT or MoS_2−P.BCNNT was dispersed in aqueous solution of TEOA (15% v/v; 8 mL) by sonication in a glass vessel. To the resultant dispersion EY (1 mL, 10 mg/mL) was added and the dispersion was irradiated with a xenon lamp (400 W). The evolved H_2 gas (3 mL) was analysed manually by injecting into a PerkinElmer gas chromatograph ARNL 580C.

Electrocatalytic H_2 evolution was carried using a conventional three-electrode setup where Hg/Hg_2Cl_2 and graphite were used as reference and counter electrode, respectively. The working electrode was prepared by drop-casting 5 µL of catalyst ink, obtained by dispersing 2 mg of the nanocomposite in mixture of water, isopropyl alcohol, and 5 wt % Nafion (4:1:0.05, v/v/v), onto a glassy carbon electrode and dried in a desiccator.

3. Results and discussion

Schematic of the MoS_2−P.SWCNT and MoS_2−P.BCNNTcomposites obtained by solution-phase restacking of negatively charged MoS_2 nanotubes with positively charged SWCNT and BCNNT is shown in Scheme 1. Defect functionalization of the pristine MoS_2 nanotubes with MBA generates negative charges on either side of the tube due to carboxyl functional groups. Secondly, the surface modification of SWCNT/BCNNT with PDDA makes these nanotubes positively charged. To obtain the MoS_2−P.SWCNT nanocomposites, P.SWCNT suspension was added dropwise to the carboxyl-functionalized MoS_2 nanotube (MoS_2−C_6H_4COOH) solution under constant stirring conditions using a precalculated proportion of the reactants (see the Experimental Section for more details). The MoS_2−P.SWCNT mentioned in the text denotes the 1:1 (wt%) content of the MoS_2 nanotubes and SWCNT, unless otherwise mentioned. Similarly, MoS_2−P.BCNNT composites are prepared by adding positively charged P.BCNNT to the MoS_2−C_6H_4COOH suspension. We have established the identity of the electrostatically stacked hetero-nanotubes by several approaches. The pristine SWCNT and BCNNT exhibit negative zeta (ζ) potentials of −33.9 and −25.4 mV, respectively, because of the residual oxygen functionalities, whereas the P.SWCNT and P.BCNNT show positive ζ potentials of +27.8 and +30.2 mV, respectively because of the ammonium groups of the PDDA (Table 2). With the addition of carboxyl-functionalized MoS_2 nanotube (MoS_2−C_6H_4COOH, ζ of −38.3 mV) to P.SWCNT and P.BCNNT, the ζ potential shifts to a neutral value, as shown in Figure 1a, b, indicating the stacking of MoS_2 nanotube on P.SWCNT and P.BCNNT surface by the electrostatic interaction. The FESEM and elemental mapping images of MoS_2−P.SWCNT nanocomposite reveal that MoS_2 nanotubes are efficiently intercalated between the bundles of P.SWCNT (Figure 3b and Figure 2). The FESEM and TEM image of

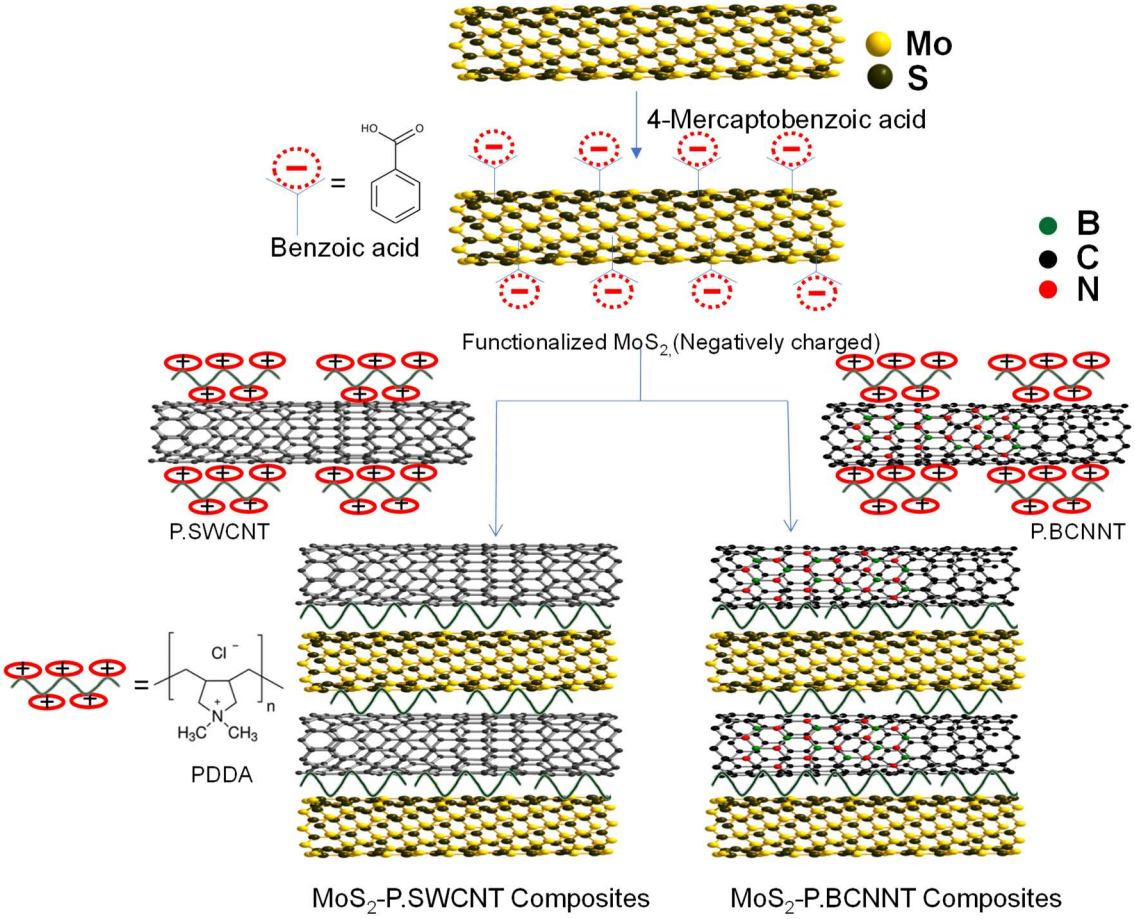

Scheme 1. Synthetic strategy for electrostatically stacked MoS_2-P.SWCNT and MoS_2-P.BCNNT nanocomposites.

Table 2. Zeta potential values of MoS_2-P.SWCNT and MoS_2-P.BCNNT nanocomposites.

Compound	Zeta potential (mV)	Compound	Zeta potential (mV)
MoS_2-C_6H_4COOH	-38.3	MoS_2-C_6H_4COOH	-38.3
SWCNT	-33.9	BCNNT	-25.4
P.SWCNT	+27.8	P.BCNNT	+30.2
MoS_2-P.SWCNT (1:3)	+12.2	MoS_2-P.BCNNT (1:3)	+16.2
MoS_2-P.SWCNT (1:1)	+2.7	MoS_2-P.BCNNT (1:1)	+3.9
MoS_2-P.SWCNT (3:1)	-3.5	MoS_2-P.BCNNT (3:1)	-5.6
MoS_2-P.SWCNT (5:1)	-4.6	MoS_2-P.BCNNT (5:1)	-9.8

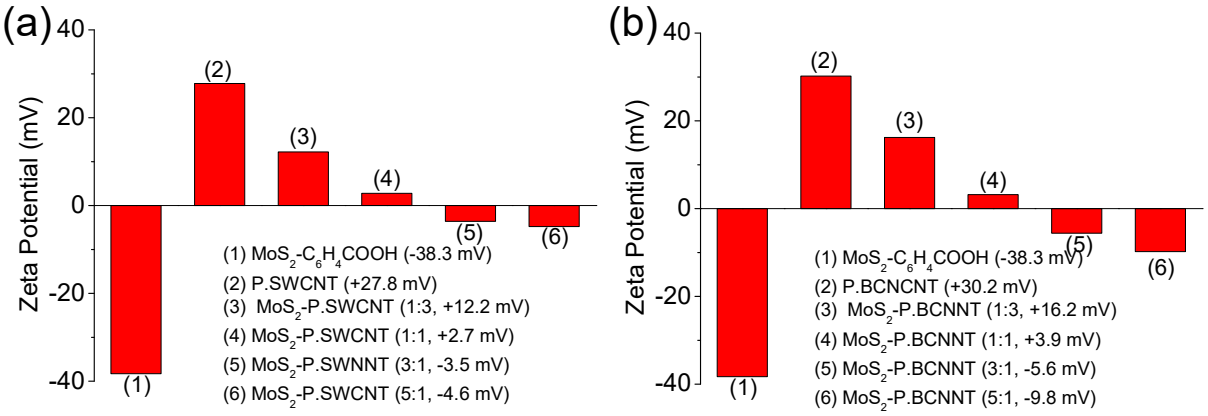

Figure 1. ζ-potential plots of the (a) (1) MoS_2-C_6H_4COOH, (2) P.SWCNT, (3) MoS_2-P.SWCNT (1:3), (4) MoS_2-P.SWCNT (1:1), (5) MoS_2-P.SWCNT (3:1) and (6) MoS_2-P.SWCNT (5:1) nanocomposites. (b) (1) MoS_2-C_6H_4COOH, (2) P.BCNNT, (3) MoS_2-P.BCNNT (1:3), (4) MoS_2-P.BCNNT (1:1), (5) MoS_2-P.BCNNT (3:1) and (6) MoS_2-P.BCNNT (5:1) nanocomposites.

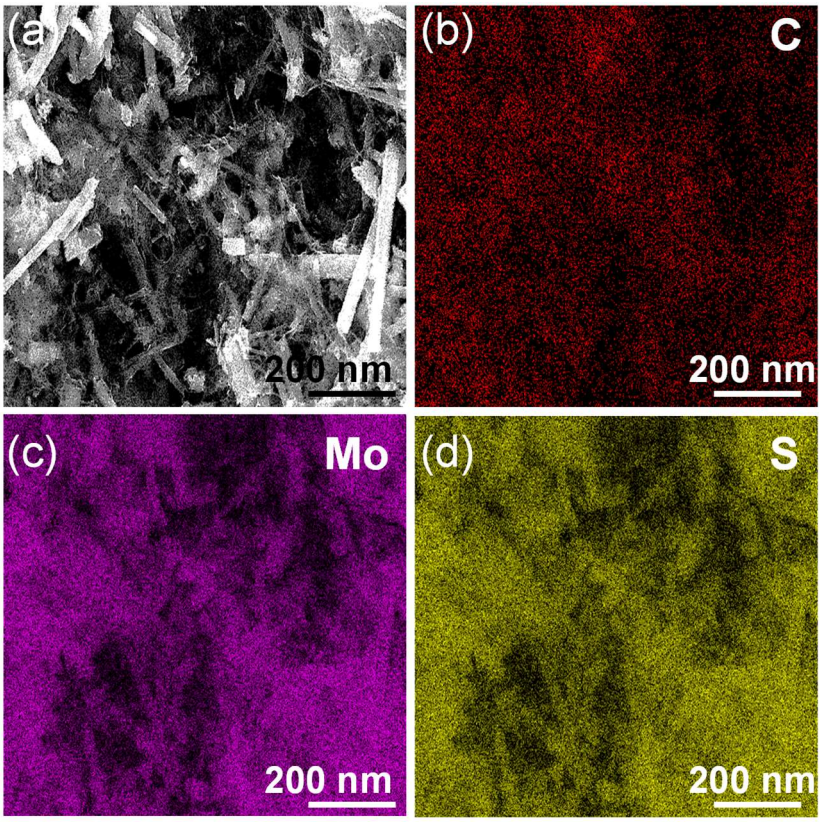

Figure 2. Elemental mapping image of MoS_2-P.SWCNT(1:1) nanocomposite showing the uniform distribution of C, Mo, and S in the nanocomposite.

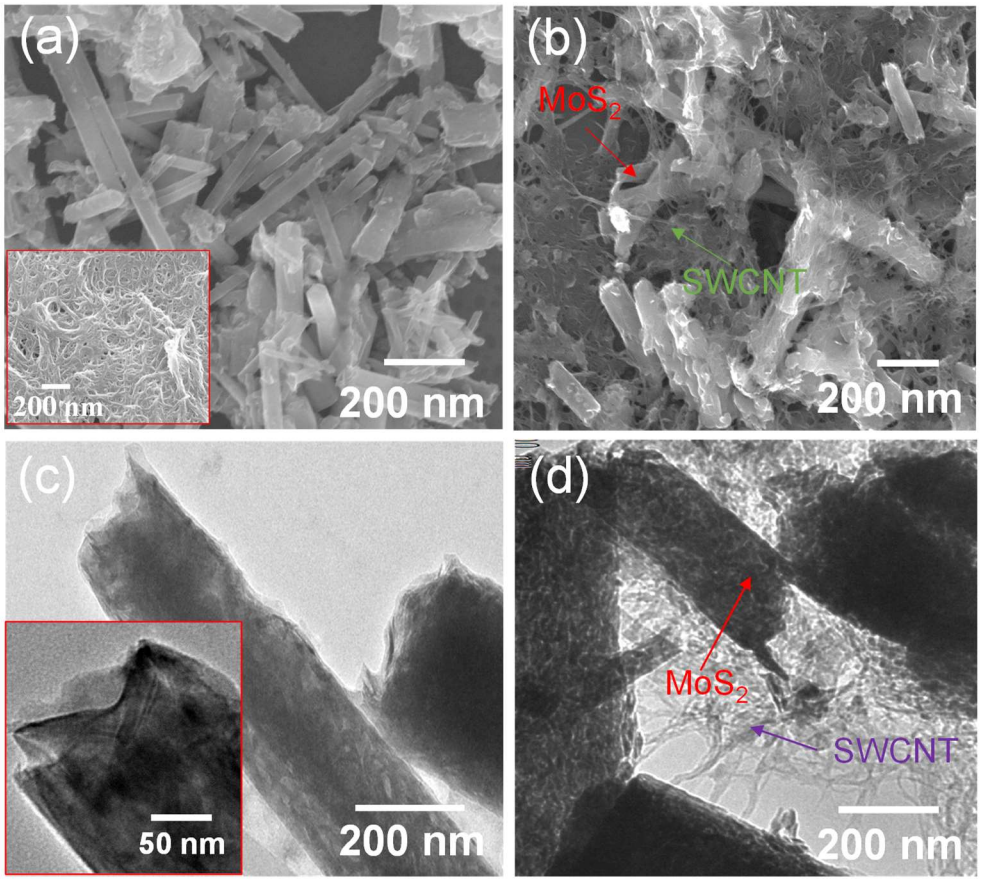

Figure 3. FESEM image (a) MoS_2 nanotubes (inset shows FESEM image of SWCNT) and (b) MoS_2-P.SWCNT nanocomposite. TEM image of (c) Carboxyl-functionalized MoS_2 nanotubes (Inset: high magnification TEM image showing an open end) and (d) MoS_2- P.SWCNT nanocomposite.

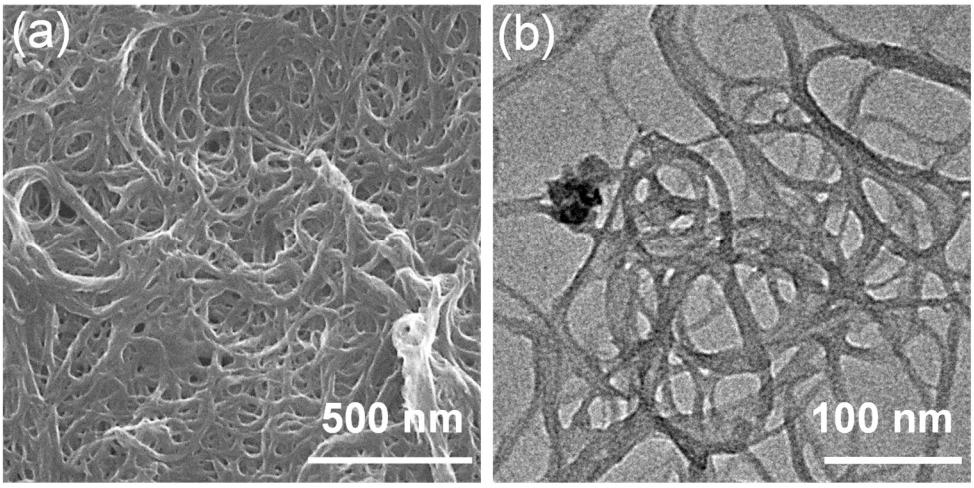

Figure 4. Pristine SWCNT (a) SEM image and (b) TEM image.

the starting SWCNT show micrometer-length bundles as expected (Figure 4a, b). The TEM image of MoS_2−C_6H_4COOH given in Figure 3c shows that the tube morphology is retained even after defect functionalization and the inset high-resolution image reveals these nanotubes have open end structure. Figure 5a, c shows the FESEM and TEM image of starting BCNNT showing bamboo-like tubular structures. Energy-dispersive X-ray spectra (EDS) of a BCNNT show peaks for B, C, and N with atomic percentages of 8.88, 69.91, and 9.22 at. %, respectively (Figure 5b). There are some oxygen elements in the material, perhaps because of oxygen-containing functional groups. Figure 3d and Figure 5d show the TEM images of MoS_2−P.SWCNT and MoS_2−P.BCNNT composites, respectively.

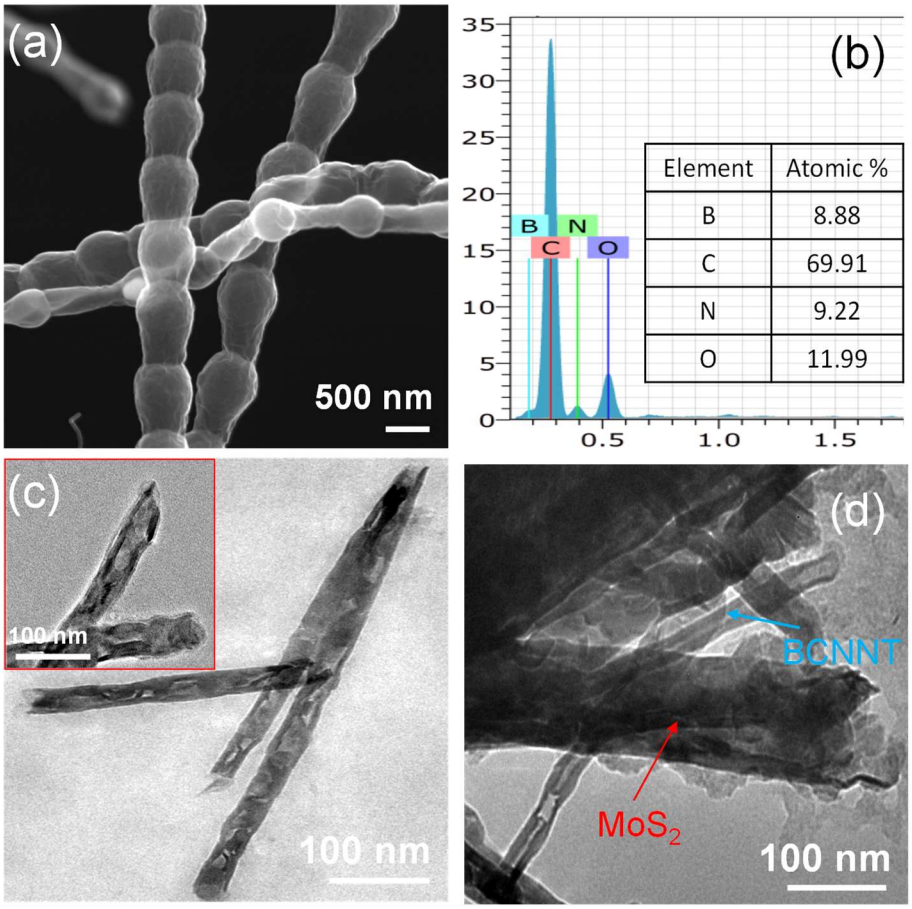

Figure 5. (a) SEM image, (b) EDX, (c) TEM image of pristine BCNNT, and (d) TEM image of MoS_2-P.BCNNT nanocomposite showing MoS_2 and BCN nanotubes.

It is evident from the TEM images that MoS_2 nanotubes are attached to SWCNT/BCNNT networks. The IR spectrum of MoS_2−C_6H_4COOH shows C=C and O−H stretching bands at 1619 and 3129 cm^{-1}, respectively, signifying the surface functionalization of MoS_2 nanotube with MBA moiety (Figure 6). Notably, the S−H stretching band at 2561 cm^{-1} present in the MBA no longer appears in the case of MoS_2−C_6H_4COOH, revealing that MBA is conjugated with nanotubes via defect functionalization.[27]

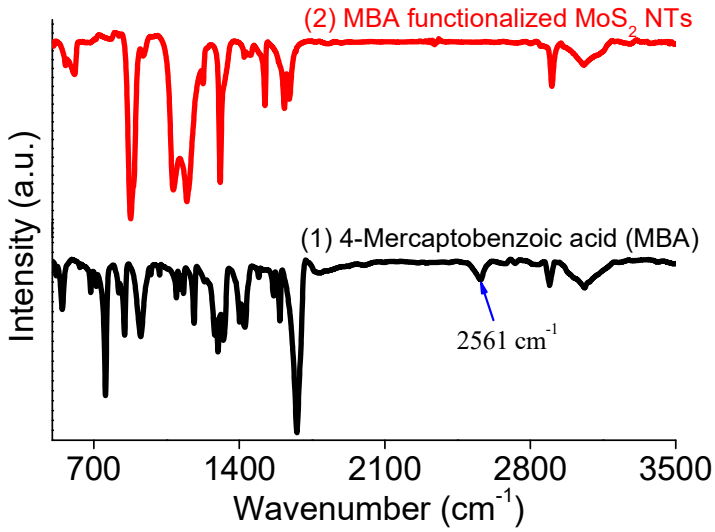

Figure 6. IR spectra of 4-mercaptobenzoic acid (1) and carboxyl-functionalized MoS_2 nanotubes (2).

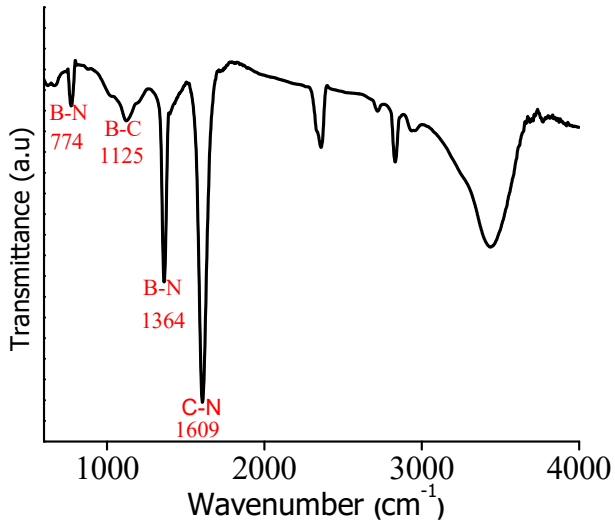

Figure 7. IR spectra of pristine BCNNT.

Meanwhile, IR spectrum of BCNNT exhibit peaks for B−N, B−C, and C−N type bonds at 1364, 1125, and 1609 cm^{-1}, respectively, revealing the presence of BN, C, and BCN networks (Figure 7).[30] Figure 8a show the Raman spectra of MoS_2−P.SWCNT(1:3, 1:1, 3:1, 5:1) composites along with those of MoS_2−C_6H_4COOH and P.SWCNT. The Raman spectrum of MoS_2−C_6H_4COOH exhibits E^1_{2g} and A_{1g} signals from the trigonal polytype MoS_2 at 381 and 406 cm^{-1}, respectively, signifying functionalized nanotubes to be in the 2H-phase.

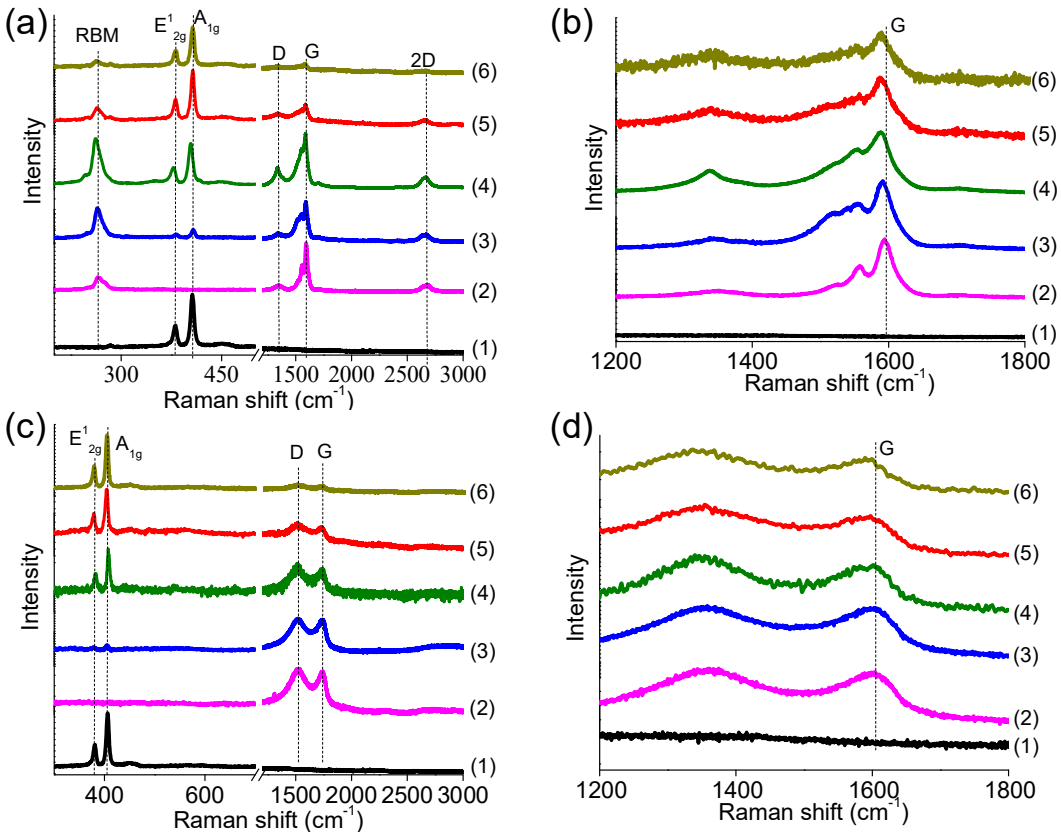

Figure 8. Raman spectra of (a) (1) MoS_2-C_6H_4COOH, (2) P.SWCNT, (3) MoS_2-P.SWCNT (1:3), (4) MoS_2-P.SWCNT (1:1), (5) MoS_2-P.SWCNT (3:1) and (6) MoS_2-P.SWCNT (5:1) nanocomposites, (b) Magnified portion of (a) in the 1200-1800 cm^{-1} range (Composite samples are normalized to the intensity of the SWCNT G band). (c) (1) MoS_2-C_6H_4COOH, (2) P.BCNNT, (3) MoS_2-P.BCNNT (1:3), (4) MoS_2-P.BCNNT (1:1), (5) MoS_2-P.BCNNT (3:1) and (6) MoS_2-P.BCNNT (5:1) nanocomposites, (d) Magnified portion of (c) in the 1200-1800 cm^{-1} range (Composite samples are normalized to the intensity of the BCNNT G band).

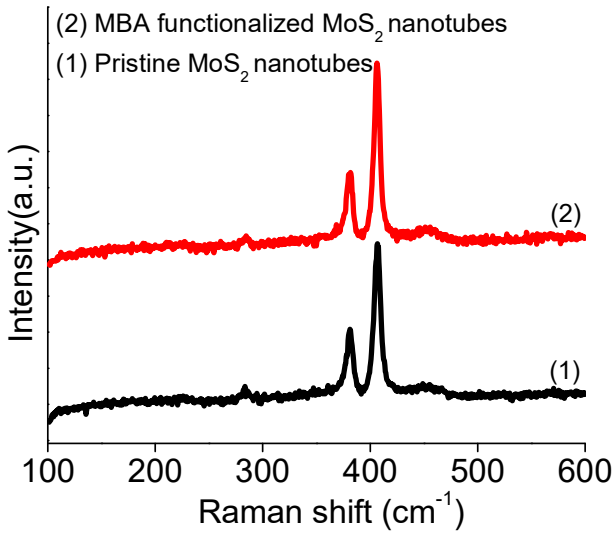

Figure 9. Raman spectra of pristine MoS_2 nanotubes (1) and MBA-functionalized MoS_2 nanotubes (2).

In the case of bare MoS_2 nanotubes, these modes were found at 383 and 408 cm^{-1}, respectively (Figure 9). The Raman spectrum of P.SWCNT exhibits radial breathing mode (RBM) of SWCNT at 266 cm^{-1} along with D and G modes at 1338 and 1589 cm^{-1}, respectively. The Raman bands of both MoS_2 nanotubes and SWCNT appears in the case of MoS_2–P.SWCNT nanocomposites. It is noteworthy that the RBM characteristic of SWCNT is retained in the case of MoS_2–P.SWCNT even after functionalization and electrostatic stacking (Figure 8a). Compared to pristine SWCNT, the G band of MoS_2–P.SWCNT composites are red-shifted, suggesting the possible charge-transfer interaction between the electrostatically stacked hetero-nanotubes (Figure 8).[31,32]

With the rise in MoS_2 nanotube proportion, we observed progressive softening in the G band frequency. Raman spectra of MoS_2–P.BCNNT nanocomposites show characteristic E^1_{2g} and A_{1g} signals of MoS_2 at 381 and 407 cm^{-1}, respectively, along with the D and G modes of

BCNNT (Figure 8c). The G band is slightly red-shifted in MoS_2–P.BCNNT (3:1, 5:1) nanocomposites compared to P.BCNNT, as shown in Figure 8d.

Photocatalytic Hydrogen Generation

Photocatalytic HER activity of MoS_2–P.SWCNT and MoS_2–P.BCNNT composites are examined under visible-light irradiation using eosin Y (EY) dye as a photosensitizer and TEOA as a sacrificial agent. In Figure 10a and Table 3, we present the yield of H_2 evolved by employing MoS_2–P.SWCNT (1:1) nanocomposite and the corresponding physical mixture as well as bare MoS_2 and SWCNT.

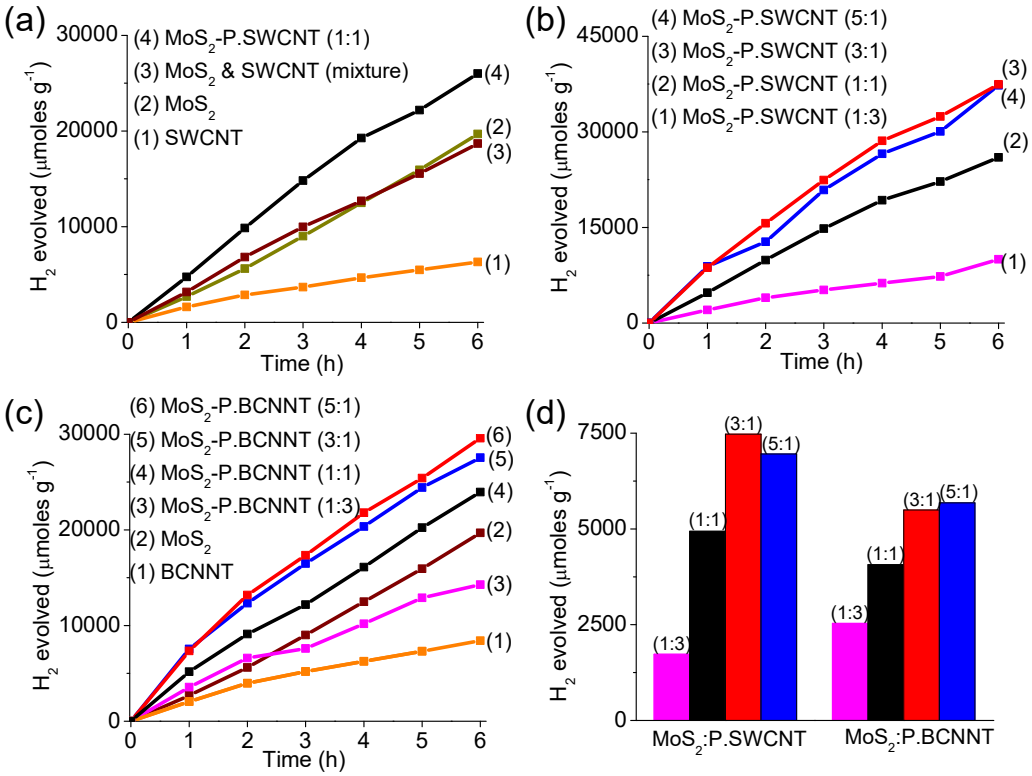

Figure 10. Photocatalytic HER data. (a) (1) SWCNT, (2) MoS_2 nanotubes, (3) MoS_2 & SWCNT (mixture) and (4) MoS_2-P.SWCNT (1:1) nanocomposites. (b) (1) MoS_2-P.SWCNT (1:3), (2) MoS_2-P.SWCNT (1:1), (3) MoS_2-P.SWCNT (3:1) and (4) MoS_2-P.SWCNT (5:1) nanocomposites. (c) (1) BCNNT, (2) MoS_2 nanotubes, (3) MoS_2-P.BCNNT (1:3), (4) MoS_2-P.BCNNT (1:1), (5) MoS_2-P.BCNNT (3:1) and (6) MoS_2-P.BCNNT (5:1) nanocomposites. (d) Bar diagram presenting the comparison of the photocatalytic H_2 evolution of MoS_2-P.SWCNT and MoS_2-P.BCNNT composites with rise in SWCNT/BCNNT content.

Table 3. Photocatalytic HER activity of MoS_2-P.SWCNT and MoS_2-P.BCNNT nanocomposites.

Catalyst	H_2 evolved (μmoles g^{-1} h^{-1})	Catalyst	H_2 evolved (μmoles g^{-1} h^{-1})
MoS_2	3187	MoS_2 and SWCNT	3112
SWCNT	1096	BCNNT	1463
MoS_2-P.SWCNT (1:3)	1731	MoS_2-P.BCNNT (1:3)	2536
MoS_2-P. SWCNT (1:1)	4939	MoS_2-P.BCNNT (1:1)	4064
MoS_2-P.SWCNT (3:1)	7475	MoS_2-P.BCNNT (3:1)	5495
MoS_2-P.SWCNT (5:1)	6957	MoS_2-P.BCNNT (5:1)	5682

MoS_2–P.SWCNT (1:1) composite exhibits H_2 evolution rate of 4939 μmol g^{-1} h^{-1}, whereas the pristine MoS_2 and SWCNT show H_2 yields of 3187 and 1096 μmol g^{-1} h^{-1}, respectively. The composite shows ~1.5 and 5 times higher catalytic activity than the individual MoS_2 and SWCNT, respectively. We have also performed HER studies with the physical mixture of MoS_2 and SWCNT to understand the impact of electrostatic stacking in MoS_2–P.SWCNT composites on the HER activity. The H_2 evolution with the physical mixture (3112 μmol g^{-1} h^{-1}) is much less than that of MoS_2–P.SWCNT (1:1) nanocomposite (4939 μmol g^{-1} h^{-1}). The superior performance of the nanocomposites arises from the increased interfacial area as well as better charge separation efficiency between the heteronanotubes due to tube-by-tube electrostatic stacking, which enhances the charge-transfer interaction between MoS_2 and SWCNT. To further examine the optimal ratio of MoS_2 and SWCNT in nanocomposites, we have compared the activity of electrostatically stacked hetero-nanotubes with varying MoS_2 and SWCNT ratio of (1:3), (1:1), (3:1), and (5:1). The MoS_2–P.SWCNT (3:1) and (5:1) ratios show higher activity compared to (1:3, 1:1) compositions, with the 3:1 composition displaying the highest HER activity of 7475 μmol g^{-1} h^{-1} (Figure 10b). A similar trend in enhancement in

H_2 evolution rate with increase in MoS_2 nanotube proportion is observed with MoS_2–P.BCNNT composites as well. The catalytic activities of 3:1 and 5:1 MoS_2–P.BCNNT nano composites are superior compared to (1:3) and 1:1) ratios with the 5:1 nanocomposite showing the highest H_2 yield of 5682 μmol g^{-1} h^{-1} (Figure 10c and Table 3). The above results signify that the electrostatic stacking of 1D MoS_2 with SWCNT and BCNNT substantially improves the H_2 evolution rate of the individual components, wherein the H_2 yield rises with MoS_2 ratio because of the increased number of active sites. The 1D nature of MoS_2 and negative surface charge helps them effectively intercalate between positively charged SWCNT/BCNNT (Figure 2), leading to the high interfacial area and charge-transfer interactions between the heteronanotubes, thereby enhancing HER activity. But the increment in HER activity in the case of MoS_2–P.BCNNT, in relation to bare MoS_2 nanotubes, is somewhat lower than that of MoS_2–P.SWCNT (Figure 10d). The sponge-like porous carbon networks of SWCNT (Figure 4) probably offer more interfacial area and better charge separation efficiency, thereby shows higher activity.[24,33]

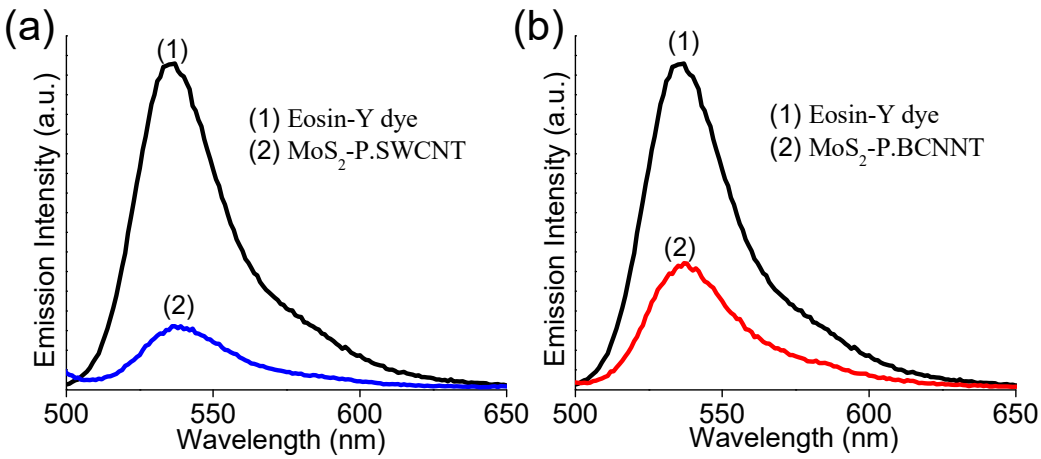

Figure 11. Emission spectra of eosin Y (1 x 10^{-7} M) in the presence of (a) MoS_2-P.SWCNT and (b) MoS_2-P.BCNNT nanocomposites.

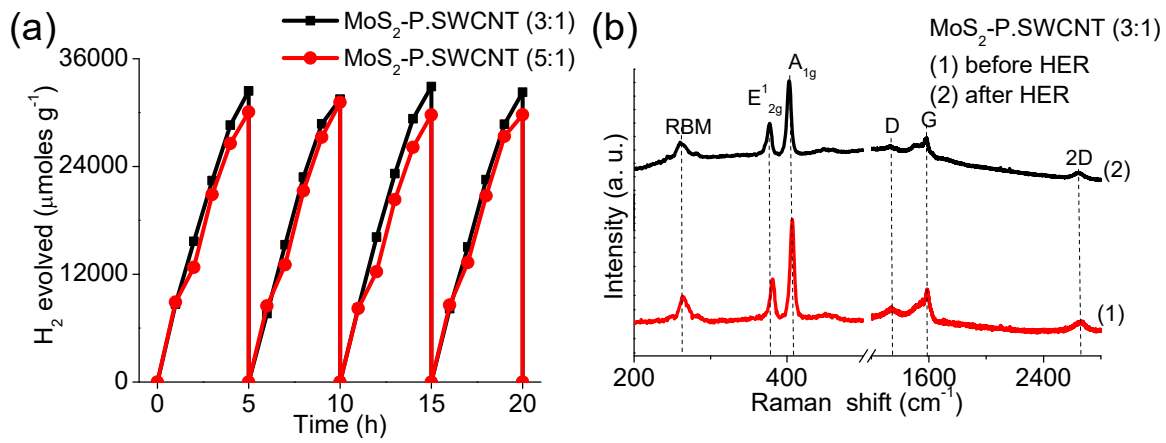

Figure 12. (a) Cyclic stability curves of MoS_2-P.SWCNT (3:1, 5:1) composites. (b) Raman spectra of MoS_2-P.SWCNT (3:1) nanocomposite, before (1) and after (2) photocatalytic HER.

The mechanism of visible-light-driven HER activity of MoS_2-based nanostructures in the presence of EY is well documented in the literature.[34,35] Primarily, EY under visible light is photoexcited to EY*, which later undergoes a series of changes. Spontaneous electron-transfer from sacrificial agent (TEOA) to restructured EY* gives rise to greatly reduced EY^- species. The excited electron of EY^- could eventually be utilized for water reduction by MoS_2. The photoluminescence (PL) spectra of MoS_2–P.SWCNT and MoS_2–P.BCNNT are recorded in the presence of a photosensitizer EY to understand the photoexcited electron-transfer between EY and nanocomposites. As shown in Figure 11, the EY emission band (at 535 nm) is significantly quenched in the presence of MoS_2–P.SWCNT and MoS_2–P.BCNNT nanocomposites, implying effective electron-transfer from EY to MoS_2–P.SWCNT as well as MoS_2–P.BCNNT, which can ultimately utilized for H^+ reduction. The cyclic stability curve of MoS_2–P.SWCNT (20 h, 4 cycles) shown in Figure 12a specifies that the H_2 evolution to be robust. The Raman spectrum of MoS_2–P.SWCNT (3:1) after HER experiment is given in Figure 12b reveals that photocatalyst to be stable. In Table 4, we have compared the H_2 evolution rate of

MoS_2–P.SWCNT (3:1) nanocomposites with some of the 1D nanotubes (g-C_3N_4 nanotube, TiO_2 nanotube, titanate nanotube) and related nanohybrids stated in the literature.

Table 4. Comparison of electrocatalytic HER performance of MoS_2-P.SWCNT and MoS_2-P.BCNNT composites with few of the literature reports.

Catalyst	Reaction Conditions	Activity (μmoles g^{-1} h^{-1})
g-C_3N_4 nanotubes[36]	300 W xenon lamp, TEOA	189
Pt/TiO_2 nanoparticle-CNT[37]	300 W xenon lamp, Methanol	242
Bimetallic Ag–Cu/C_3N_4 nanotubes[38]	300 W xenon lamp, TEA	246
TiO_2 nanoparticle-CNT[39]	300 W xenon lamp, TEOA	377
Au nanoparticle-TiO_2 nanotube[40]	100 mW cm^{-2}, Methanol	482
Ni_2P nanoparticle-CNT[41]	300W xenon lamp, TEOA	627
MoS_2 nanoflake-g-C_3N_4 nanotube[36]	300W xenon lamp, TEOA	1124
Titanate nanotube[42]	250 W xenon lamp, Methanol	2000
Pt/oxygen-doped g-C_3N_4 nanotubes[43]	500W mercury lamp, TEOA	3692
CdS/MoS_2 nanosheets-DWNT[44]	500W UV-vis lamp, Lactic acid	5728
Pt/TiO_2 nanoparticle-fSWCNT[45]	40 mW cm^{-2}, Methanol	7100
EY/Cu_3P-CNT[46]	350 W xenon lamp, TEOA	7350
EY/MoS_2-P.SWCNT (3:1)[a]	400W xenon lamp, TEOA	7475

CNT-Carbon nanotube; DWNT- Double walled carbon nanotubes;
fSWCNT-functionalized single-walled carbon nanotubes;
EY- Eosin Y dye; [a] Nanotube composites reported in the present work.

Electrocatalytic Hydrogen Generation

Encouraged by the superior photocatalytic activity of nanocomposites, we have examined their electrocatalytic H_2 evolution in 0.5M H_2SO_4 using a conventional three-electrode setup. The linear sweep voltammogram (LSV) curves of MoS_2–P.SWCNT(1:1) along with those of bare MoS_2 nanotubes, SWCNT, and MoS_2 and SWCNT (mixture) are shown in Figure 13; the LSV curve of commercial platinum catalyst is also recorded. The onset potential value for MoS_2–P.SWCNT (1:1) (190 mV) is lower compared to bare MoS_2 (310 mV) and SWCNT

(490mV). Further, the physical mixture of MoS_2 and SWCNT does not exhibit any notable shift in the onset potential relative to MoS_2, whereas MoS_2–P.SWCNT (1:1) exhibits a 120 mV shift in the positive direction, suggesting the superior activity of the nanocomposite. Moreover, MoS_2–P.SWCNT (3:1, 5:1) compositions, with high MoS_2 content show somewhat lower onset potential values, 80 and 70 mV, respectively, compared to (1:3, 1:1) ratios (Figure 13b). A similar trend is observed in photocatalytic H_2 evolution as well. To gain further insights into the kinetics of HER, we have explored Tafel slopes of electrostatically stacked hetero-nanotubes. The Tafel slope values for MoS_2–P.SWCNT (3:1, 1:1, 3:1, 5:1), pristine MoS_2, SWCNT, and a physical mixture of MoS_2 and SWCNT are 162, 88, 100, 95, 137, 300, and 260 mV dec^{-1}, respectively (Figures 13c, 14a).

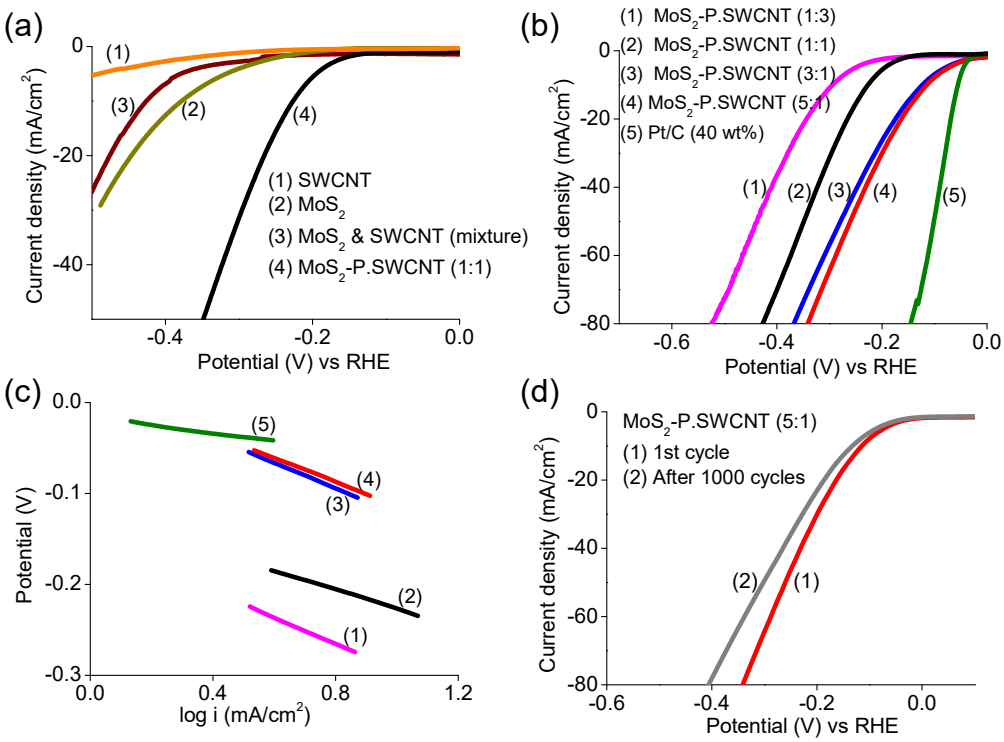

Figure 13. Electrocatalytic HER data. (a) LSV curves of (1) SWCNT, (2) MoS_2 nanotubes, (3) MoS_2 & SWCNT (mixture) and (4) MoS_2-P.SWCNT (1:1) nanocomposites. (b) LSV and (c) Tafel plots of (1) MoS_2-P.SWCNT (3:1), (2) MoS_2-P.SWCNT (1:1), (3) MoS_2-P.SWCNT (3:1), (4) MoS_2-P.SWCNT (5:1) and (5) Pt/C catalysts. (d) LSV curves showing the stability of MoS_2-P.SWCNT (5:1) after1000 cycles.

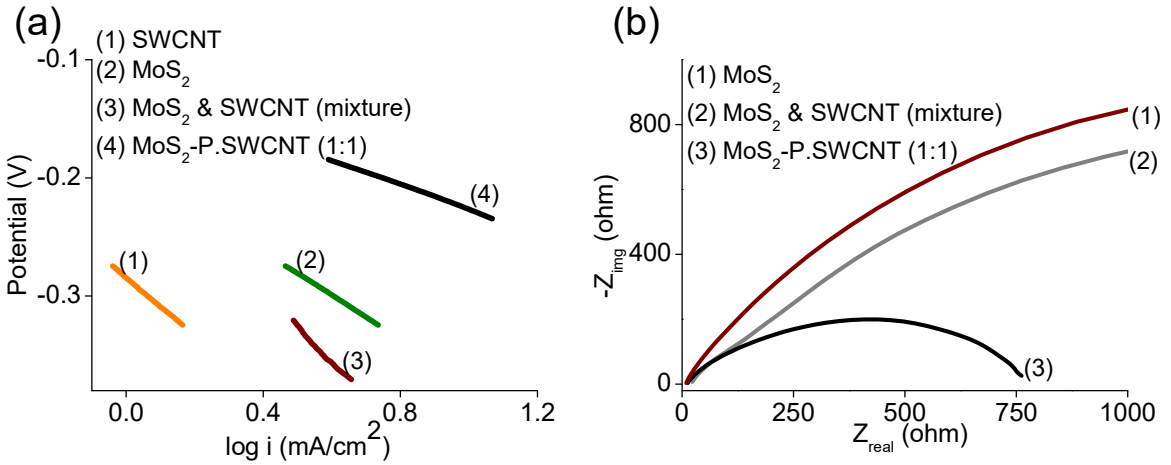

Figure 14. (a) Tafel plots of pristine SWCNT (1), pristine MoS_2 nanotubes (2), physical mixture of MoS_2 & SWCNT (3) and 1:1 MoS_2-P.SWCNT composites (4). (b) Nyquist plot of pristine MoS_2 nanotubes (1), MoS_2 & P.SWCNT (mixture) (2), 1:1 MoS_2-P.SWCNT composites (3).

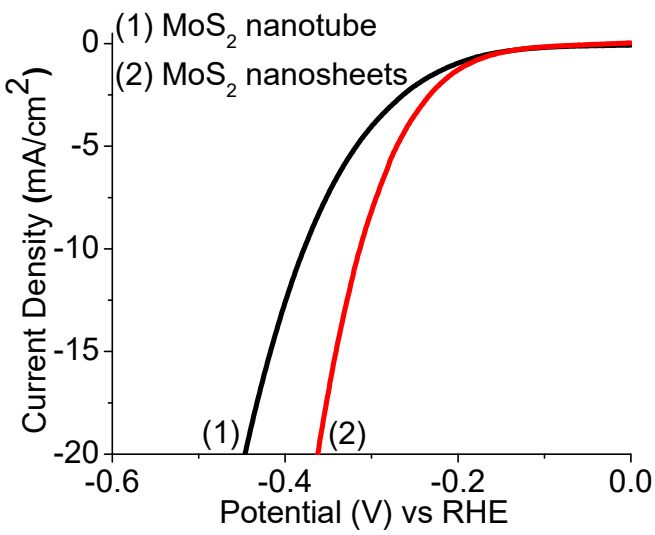

Figure 15. Comparison of LSV curves of (1) MoS_2 nanotube and (2) MoS_2 few layer nanosheets.

Table 5. Comparison of electrocatalytic HER performance of MoS_2-P.SWCNT and MoS_2-P.BCNNT composites with few of the literature reports.

Catalyst	Onset potential (mV vs. RHE)	Tafel slope (mV dec^{-1})
MoS_x/N-doped CNT[11]	75	40
MoS_2/N-MWCNT[47]	90	40
MoS_2/O–MWCNT[47]	100	55
Strongly coupled MoS_2-CNT[10]	100	-
MWMoS_2@MWCNT[48]	150	109
H-MoS_2NS/MWCNT-10[49]	174	83
MoS_2 nanotubes @rGO[50]	180	69
MoS_2/CNT[33]	191	93
Ni-MoS_2 nanoparticle[51]	200	47
MoS_2 nanoparticle[51]	270	59
MoS_2 nanosheets[52]	300	-
MoS_2/CNT-90[8]	-	40
MoS_2 nanoparticle[16]	-	41
MoS_2-P.SWCNT (3:1)[a]	80	100
MoS_2-P.SWCNT (5:1)[a]	70	95
MoS_2-P.BCNNT (1:3)[a]	290	158
MoS_2-P.BCNNT (1:1)[a]	240	202
MoS_2-P.BCNNT (3:1)[a]	260	156
MoS_2-P.BCNNT (5:1)[a]	220	121
MoS_2[a]	310	137
SWCNT[a]	490	300
BCNNT[a]	590	256
MoS_2 & SWCNT (mixture)[a]	380	260
MoS_2-P.SWCNT (1:3)[a]	250	162
MoS_2-P.SWCNT (1:1)[a]	190	88
Pt/C[a]	45	37

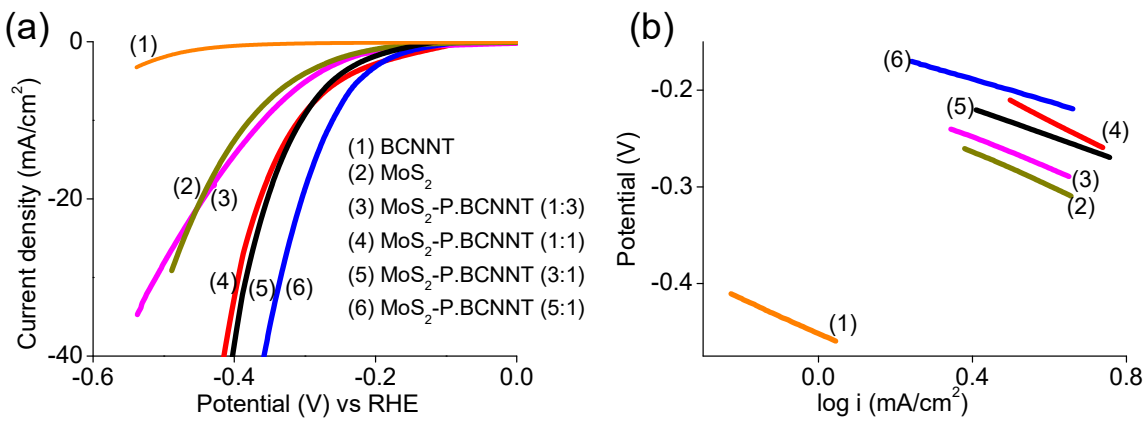

Figure 16. Electrocatalytic HER data. (a) LSV curves of and (b) Tafel plots of (1) BCNNT, (2) MoS_2 nanotubes, (3) MoS_2-P.BCNNT (1:3), (4) MoS_2-P.BCNNT (1:1), (5) MoS_2-P.BCNNT (3:1) and (6) MoS_2-P.SWCNT (5:1) nanocomposites.

The lowest Tafel slope value for nanocomposite signifies the proficient electron-transfer from electrostatically stacked nanotubes to the active sites. We have shown comparison between MoS_2 nanotube and MoS_2 nanosheets (Figure 15). Electrochemical impedance spectroscopy (EIS) studies also suggest the MoS_2−P.SWCNT nanocomposite exhibits low charge-transfer resistance compared to the physical mixture or MoS_2 alone (Figure 14b). Further, the electrochemical stability of MoS_2−SWCNT (5:1) is evaluated using LSV in the potential range 0 to −0.6 V, where only a 15 mV change in the onset potential is observed even after 1000 cycles (Figure 13d). This signifies the high electrochemical stability of the electrostatically stacked heteronanotubes. We have also studied the electrocatalytic H_2 evolution performance of MoS_2−P.BCNNT composites of (1:3), (1:1), (3:1), and (5:1) compositions. The onset potential and Tafel slope values of MoS_2−P.BCNNT composites are not as good as those of MoS_2−P.SWCNT (Figure 16a, b). Unlike MoS_2−P.SWCNT (3:1), MoS_2−P.BCNNT (3:1) needs an additional overpotential of 175 mV to reach a current density of 20 $mAcm^{-2}$. It is noteworthy that electrocatalytic HER activity of MoS_2−P.SWCNT (5:1) is

comparable/superior to those reported for most of the 0D/1D/2D MoS_2−CNT composites (Table 5).

5. Conclusions

In conclusion, we were successful in preparing nanocomposites of MoS_2 nanotube with polymer-functionalized SWCNT and BCNNT by a solution process. The study shows the beneficial effect of electrostatic restacking of various 1D nanotubes in HER activity. The MoS_2−P.SWCNT and MoS_2−P.BCNNT hetero-nanotubes exhibit high photocatalytic and electrocatalytic H_2 evolution rates compared to the pristine MoS_2 nanotube, and the yield increases with the MoS_2 nanotube ratio in the nanocomposite. Photocatalytic H_2 evolution of MoS_2−P.SWCNT (3:1) nanocomposite is significant with an H_2 evolution of 7475 μmol g^{-1} h^{-1}. The superior activity of the nanocomposites is ascribed to the ordered stacking of the hetero-nanotubes, enhancing charge-transfer interactions as well as the interfacial area between MoS_2 nanotubes and SWCNT.

6. References

[1] P. Zhao, M. Ni, Y. Xu, C. Wang, C. Chen, X. Zhang, C. Li, Y. Xie, J. Fei, *Sensors Actuators, B Chem.* **2019**, *299*, 126997.

[2] G. Deokar, P. Vancsó, R. Arenal, F. Ravaux, J. Casanova-Cháfer, E. Llobet, A. Makarova, D. Vyalikh, C. Struzzi, P. Lambin, M. Jouiad, J. F. Colomer, *Adv. Mater. Interfaces* **2017**, *4*, 1.

[3] W. Y. Chen, A. Yermembetova, B. M. Washer, X. Jiang, S. N. Shuvo, D. Peroulis, A. Wei, L. A. Stanciu, *ACS Sensors* **2020**, *5*, 1699.

[4] J. Ren, R. P. Ren, Y. K. Lv, *Chem. Eng. J.* **2018**, *353*, 419.

[5] Y. C. Jeong, J. H. Kim, S. H. Kwon, J. Y. Oh, J. Park, Y. Jung, S. G. Lee, S. J. Yang, C. R. Park, *J. Mater. Chem. A* **2017**, *5*, 23909.

[6] H. Yoo, A. P. Tiwari, J. Lee, D. Kim, J. H. Park, H. Lee, *Nanoscale* **2015**, *7*, 3404.

[7] T. Stephenson, Z. Li, B. Olsen, D. Mitlin, *Energy Environ. Sci.* **2014**, *7*, 209.

[8] H. Yuan, J. Li, C. Yuan, Z. He, *ChemElectroChem* **2014**, *1*, 1828.

[9] J. Cao, J. Zhou, Y. Zhang, X. Liu, *Sci. Rep.* **2017**, *7*, 1.

[10] H. Huang, W. Huang, Z. Yang, J. Huang, J. Lin, W. Liu, Y. Liu, *J. Mater. Chem. A* **2017**, *5*, 1558.

[11] D. J. Li, U. N. Maiti, J. Lim, D. S. Choi, W. J. Lee, Y. Oh, G. Y. Lee, S. O. Kim, *Nano Lett.* **2014**, *14*, 1228.

[12] R. Xiang, T. Inoue, Y. Zheng, A. Kumamoto, Y. Qian, Y. Sato, M. Liu, D. Tang, D. Gokhale, J. Guo, K. Hisama, S. Yotsumoto, T. Ogamoto, H. Arai, Y. Kobayashi, H. Zhang, B. Hou, A. Anisimov, M. Maruyama, Y. Miyata, S. Okada, S. Chiashi, Y. Li, J. Kong, E. I. Kauppinen, Y. Ikuhara, K. Suenaga, S. Maruyama, *Science* **2020**, *367*, 537.

[13] C. Ataca, H. Şahin, E. Aktuörk, S. Ciraci, *J. Phys. Chem. C* **2011**, *115*, 3934.

[14] C. N. R. Rao, K. Gopalakrishnan, U. Maitra, *ACS Appl. Mater. Interfaces* **2015**, *7*, 7809.

[15] M. Khan, A. Bin Yousaf, M. Chen, C. Wei, X. Wu, N. Huang, Z. Qi, L. Li, *Nano Res.* **2016**, *9*, 837.

[16] Y. Li, H. Wang, L. Xie, Y. Liang, G. Hong, H. Dai, *J. Am. Chem. Soc.* **2011**, *133*, 7296.

[17] K. Pramoda, U. Gupta, I. Ahmad, R. Kumar, C. N. R. Rao, *J. Mater. Chem. A* **2016**, *4*, 8989.

[18] K. Pramoda, U. Gupta, M. Chhetri, A. Bandyopadhyay, S. K. Pati, C. N. R. Rao, *ACS Appl. Mater. Interfaces* **2017**, *9*, 10664.

[19] K. Pramoda, M. M. Ayyub, N. K. Singh, M. Chhetri, U. Gupta, A. Soni, C. N. R. Rao, *J. Phys. Chem. C* **2018**, *122*, 13376.

[20] K. Pramoda, S. Servottam, M. Kaur, C. N. R. Rao, *ACS Appl. Nano Mater.* **2020**, *3*, 1792.

[21] P. Chithaiah, S. Ghosh, A. Idelevich, L. Rovinsky, T. Livneh, A. Zak, *ACS Nano* **2020**, *14*, 3004.

[22] R. Voggu, K. V. Rao, S. J. George, C. N. R. Rao, *J. Am. Chem. Soc.* **2010**, *132*, 5560.

[23] L. Liu, W. E. Stanchina, G. Li, *Appl. Phys. Lett.* **2009**, *94*, 1.

[24] C. Liu, F. Liu, H. Li, J. Chen, J. Fei, Z. Yu, Z. Yuan, C. Wang, H. Zheng, Z. Liu, M. Xu, G. Henkelman, L. Wei, Y. Chen, *arXiv e-prints* **2020**, arXiv:2009.14396.

[25] P. Xiong, R. Ma, N. Sakai, L. Nurdiwijayanto, T. Sasaki, *ACS Energy Lett.* **2018**, *3*, 997.

[26] P. Xiong, R. Ma, N. Sakai, T. Sasaki, *ACS Nano* **2018**, *12*, 1768.

[27] S. Karunakaran, S. Pandit, B. Basu, M. De, *J. Am. Chem. Soc.* **2018**, *140*, 12634.

[28] K. Pramoda, R. Kumar, C. N. R. Rao, *Chem. - An Asian J.* **2015**, *10*, 2147.

[29] P. Chithaiah, K. Pramoda, G. U. Kulkarni, C. N. R. Rao, *Eur. J. Inorg. Chem.* **2020**, *2020*, 1230.

[30] G. ZHANG, Z. LIU, L. ZHANG, L. JING, K. SHI, *J. Chem. Sci.* **2013**, *125*, 1169.

[31] S. Singh, S. Sharma, R. C. Singh, S. Sharma, *Appl. Surf. Sci.* **2020**, *532*, 147373.

[32] V. O. Koroteev, L. G. Bulusheva, I. P. Asanov, E. V. Shlyakhova, D. V. Vyalikh, A. V. Okotrub, *J. Phys. Chem. C* **2011**, *115*, 21199.

[33] X. Zhang, F. Zhou, S. Zhang, Y. Liang, R. Wang, *Adv. Sci.* **2019**, *6*, 1900090.

[34] U. Maitra, U. Gupta, M. De, R. Datta, A. Govindaraj, C. N. R. Rao, *Angew. Chemie - Int. Ed.* **2013**, *52*, 13057.

[35] U. Gupta, B. S. Naidu, U. Maitra, A. Singh, S. N. Shirodkar, U. V. Waghmare, C. N. R. Rao, *APL Mater.* **2014**, *2*, 092802.

[36] J. Sun, S. Yang, Z. Liang, X. Liu, P. Qiu, H. Cui, J. Tian, *J. Colloid Interface Sci.* **2020**, *567*, 300.

[37] Y. Zhang, Z. Xing, J. Zou, Z. Li, X. Wu, L. Shen, Q. Zhu, S. Yang, W. Zhou, *RSC Adv.* **2017**, *7*, 453.

[38] Y. Zhu, A. Marianov, H. Xu, C. Lang, Y. Jiang, *ACS Appl. Mater. Interfaces* **2018**, *10*, 9468.

[39] K. Dai, X. Zhang, K. Fan, P. Zeng, T. Peng, *J. Nanomater.* **2014**, *2014*, 694073.

[40] X. Yang, L. Wu, L. Du, X. Li, *Catal. Letters* **2015**, *145*, 1771.

[41] Y. Jiao, Y. Li, J. Wang, Z. He, Z. Li, *Appl. Surf. Sci.* **2020**, *534*, 147603.

[42] H.-Y. Chen, S.-L. Lo, H.-L. Chang, *Nano* **2020**, *15*, 2050129.

[43] Y. Zhang, Z. Chen, J. Li, Z. Lu, X. Wang, *J. Energy Chem.* **2021**, *54*, 36.

[44] M. Meng-Jung Li, P. Mills, S. M. Fairclough, A. Robertson, Y. K. Peng, J. Warner, C. Nie, E. Flahaut, S. C. E. Edman Tsang, *Chem. Commun.* **2016**, *52*, 13596.

[45] F. H. Abdulrazzak, F. H. Hussein, A. F. Alkaim, I. Ivanova, A. V. Emeline, D. W. Bahnemann, *Photochem. Photobiol. Sci.* **2016**, *15*, 1347.

[46] R. Shen, J. Xie, Y. Ding, S. Y. Liu, A. Adamski, X. Chen, X. Li, *ACS Sustain. Chem. Eng.* **2019**, *7*, 3243.

[47] X. Dai, K. Du, Z. Li, H. Sun, Y. Yang, W. Zhang, X. Zhang, *Int. J. Hydrogen Energy* **2015**, *40*, 8877.

[48] A. B. Laursen, S. Kegnæs, S. Dahl, I. Chorkendorff, *Energy Environ. Sci.* **2012**, *5*, 5577.

[49] Y. Li, X. Yin, X. Huang, X. Liu, W. Wu, *Int. J. Hydrogen Energy* **2020**, *45*, 16489.

[50] L. Song, M. Zhao, X. Li, Z. Zhang, L. Qu, *RSC Adv.* **2016**, *6*, 70740.

[51] D. Wang, X. Zhang, Y. Shen, Z. Wu, *RSC Adv.* **2016**, *6*, 16656.

[52] D. C. Binwal, M. Kaur, K. Pramoda, C. N. R. Rao, *Bull. Mater. Sci.* **2020**, *43*, 313.

Part IV

Nanocomposites of MoS_2 Nanoparticles with Carboxyl-Functionalized Carbon Nanotubes and Borocarbonitrides Nanosheets, and Their Electrocatalytic HER Activity

Chapter IV

Nanocomposites of MoS_2 Nanoparticles with Carboxyl-Functionalized Carbon Nanotubes and Borocarbonitrides Nanosheets, and Their Electrocatalytic HER Activity

Summary*

We report a facile method to generate MoS_2/single-walled carbon nanotubes (SWCNT) and MoS_2/borocarbonitride (BC_6N) composites by mixing MoS_2 nanoparticle dispersion with different proportions of carboxyl-functionalized SWCNT and BCN in water. The MoS_2/SWCNT and MoS_2/BCN composites show higher electrocatalytic H_2 evolution performance compared to the individual constituents, the activity increasing with the proportion of MoS_2. Among the prepared catalysts, MoS_2-SWCNT with a 3:1 ratio of MoS_2 and SWCNT exhibits highly positive onset potential (-113 mV vs RHE) and a small Tafel slope (59 mV dec^{-1}) as well as remarkable stability in acid electrolyte. The combination of MoS_2 nanoparticles with SWCNT or BCN appears to be a valuable finding with applications in catalysis reactions.

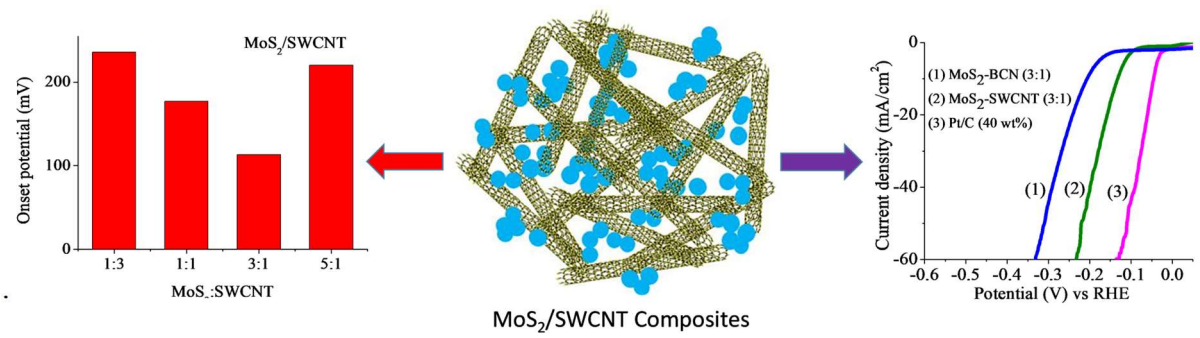

* A Paper based on this work has been submitted to *Mater. Res. Bull.* 2021.

1. Introduction

Since the revelation of remarkable properties of graphene, other 2D transition metal dichalcogenides (TMDCs) such as MoS_2, $MoSe_2$ and WTe_2 have been widely investigated due to their outstanding properties and potential applications from electronics to catalysis.[1–4] Of the TMDCs, MoS_2 has been recognized as an efficient non-noble catalyst for electrocatalytic hydrogen generation from water due to the presence of active sulfur edges.[5–8] The limited surface area, poor intrinsic electronic conductivity, and other stability issues impeded the performance of MoS_2 as an electrocatalyst or electrode material.[9,10] To further enhance the hydrogen evolution reactivity (HER) of MoS_2, several approaches have focused on engineering the MoS_2 nanostructures with better exposure of edge sites. Many nanostructured MoS_2-based catalysts such as quantum dots,[11] flower-like structure,[12] nanoribbons,[13] vertically aligned layers,[14] defect-rich MoS_2 nanosheets[15] and porous 3D network[16] have been prepared to realize higher HER activity compared to bulk MoS_2. There have also been some efforts in increasing electronic conductivity. For instance, MoS_2 nanoparticles directly grown on conductive additives such as carbon nanotube (CNT),[17] graphene,[18] and carbon nitride[19] exhibit superior HER activity through reduced charge-transfer resistance properties. Among these, CNT is considered to be a good support material because of its remarkable electronic conductivity, high surface area, and ease with which surface can be chemically modified to anchor active materials. For example, Liu *et al.*[20] have prepared highly porous and extremely conductive MoS_2/SWCNT composites by simply mixing MoS_2 nanosheet dispersion with SWCNT and utilized them as electrode material for sodium-ion batteries. Further, Ahn *et al.*[21] have designed hydrogen evolution reaction (HER) electrodes by stacking negatively charged exfoliated MoS_2 sheets with amine-functionalized multi-walled carbon nanotubes. Although

the coupling of MoS_2 nanostructures with carbon nanotube enhances conductivity, it remains a challenge to prepare MoS_2/carbon nanotube composites by a simpler or scalable approach to study electrocatalytic HER.

Herein, we have prepared MoS_2/SWCNT composites by simply mixing MoS_2 nanoparticle and carboxyl-functionalized SWCNT dispersions and examined their electrocatalytic HER activity. The MoS_2/SWCNT hybrid is an interconnection of MoS_2 nanoparticles and carboxyl-functionalized SWCNT. The underlying nanotube networks act as conductive channels for the electron transfer and avoid agglomeration of the MoS_2 nanoparticles. Furthermore, as motivated by the superior electrocatalytic HER activity of carbon-rich 2D BCN layers, we also combined MoS_2 nanoparticles with BC_6N sheets and studied their hydrogen evolution activity [22]. Both MoS_2/SWCNT and MoS_2/BCN composites show significant improvement in HER activity compared to the pristine MoS_2 nanoparticles. In Table 1, we have listed the range of MoS_2/SWCNT and MoS_2/BCN composites obtained

Table 1: Composites of MoS_2/SWCNT and MoS_2/BCN prepared

Dichalcogenide nanoparticle (wt %)	Carboxyl-functionalized Carbon precursors (wt %)	Product
MoS_2 (1)	SWCNT (3)	MoS_2/SWCNT (1:3)
MoS_2 (1)	SWCNT (1)	MoS_2/SWCNT (1:1)
MoS_2 (3)	SWCNT (1)	MoS_2/SWCNT (3:1)
MoS_2 (5)	SWCNT (1)	MoS_2/SWCNT (5:1)
MoS_2 (1)	BCN (3)	MoS_2/BCN (1:3)
MoS_2 (1)	BCN (1)	MoS_2/BCN (1:1)
MoS_2 (3)	BCN (1)	MoS_2/BCN (3:1)

by utilizing the various reactant proportions. Unlike MoS_2 nanoparticles, 1D-MoS_2 nanotubes mixed with 1D carbon nanotubes or with 2D BCN layers do not show any meaningful HER activity, since the 1D nature of MoS_2 nanotubes prevents them from intercalating between entangled nanotube networks or stacked sheets.

2. Experimental Section

MoS_2 nanoparticles were synthesized by the reaction between molybdenum hexacarbonyl ($Mo(CO)_6$) and sulfur precursors in para-xylene solvent. Initially, sulfur powder (0.23 mmol) was slowly added to para-xylene (10 mL) under a steady stirring in an N_2 atmosphere and heated at 140 °C, till sulfur dissolves completely.[23] The resultant solution cooled to room temperature and molybdenum hexacarbonyl (0.12 mmol) was added to give the S/Mo atomic ratio of 2. The temperature was raised to reflux and maintained at 140 °C for 1.5 h under N_2 atmosphere.[23] The resultant black-brown precipitate was centrifuged and washed several times with acetone, dried in a vacuum at 50 ºC.

Pristine SWCNTs were procured from commercial source Sigma-Aldrich while carbon-rich borocarbonitride, BC_6N, nanosheets were prepared by high-temperature solid-state urea route, as reported earlier.[22,24] Carboxyl-functionalized SWCNT/BCN was prepared by refluxing pristine SWCNT/BCN (50 mg) with conc. HNO_3 (2 mL) and H_2SO_4 (2 mL) solution and then the obtained black product was filtered and washed with a copious amount of water, ethanol.

To prepare MoS_2/SWCNT nanocomposites, MoS_2 nanoparticle dispersion was added dropwise to the carboxy-functionalized SWCNT, stirred and sonicated for 2 h until a

homogeneous mixture is obtained. MoS_2/SWCNT composite was collected by centrifugation for 30 min at 8000 rpm and dried in a vacuum oven. MoS_2/BCN nanocomposites were prepared by adding MoS_2 nanoparticle dispersion to the carboxyl-functionalized BCN nanosheet.

Electrocatalytic hydrogen evolution studies were carried in 0.5 M H_2SO_4 using a conventional three-electrode configuration consisting of a Hg/Hg_2Cl_2 as the reference electrode, a graphite rod as the counter electrode and a glassy carbon after loading the catalyst as the working electrode. Electrocatalyst ink of each sample was obtained by dispersing 1 mg of the composite in a 4:1:0.05 (v/v/v) proportions of water, isopropyl alcohol, and nafion (5 wt %). The working electrode was fabricated by drop-coating 5 μL of the catalyst-ink onto a glassy carbon electrode (3 mm diameter) to obtain a final loading of ~0.140 mg cm^{-2} and allowed to dry overnight under ambient atmosphere.

3. Results and discussion

Schematic representation of the synthetic procedure for MoS_2 nanoparticles and their composite with SWCNT is presented in Scheme 1. The chemical reaction between $Mo(CO)_6$ and sulfur precursors in organic solvent yields water-dispersible MoS_2 nanoparticles. These nanoparticles show a negative zeta potential of –20 mV (Figure 1a) possibly because of electronically rich sulfur atoms at the edges, suggesting their good dispersibility in water (as shown in Scheme 1) is due to the surface charges. Besides, oxygen functionalities are introduced at pristine SWCNT surface by refluxing them with HNO_3/H_2SO_4 mixture. These surface functionalities assist nanotubes to remain dispersible in water over a longer period. The infrared spectrum of acid-treated SWCNT confirmed the presence of surface carboxyl functional groups by showing a peak at 1720 cm^{-1} (Figure 1b).[25]

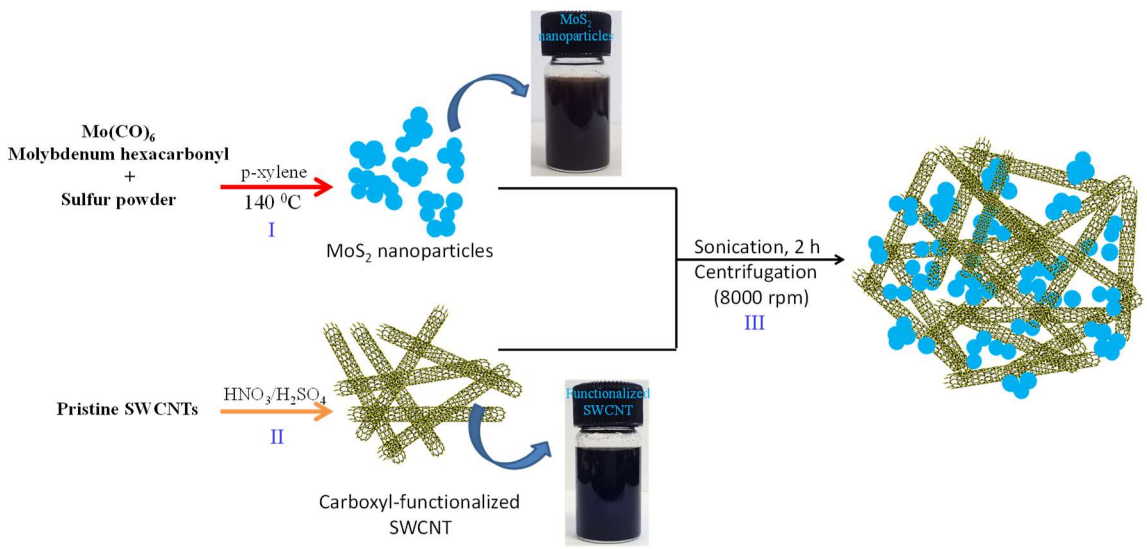

Scheme 1. Schematic of the synthesis MoS_2/SWCNT composites. I) Synthesis of MoS_2 nanoparticles, II) Synthesis of carboxyl-functionalized SWCNT and III) Preparation of MoS_2/SWCNT composites by mixing MoS_2 nanoparticles and carboxyl-functionalized SWCNT dispersions in water with the aid of sonication.

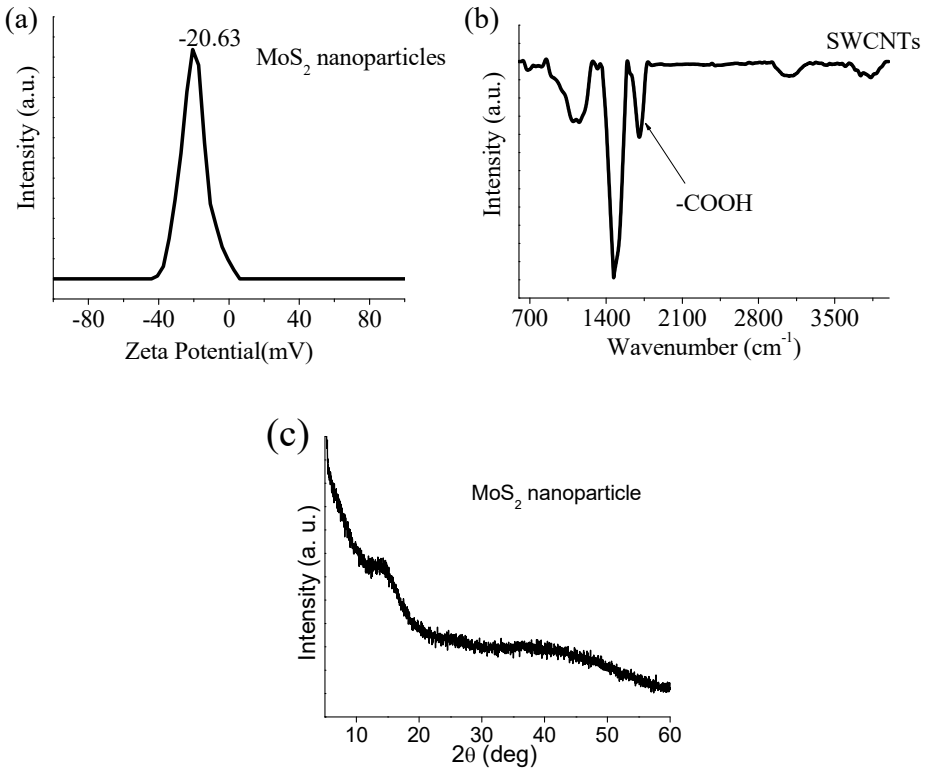

Figure 1. (a) Zeta potential plot of pristine MoS_2 nanoparticles, (b) IR spectra of carboxyl-functionalized SWCNTs and (c) XRD of MoS_2 nanoparticle.

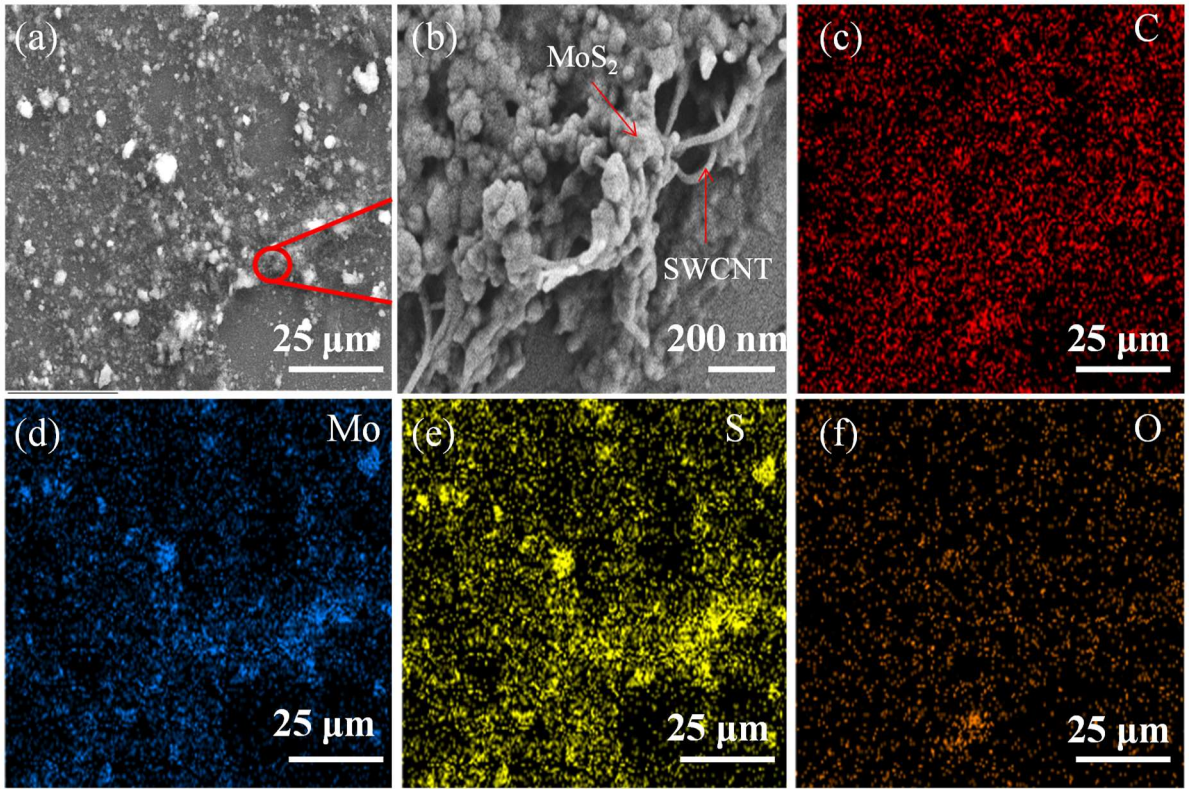

Figure 2. (a, b) SEM and (c-f) Elemental mapping images of the MoS_2/SWCNT composites (Carbon, red; Molybdenum, blue; Sulfur, yellow; Oxygen, brown).

MoS_2/SWCNT hybrids are prepared by adding MoS_2 nanoparticle dispersions to the carboxyl functionalized SWCNT under sonication conditions, and finally centrifuging it. Scanning electron microscope (SEM) and elemental mapping images of MoS_2/SWCNT composite show uniform distribution of molybdenum, sulfur, and carbon elements, specifying MoS_2 and SWCNT homogeneously mixed (Figure 2). During sonication, MoS_2 nanoparticles are not only intercalated between entangled nanotube networks but also couples with SWCNT, as a result, a homogeneous mixture is formed. A transmission electron microscope (TEM) image of bare MoS_2 nanoparticles shows that individual units are agglomerated to form clusters (Figure 3a).

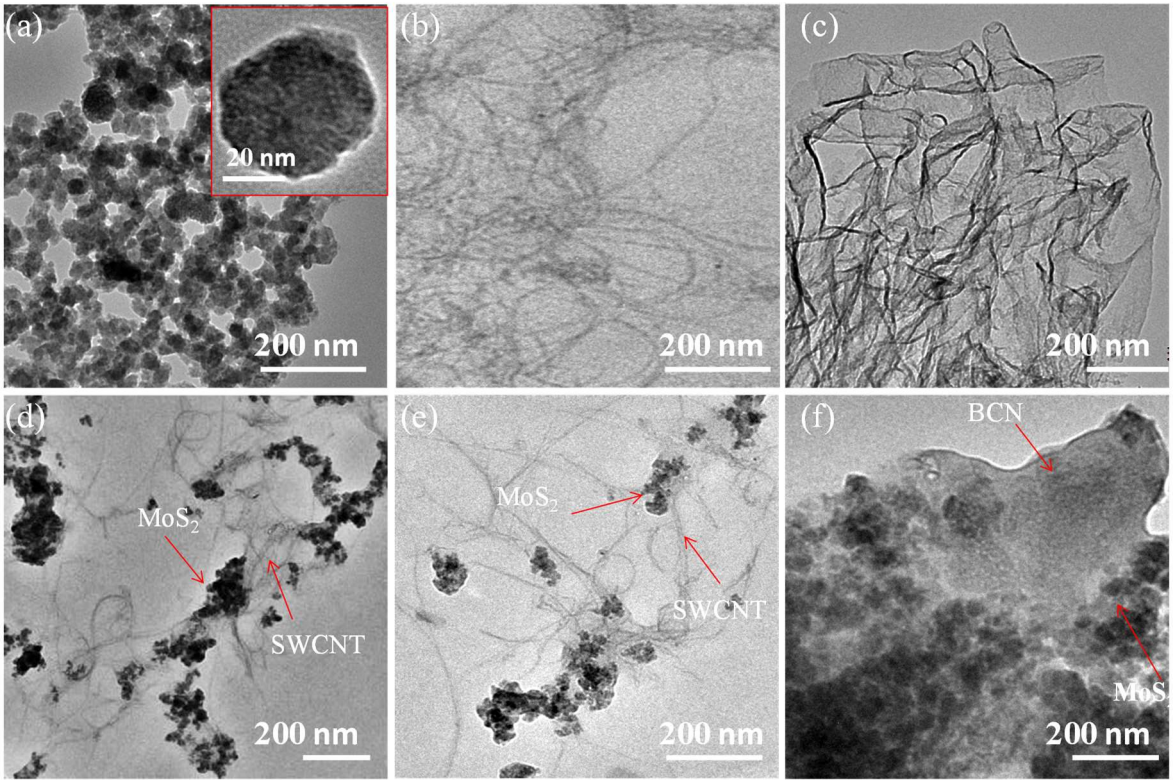

Figure 3. TEM images of pristine (a) MoS_2 nanoparticles (Inset: HRTEM image), (b) SWCNT and (c) BCN nanosheets; TEM images of (d, e) MoS_2/SWCNT composites, (f) MoS_2/BCN composites.

High-resolution TEM revealed MoS_2 nanoparticle is spherical with a grain size of about 40-50 nm (Inset of Figure 3a). The carboxyl-functionalized SWCNT show thin tubular structures of micrometer length (Figure 2b), whereas MoS_2 nanoparticle clusters attached with the SWCNT network can be seen in MoS_2/SWCNT (Figure 3d, e, 2b). Besides, the TEM image of MoS_2/BCN composite revealed the adhesion of MoS_2 nanoparticles to the BCN sheet (Figure 3f) while the starting BC_6N nanosheets show thin-layer features (Figure 3c).

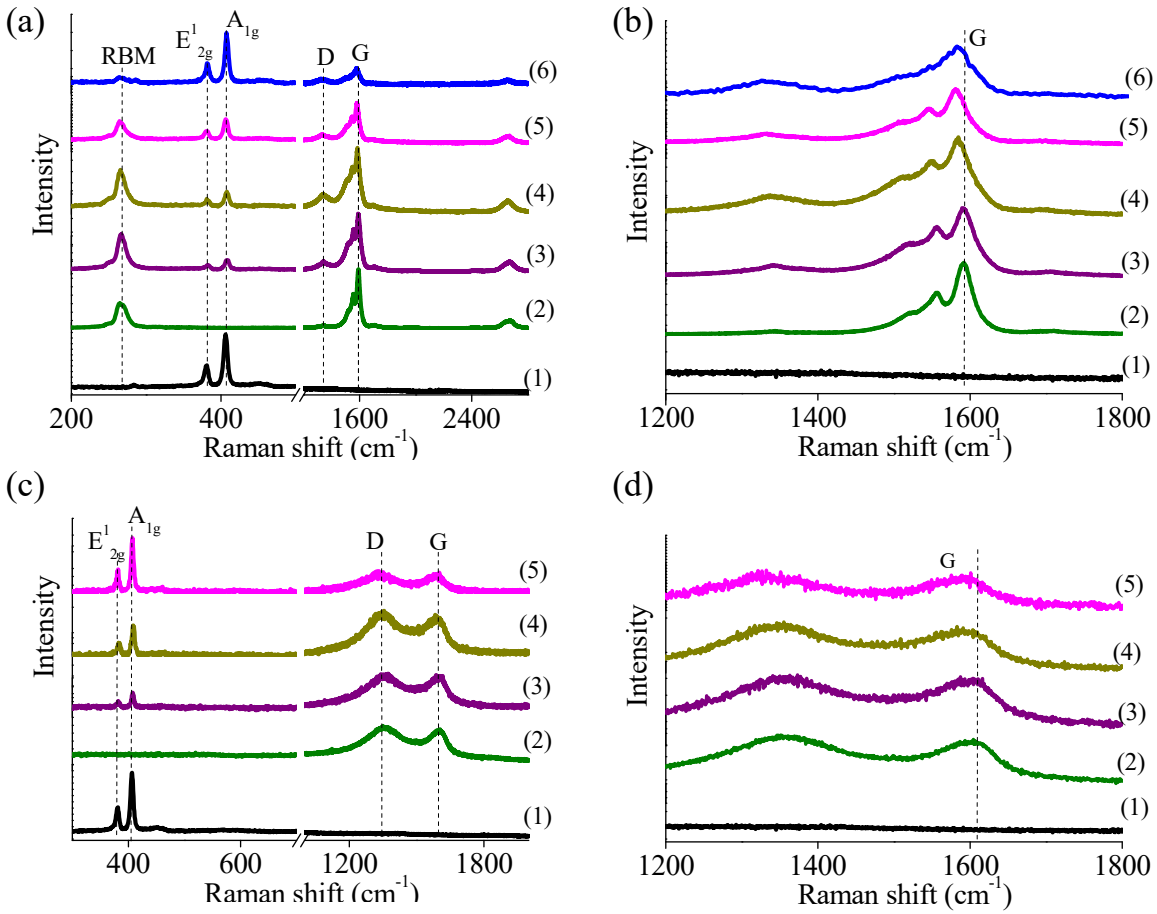

Figure 4. (a) Raman spectra of (1) MoS_2 nanoparticles, (2) SWCNT, (3) MoS_2/SWCNT (1:3), (4) MoS_2/SWCNT (1:1), (5) MoS_2/SWCNT (3:1) and (6) MoS_2/SWCNT (5:1) composites; (b) Magnified portion of (a) in the 1200-1800 cm^{-1} range (composite samples are normalized to the intensity of SWCNT G band); (c) Raman spectra of (1) MoS_2 nanoparticles, (2) BCN, (3) MoS_2/BCN (1:3), (4) MoS_2-BCN (1:1) and (5) MoS_2/BCN (3:1) composites; (d) Magnified portion of (c) in the 1200-1800 cm^{-1} range.

The Raman spectra of MoS_2/SWCNT (1:3, 1:1, 3:1, 5:1) composites along with the starting MoS_2 and SWCNT are presented in Figure 4a. Pristine MoS_2 nanoparticles show characteristic E^1_{2g} and A_{1g} signals at 380 and 407 cm^{-1} respectively, revealing nanoparticles to be in the 2H-phase [26]. While the pristine carbon nanotubes show typical D, G, and 2D signals at 1346,

1591, and 2667 cm^{-1} respectively along with the radial breathing mode (RBM) mode at 265 cm^{-1} [27]. With the rise in the proportion of MoS_2, the MoS_2/SWCNT hybrids display progressive improvement in the relative intensities of MoS_2 compared to those of SWCNT signals. Further, the G band of MoS_2/SWCNT (1:1, 3:1, 5:1) mixture is slightly red-shifted compared to that of pristine SWCNT possibly due to charge-transfer interactions between the physically mixed constituents (Figure 4b**).** The G band in the Raman spectra of MoS_2-rich composites, (MoS_2 to SWCNT ratios of 5:1, 3:1 and 1:1) are red-shifted by 10.0, 7.0 and 5.0 cm^{-1}, respectively with respect to the pristine SWCNT. The SWCNT-rich composite, 1:3, shows only a marginal red-shift of 1.0 cm^{-1}. It is noteworthy that the RBM mode of SWCNT is retained in the case of hybrid even after functionalization. In the MoS_2/BCN (1:3, 1:1, 3:1) nanocomposites, we observed Raman modes of 2H-MoS_2 at 382 and 408 cm^{-1} along with the D and G bands of BCN nanosheets (Figure 4c). The G band of MoS_2/BCN (1:1, 3:1) is somewhat red-shifted compared to the bare BCN nanosheets (Figure 4d). The Raman spectra recorded at various locations of MoS_2/SWCNT and MoS_2/BCN composites show peaks from both MoS_2 and SWCNT/BCN, further validating the uniform nature of the nanocomposites. Electrocatalytic HER activity of MoS_2/SWCNT and MoS_2/BCN composite is assessed in 0.5 M H_2SO_4 electrolyte by employing a three-electrode cell. Polarization curves of MoS_2/SWCNT (1:1) composite along with the starting MoS_2 and SWCNT are shown in Figure 5a. The onset potential (η) value which is the extent of additional energy required for a Faradic process of hydrogen evolution is lower in the case of MoS_2/SWCNT (1:1) mixture in comparison to the starting MoS_2 nanoparticle and SWCNT, suggesting higher catalytic activity for the composites. Pristine MoS_2 nanoparticles and SWCNT show onset potential values of -286 and -524 mV respectively which suggest MoS_2 is the more active component in hydrogen evolution. MoS_2/SWCNT (1:1) composite exhibits a 109 mV improvement in η (-177 mV)

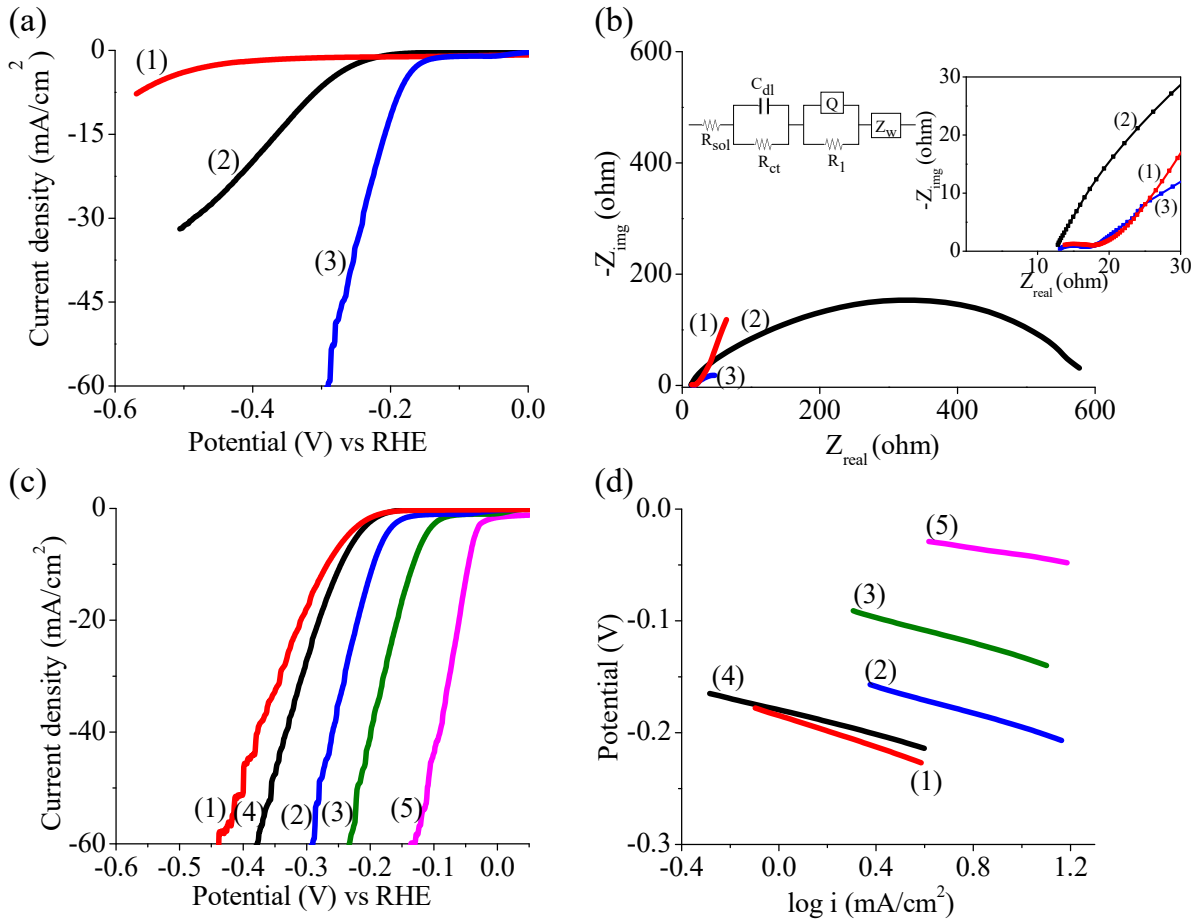

Figure 5. Electrocatalytic hydrogen evolution data: (a) LSV curves and (b) Nyquist plots of (1) SWCNT, (2) MoS_2 nanoparticles and (3) MoS_2/SWCNT (1:1) composites. Right inset of (b): Magnified portion of the Nyquist plot at the high-frequency region. Left inset of (b): equivalent circuit used to fit MoS_2/SWCNT (1:1) impedance result. The R_{sol}, R_{ct}, R_1, Q and Z_W are on behalf of the solution resistance, charge-transfer resistance; resistance accounted for the second semi-circle, constant phase element, and Warburg impedance. (c) LSV curves and (d) Tafel slopes of (1) MoS_2/SWCNT (1:3), (2) MoS_2/SWCNT (1:1), (3) MoS_2/SWCNT (3:1), (4) MoS_2/SWCNT (5:1) and (5) Pt/C catalyst.

compared to bare MoS_2 nanoparticles (-286 mV) and shows a steep enhancement in the current density with a rise in the overpotential. The improved activity in the case of the hybrids can be understood in terms of better charge transfer rate and more exposed edge sites. The

electrochemical impedance spectra (EIS) are measured to understand the conductivity advantages of the electrocatalyst. Figure 5 b shows the Nyquist plot obtained from the EIS data. To get the charge-transfer resistance (R_{ct}), we have fitted the EIS data to equivalent circuits shown in the inset of Figures 5b. The R_{ct} for the 1:1 MoS_2/SWCNT composite is 5.3 Ω which is much smaller than the pristine MoS_2 (579 Ω), suggesting the fast electron transport at the electrode/electrolyte interface of the composite. The R_{ct} for the SWCNT is 4.2 Ω, maybe due to its metallic nature. MoS_2 nanoparticle clusters are further dispersed into smaller assemblies during sonication and coupled with carbon networks (as evident in TEM images, Figure 3d, e) that generate more metallic edges for hydrogen adsorption and evolution.

To examine the optimal ratio of MoS_2 nanoparticles and SWCNT, we have compared the onset potentials of MoS_2/SWCNT (1:3), (1:1) (3:1) and (5:1) compositions where the data of commercial Pt/C catalyst is also incorporated (Figure 5c, Table 2). MoS_2/SWCNT (1:1, 3:1) ratios show lower onset potential than (1:3), with the 3:1 composition showing the lowest onset potential of -113 mV. The HER activity of the composite increases progressively with the MoS_2 proportion until MoS_2 and SWCNT ratio of 3:1. Beyond this ratio (5:1), the activity decreases and it is comparable with the carbon-rich (1:3) ratio. The above results specify coupling of MoS_2 nanoparticles with carboxyl-functionalized SWCNT significantly improve the electrocatalytic HER activity of the former, wherein the H_2 evolution rate rises swiftly with MoS_2 proportion because of the increased edge sites.

We have mixed MoS_2 nanoparticles with 2D BCN nanosheets to examine the effect of dimensionality of the conducting matrix on the activity of nanoparticles. The onset potential values obtained for MoS_2/BCN mixture of (1:3), (1:1) and (3:1) ratios are -231, -212 and -178 mV respectively (Figure 6a, Table 2). A similar trend in enhancement in activity with the rise

Table 2: Electrochemical HER activity of MoS_2/SWCNT and MoS_2/BCN composites compared with Pt/C.

Sample	Onset potential (mV vs RHE)	Tafel slope (mV dec^{-1})
SWCNT	524	310
MoS_2	286	113
BCN	449	130
MoS_2/SWCNT (1:3)	236	71
MoS_2/SWCNT (1:1)	177	61
MoS_2/SWCNT (3:1)	113	59
MoS_2/SWCNT (5:1)	220	54
MoS_2/BCN (1:3)	231	90
MoS_2/BCN (1:1)	212	83
MoS_2/BCN (3:1)	178	101
Pt/C	33	37

in MoS_2 proportion is observed with the MoS_2/SWCNT composites as well. However, the improvement in η value with MoS_2/BCN mixtures, in relation to pristine MoS_2 nanoparticles, is somewhat lower than that of MoS_2/SWCNT. The MoS_2 nanoparticle clusters can easily intercalate between the percolated nanotube networks as compared to the stacked BCN nanosheets (Figure 2c); therefore mixing MoS_2 nanoparticles with SWCNT ensures relatively more interfacial area, lower charge-transfer resistance and hence shows higher activity. The EIS curves of bare MoS_2, BCN and MoS_2/BCN (3:1) composite are shown in Figure 6c and estimated the R_{ct} values by fitting Nyquist plot to equivalent circuit (Inset of Figure 6c). The obtained R_{ct} values of MoS_2/BCN (3:1) composite (87 Ω) is much less than bare MoS_2 nanoparticle (579 Ω). Thus, such a lower value of MoS_2/BCN (3:1) composite indicates that

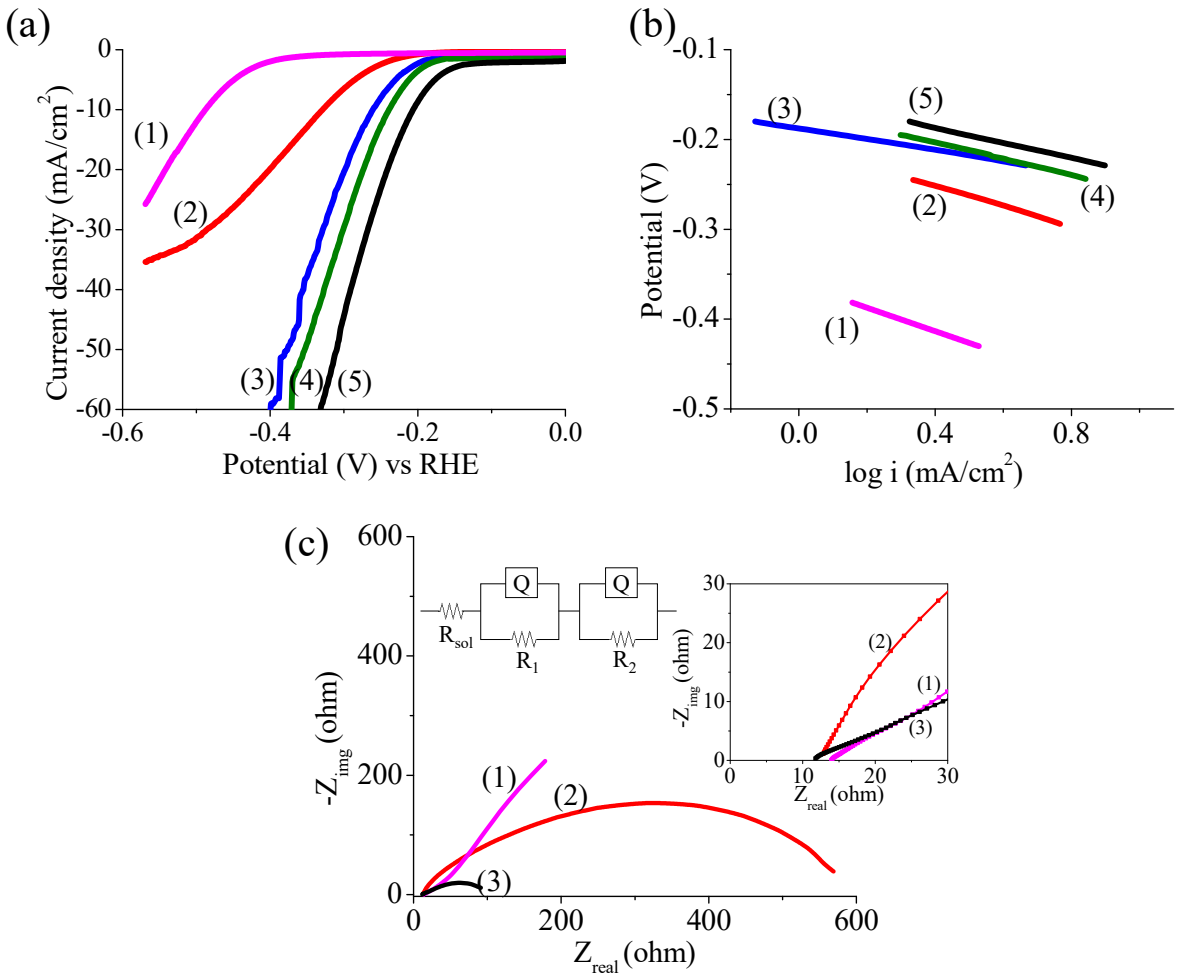

Figure 6. (a) LSV curves and (b) Tafel slopes of (1) BCN, (2) MoS_2 nanoparticles, (3) MoS_2/BCN (1:3), (4) MoS_2/BCN (1:1) and (5) MoS_2/BCN (3:1) nanocomposites. (c) Nyquist plots of (1) BCN, (2) MoS_2 nanoparticles and (3) MoS_2/BCN (3:1) composites. Right inset of (c): Magnified portion of the Nyquist plot at the high-frequency region. Left inset of (c): equivalent circuit used to fit MoS_2/SWCNT (1:1) impedance results.

its higher electrocatalytic activity for HER is attributed to the conducting BCN sheets that enhance charge-transfer characteristics of MoS_2 nanoparticles. Further, we also studied the HER activity of 1D-MoS_2 nanotubes mixed with 1D carbon nanotubes or 2D BCN sheets, which do not show any enhancement in activity compared to the individual components (Figure 7a, b). Unlike MoS_2 nanoparticles, it may not be feasible for 1D-MoS_2 nanotubes (Inset of

Figure 7a) to be intercalated between the percolated carbon networks or stacked BCN sheets which result in a non-uniform mixture, thus show lower activity. The above results indicate dimensionality of both the active component (MoS_2) and conducting matrix (SWCNT or BCN) is seminal in attaining synergy in overall HER activity.

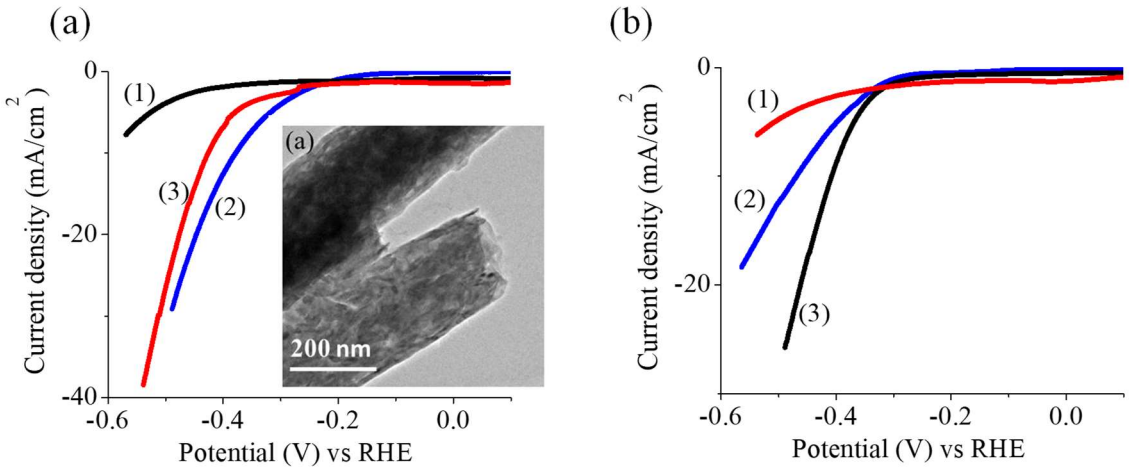

Figure 7. LSV curves of (a) MoS_2 nanotube (1), SWCNTs (2), MoS_2 nanotube/SWCNT mixture (Inset: FESEM image of pristine MoS_2 nanotubes procured from Holon Institute of Technology); (b) MoS_2 nanotube (1), BCN nanosheets (2), MoS_2 nanotube/BCN mixture (3).

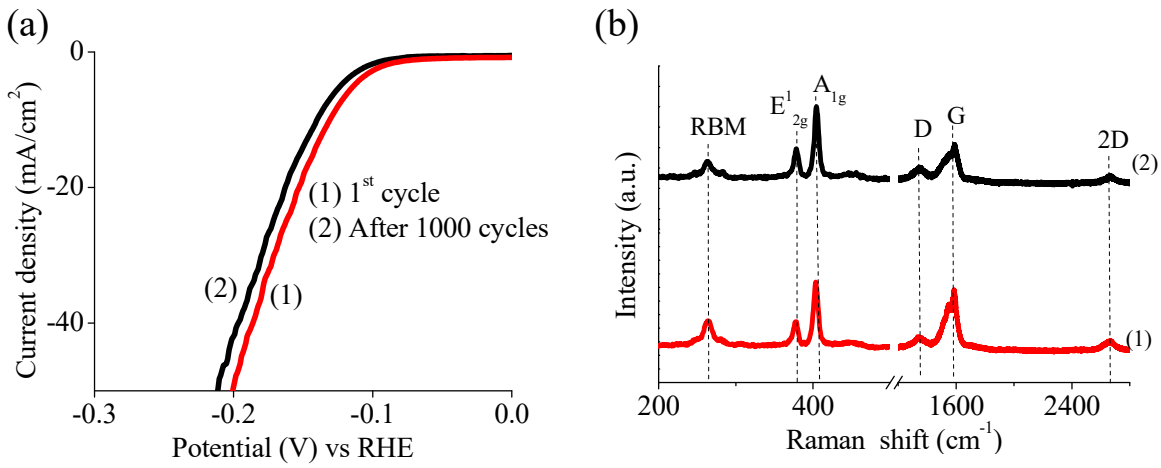

Figure 8. (a) Cyclic stability and (b) Raman spectra of MoS_2/SWCNT (3:1) composite before (1) and after (2) hydrogen evolution studies.

To gain further insights into the kinetics of hydrogen evolution on the MoS_2/SWCNT and MoS_2/BCN composites, Tafel plots were explored. Tafel slope can be obtained by plotting log (current density) versus overpotential in the cathodic potential (η) range and the slope corresponds to the rising curve shows the Tafel slope value. The Tafel slope values of the various catalysts is 71, 61, 59, 54 and 37 mV dec^{-1} for MoS_2/SWCNT (1:3), (1:1), (3:1), (5:1) and Pt/C respectively (Figure 5d, Table 2). The starting SWCNT and MoS_2 display high Tafel slopes of 310 and 113 mV dec^{-1} respectively (Table 2).

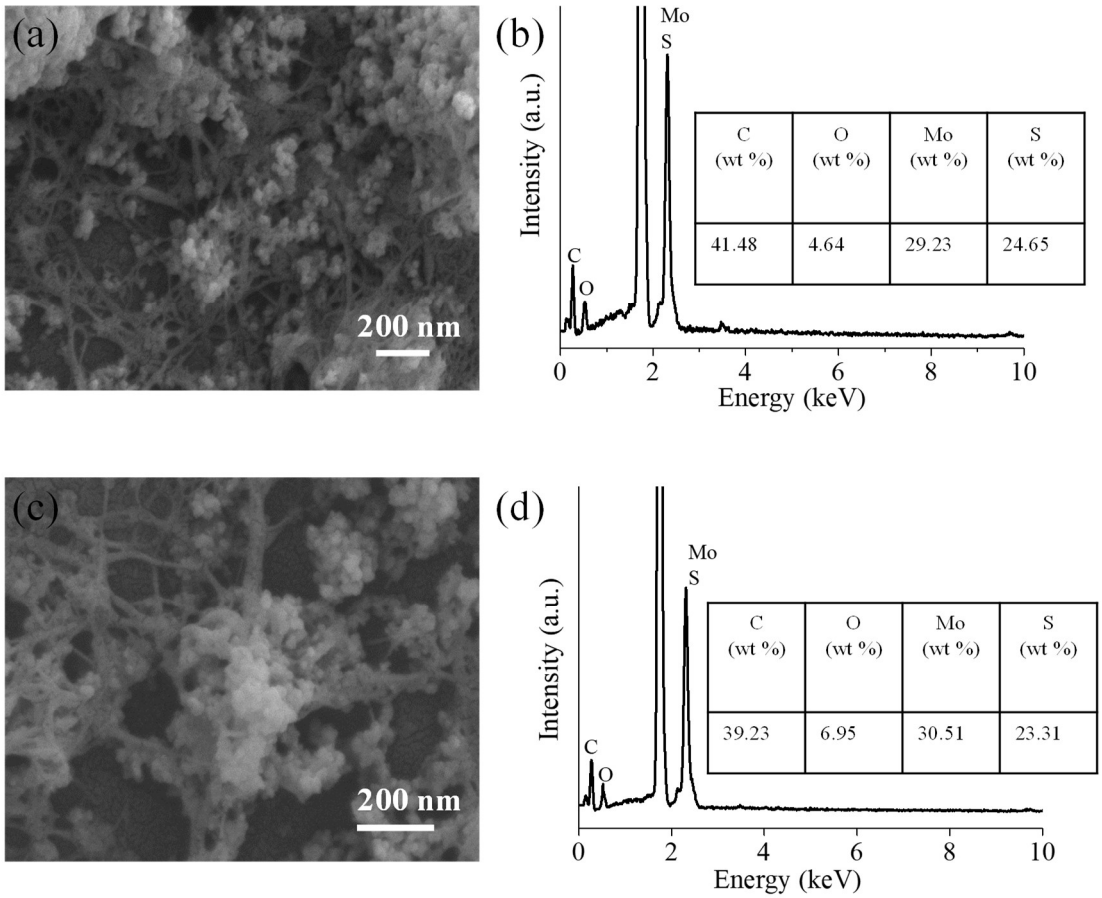

Figure 9. (a, b) FESEM and EDS of MoS_2/SWCNT (1:3) composite prior to HER experiment; (c, d) FESEM and EDS of MoS_2/SWCNT (1:3) composite after HER experiment.

The lower Tafel slope value for MoS_2/SWCNT composite signifies the efficacy of MoS_2 and SWCNT mixture in electron transport to the active sites. MoS_2/BCN (1:3), (1:1) and (3:1) ratios show 90, 83 and 101 mV dec^{-1} respectively while the pristine BCN shows a high value of 130 mV dec^{-1} (Figure 6b, Table 2). MoS_2/SWCNT (1:3) composite does not show any substantial change in the onset potential even after 1000 LSV cycles, suggesting the HER activity of the catalyst to be robust (Figure 8a). The Raman spectrum of MoS_2/SWCNT after the hydrogen evolution study shows that the relative intensity of SWCNT bands (D and G) is quenched compared to the MoS_2 signals (E_{2g}^1 and A_{1g}). The generation of defect sites due to electrochemical perturbations[28] and adsorption of hydronium ions at the sidewall of the nanotube possibly diminishes the intensity of SWCNT signals.[29,30] Further, energy dispersive X-ray spectroscopy (EDS) of MoS_2/SWCNT (3:1) before and after HER experiments reveal a minor change in C, Mo and S relative composition, suggesting that catalyst is chemically stable under electrochemical conditions (Figure 9). In Table 3, we have compared the onset potential, overpotential at 10 mA cm^{-2}, and Tafel slope values of MoS_2/SWCNT and MoS_2/BCN composites with other 1D/2D MoS_2-CNT/graphene nanocomposites reported. It is noteworthy that onset potential (-113 mV) and Tafel slope (59 mV dec^{-1}) of MoS_2/SWCNT (3:1) composite is lower than those reported for most of the MoS_2-based nanocomposite electrocatalysts.

Table 3: Comparison of the electrocatalytic hydrogen evolution activity of MoS_2/SWCNT and MoS_2/BCN hybrids with other MoS_2-CNT/graphene nanocomposites reported in the literature.

Catalyst	Onset potential (mV vs RHE)	Overpotential (@10 mA/cm^2)	Tafel slope (mV dec^{-1})
MoS_2 nanosheets [31]	300	-	-
MoS_2 nanoparticle [32]	270	-	59
2D MoS_2/N-Graphene [33]	236	261	230
MoS_2/MWCNT [34]	211	-	136
2D MoS_2/Graphene [35]	190	-	79
1D MoS_2/rGO [36]	180	250	69
2D MoS_2/MWCNT [37]	174	284	97
1D MoS_2@MWCNT [38]	150	-	109
2D MoS_2/RGO [39]	140	-	41
*MoS_2/CNT-Graphene [40]	140	255	100
*Co-MoS_2/Graphene [41]	142	194	44
2D MoS_2/Graphene [42]	130	218	57
*Cu-MoS_2/rGO [43]	126	-	90
2D MoS_2/N-rGO [44]	119	-	36
2D MoS_2/CNTs [45]	108	277	66
0D/3D MoS_2/Graphene [46]	-	150	56
*MoS_2/Graphene-NiO [47]	-	150	80
$MoTe_2$/Graphene [48]	-	150	94
#MoS_2/BCN (3:1)	178	205	101
#MoS_2/SWCNT (3:1)	113	132	59

MWCNT- Multi-walled carbon nanotube, CNT- Carbon nanotube, rGO-Reduced graphene oxide, *Ternary composites, #Composite reported in the present study.

5. Conclusions

We have successfully prepared MoS_2/SWCNT and MoS_2/BCN composites by mixing various proportions of colloidal dispersions containing MoS_2 and carboxyl-functionalized SWCNT/BCN. The Raman spectra provide evidence for electronic interaction between the MoS_2 nanoparticles and SWCNT/BCN in the composites. Electrocatalytic HER studies indicate that MoS_2/SWCNT (3:1) catalyst exhibits a superior electrocatalytic activity with a highly positive onset potential (-113 mV vs RHE) and a small Tafel slope of 59 mV dec^{-1}, which is comparable to some of the highest reported MoS_2-CNT/graphene composites. The high activity of composite is attributed to the efficient intercalation of MoS_2 nanoparticles between the highly conducting entangled SWCNT networks, improving charge-transfer interactions as well as the interfacial area between MoS_2 nanoparticles and carbon nanotubes.

6. References

[1] Q. H. Wang, K. Kalantar-Zadeh, A. Kis, J. N. Coleman, M. S. Strano, *Nat. Nanotechnol.* **2012**, *7*, 699.

[2] F. Wang, T. A. Shifa, X. Zhan, Y. Huang, K. Liu, Z. Cheng, C. Jiang, J. He, *Nanoscale* **2015**, *7*, 19764.

[3] X. Chia, A. Y. S. Eng, A. Ambrosi, S. M. Tan, M. Pumera, *Chem. Rev.* **2015**, *115*, 11941.

[4] X. Duan, C. Wang, A. Pan, R. Yu, X. Duan, *Chem. Soc. Rev.* **2015**, *44*, 8859.

[5] J. Kibsgaard, Z. Chen, B. N. Reinecke, T. F. Jaramillo, *Nat. Mater.* **2012**, *11*, 963.

[6] J. Xie, J. Zhang, S. Li, F. Grote, X. Zhang, H. Zhang, R. Wang, Y. Lei, B. Pan, Y. Xie, *J. Am. Chem. Soc.* **2013**, *135*, 17881.

[7] M. V. Bollinger, J. V. Lauritsen, K. W. Jacobsen, J. K. Nørskov, S. Helveg, F. Besenbacher, *Phys. Rev. Lett.* **2001**, *87*, 3.

[8] X. Lin, W. Li, Y. Dong, C. Wang, Q. Chen, H. Zhang, *Comput. Mater. Sci.* **2016**, *124*, 49.

[9] C. Ataca, H. Şahin, E. Aktuörk, S. Ciraci, *J. Phys. Chem. C* **2011**, *115*, 3934.

[10] C. N. R. Rao, K. Gopalakrishnan, U. Maitra, *ACS Appl. Mater. Interfaces* **2015**, *7*, 7809.

[11] B. Mohanty, A. Mitra, B. Jena, B. K. Jena, *Energy and Fuels* **2020**, *34*, 10268.

[12] N. K. Singh, A. Soni, R. Singh, U. Gupta, K. Pramoda, C. N. R. Rao, *J. Chem. Sci.* **2018**, *130*, 1.

[13] J. Tan, Y. Mei, H. Shen, H. Liu, T. Azhagan, W. Song, T. Thomas, J. Liu, M. Yang, M. Gao, *ChemCatChem* **2020**, *12*, 122.

[14] J. Yang, K. Wang, J. Zhu, C. Zhang, T. Liu, *ACS Appl. Mater. Interfaces* **2016**, *8*, 31702.

[15] J. Xie, H. Zhang, S. Li, R. Wang, X. Sun, M. Zhou, J. Zhou, X. W. Lou, Y. Xie, *Adv. Mater.* **2013**, *25*, 5807.

[16] X. Geng, W. Wu, N. Li, W. Sun, J. Armstrong, A. Al-Hilo, M. Brozak, J. Cui, T. P. Chen, *Adv. Funct. Mater.* **2014**, *24*, 6123.

[17] J. Cao, J. Zhou, Y. Zhang, X. Liu, *Sci. Rep.* **2017**, *7*, 1.

[18] P. S. Toth, M. A. Bissett, T. J. A. Slater, N. Savjani, A. K. Rabiu, A. M. Rakowski, J. R. Brent, S. J. Haigh, P. O. Brien, R. A. W. Dryfe, *Adv. Mater.* **2016**, *28*, 8256.

[19] Y. Liu, X. Xu, J. Zhang, H. Zhang, W. Tian, X. Li, M. O. Tade, H. Sun, S. Wang, *Appl. Catal. B Environ.* **2018**, *239*, 334.

[20] Y. Liu, X. He, D. Hanlon, A. Harvey, J. N. Coleman, Y. Li, *ACS Nano* **2016**, *10*, 10.

[21] E. Ahn, B. S. Kim, *ACS Appl. Mater. Interfaces* **2017**, *9*, 8688.

[22] M. Chhetri, S. Maitra, H. Chakraborty, U. V. Waghmare, C. N. R. Rao, *Energy Environ. Sci.* **2016**, *9*, 95.

[23] D. Duphil, S. Bastide, C. Lévy-Clément, *J. Mater. Chem.* **2002**, *12*, 2430.

[24] C. N. R. Rao, K. Pramoda, *Bull. Chem. Soc. Jpn.* **2019**, *92*, 441.

[25] K. A. Wepasnick, B. A. Smith, J. L. Bitter, D. Howard Fairbrother, *Anal. Bioanal. Chem.* **2010**, *396*, 1003.

[26] B. Li, L. Jiang, X. Li, P. Ran, P. Zuo, A. Wang, L. Qu, Y. Zhao, Z. Cheng, Y. Lu, *Sci. Rep.* **2017**, *7*, 1.

[27] P. M. V. Raja, G. L. Esquenazi, K. D. Wright, C. E. Gowenlock, B. E. Brinson, S. Alexander, D. R. Jones, V. S. Gangoli, A. R. Barron, *Nanoscale* **2018**, *10*, 19628.

[28] G. Ferrari, A. Brownson, C. E. Banks, Investigating the Integrity of Graphene towards the Electrochemical Hydrogen Evolution Reaction (HER). *Sci. Rep.* **2019**, 9, 15961.

[29] M. S. Strano, C. A. Dyke, M. L. Usrey, P. W. Barone, M. J. Allen, H. Shan, C. Kittrell, R. H. Hauge, J. M. Tour, R. E. Smalley, Science **2003**, 301 1519.

[30] S. Lin, A. J. Hilmer, J. D. Mendenhall, M. S. Strano, D. Blankschtein, *J. Am. Chem. Soc.* **2012**, 134, 8194.

[31] D. C. Binwal, M. Kaur, K. Pramoda, C. N. R. Rao, *Bull. Mater. Sci.* **2020**, *43*, 313.

[32] D. Wang, X. Zhang, Y. Shen, Z. Wu, *RSC Adv.* **2016**, *6*, 16656.

[33] Y. Hou, B. Zhang, Z. Wen, S. Cui, X. Guo, Z. He, J. Chen, *J. Mater. Chem. A* **2014**, *2*, 13795.

[34] M. Dinesh, K. Muthumalai, Y. Haldorai, R. T. R. Kumar, *Electroanalysis* **2020**, 32, 2571.

[35] J. Guo, F. Li, Y. Sun, X. Zhang, L. Tang, *J. Power Sources* **2015**, *291*, 195.

[36] L. Song, M. Zhao, X. Li, Z. Zhang, L. Qu, *RSC Adv.* **2016**, *6*, 70740.

[37] Y. Li, X. Yin, X. Huang, X. Liu, W. Wu, *Int. J. Hydrogen Energy* **2020**, *45*, 16489.

[38] A. B. Laursen, S. Kegnæs, S. Dahl, I. Chorkendorff, *Energy Environ. Sci.* **2012**, *5*, 5577.

[39] X. Zheng, J. Xu, K. Yan, H. Wang, Z. Wang, S. Yang, *Chem. Mater.* **2014**, *26*, 2344.

[40] D. H. Youn, S. Han, J. Y. Kim, J. Y. Kim, H. Park, S. H. Choi, J. S. Lee, *ACS Nano* **2014**, *8*, 5164.

[41] J. Ye, W. Chen, S. Xu, Z. Yu, S. Hou, *RSC Adv.* **2016**, *6*, 104925.

[42] X. Yin, Y. Yan, M. Miao, K. Zhan, P. Li, J. Yang, B. Zhao, B. Y. Xia, *Chem-Eur. J.* **2018**, *24*, 556.

[43] F. Li, L. Zhang, J. Li, X. Lin, X. Li, Y. Fang, J. Huang, W. Li, M. Tian, J. Jin, R. Li, *J. Power Sources* **2015**, *292*, 15.

[44] L. Zhao, C. Hong, L. Lin, H. Wu, Y. Su, X. Zhang, A. Liu, *Carbon N. Y.* **2017**, *116*, 223.

[45] K. Zhu, Q. Li, H. Ren, Y. Sun, C. Li, R. Lv, S. Fan, J. Yang, Y. Guo, K. Liu, *ACS Appl. Nano Mater.* **2021**, *4*, 4754.

[46] Y. Liu , Y. Zhu, X. Fan, S. Wang,, Y. Li , F. Zhang, G. Zhang , W. Peng, *Carbon* **2017**, *121*, 163.

[47] J. Yan, Y. Huang L. Zhang, M. Zhou, P. Yang W. Chen, X. Deng, H. Yang, *J. Sol-Gel Sci. Techn.* **2020**, *93*, 462.

[48] S. Sarwar, A. Ali, Z. Liu, J. Li, S. Uprety, H. Lee, R. Wang, M. Park, M. J. Bozack, A. J. Adamczyk, X. Zhang, *J. Colloid Interface Sci.* **2021**, *581*, 847.

****